

ESS Instrument Construction Proposal

Estia – focusing reflectometer

	Name	Affiliation
Proposer	Dr. Jochen Stahn jochen.stahn@psi.ch	Paul Scherrer Institut Laboratory for Neutron Scattering WHGA / 142 5232 Villigen PSI Switzerland
Co-proposers	Marité Cárdenas cardenas@nano.ku.dk	Nano-Science Center University of Copenhagen Universitetsparken 5 2100 København Ø Denmark
ESS coordinator	Dr. Hanna Wacklin Hanna.wacklin@esss.se	European Spallation Source ESS AB 221 00 Lund Sweden

Note: All proposals received by ESS will be included as Expressions of Interest for In-kind contributions. ESS will use this information for planning purposes and the proposer or affiliated organization is not obligated to materially contribute to the project.

	Name
Document submitted to	Ken Andersen
Distribution	Dimitri Argyriou, Oliver Kirstein, Arno Hiess, Robert Connatser, Sindra Petersson Årsköld, Richard Hall-Wilton, Phillip Bentley, Iain Sutton, Thomas Gahl, relevant STAP

Document Number
Project Name Estia – focusing reflectometer
Date 30/10/2013

ENCLOSURES

The proposal including summary and table of contents is attached as **estia.pdf** (front matter and chapters 1 to 5). This file also contains extensive attachments with details on the *Selene*-type guide geometry, operation modes, and experience with the prototype tested at PSI (chapters 6 to 11).

The file can also be downloaded at <http://people.web.psi.ch/stahn/estia.pdf>.

PROPOSAL HISTORY

New proposal:	yes
Resubmission:	no

**Instrument Proposal of the
Swiss-Danish Instrument Initiative
for the European Spallation Source, ESS**

Estia
Εστία

a

focusing reflectometer for small samples

based on the

Selene guide concept

Swiss-Danish instrument initiative

October 30, 2013




Paul Scherrer Institut



Selene
focusing neutron guide



project team

Jochen Stahn	Laboratory for Neutron Scattering Paul Scherrer Institut Switzerland jochen.stahn@psi.ch +41 56 310 2518	senior scientist - project leader - concept - experiments - McStas
Panagiotis Korelis	Laboratory for Neutron Scattering Paul Scherrer Institut Switzerland panagiotis.korelis@psi.ch +41 56 310 5813	post-doc - McStas - experiments
Uwe Filges	Laboratory for Developments and Methods Paul Scherrer Institut Switzerland uwe.filges@psi.ch +41 56 310 4606	senior scientist - McStas, MCNPX
Tobias Panzner	Laboratory for Developments and Methods Paul Scherrer Institut Switzerland tobias.panzner@psi.ch +41 56 310 4342	pst-doc - McStas - experiements
Emmanouela Rantsiou	Laboratory for Developments and Methods Paul Scherrer Institut Switzerland emmanouela.rantsiou@psi.ch +41 56 310 4631	pst-doc - McStas, MCNPX
Marité Cardenas	Nano-Science Center University of Copenhagen Denmark cardenas@nano.ku.dk +45 35 320 431	senior scientist - scientific advice
Ursula Bengaard Hansen	Nano-Science Center University of Copenhagen Denmark uhansen@fys.ku.dk +45 60 478 615 (mobile)	student assistant - McStas - experiements
Beate Klösgen	Department for Physics, Chemistry and Pharmacy University of Southern Denmark Denmark kloesgen@sdu.dk +45 6550 2561	associate professor - scientific advice
<i>Selene</i>		moon, dark side titan goddess
	detail of the ceiling painting <i>Selene and Endymion</i> at the <i>Ny Carlsberg Glyptotek, Copenhagen</i>	

Estia**Εστία
a focusing reflectometer for small samples**

The *Swiss-Danish Instrument Initiative* presents Εστία¹, a concept for a focusing reflectometer optimised for small samples.

Scientific areas of interest for reflectometry include the investigation of novel phenomena resulting from the forced coexistence of conflicting properties on an atomic scale, and the understanding of biological mechanisms at cell membranes. On the technical side there is the improvement of magnetic data storage and processing, and of protective or functional coatings. The resulting variety in sample sizes, geometry, measurement-range and resolution leads to competing optimisation criteria for a reflectometer.

The scientific focus of Εστία is the investigation of structural and magnetic depth profiles of solid film structures. Probing liquid/solid interfaces or lateral structures is also possible. To accommodate the large demand for reflectometry and the diversity of research fields, we suggest to build additional and complementary reflectometers, optimised for liquid surfaces and organic samples in general, and eventually one instrument dedicated to the investigation of lateral structures.

A selection of very active areas of research that will profit greatly from Εστία is:

- The investigation of magnetic heterostructures. These are the basic building blocks for a large number of magneto-electric devices, and increasingly for sensors and switches.
- Multifunctional materials, combining and linking magnetic, electronic and mechanical properties. While the coupling observed so far in bulk is rather weak, the combination of materials coupled via an interface opens a wide and promising field of research and applications.
- Insulating metal-oxide heterostructures that develop mobile electron gases at the interfaces, and which show a rich spectrum of physical properties. These novel electronic phases are of increasing scientific and technological interest.
- (Self-) diffusion of atoms in solids is a fundamental matter transport process. It plays a key role for the design and optimisation of materials as well as for the performance of devices in various branches of technology like energy storage/conversion, electronic devices, sensor technology and nanostructured materials design.

The unique feature of Εστία is its truly focusing neutron guide, based on the *Selene* concept. Its point-to-point focusing enables the shaping of the phase space density necessary for the measurements, and it guarantees a high transmission. At the same time, it drastically reduces the total beam intensity in the guide, which results in a low background and much reduced radiation. Furthermore, the beam is convergent at the sample which avoids over-illumination. The special guide geometry allows for efficient optics to polarise and filter the beam, or to implement constant resolution without using pulse shaping choppers. The convergent beam can be used efficiently on sample surfaces reaching from $1 \times 1 \text{ mm}^2$ to $50 \times 10 \text{ mm}^2$. To allow for high detector angles and to reduce the influence of gravity, the preferred scattering plane is horizontal. A wavelength-range $\lambda = 5 \text{ \AA}$ to 9.4 \AA is obtained both by reducing the counting time, and by avoiding the proton pulse duration for data acquisition.

Εστία provides several operation modes, where switching from one to the other implies only the insertion of some optics or the activation of a slit. In a low-resolution mode it will be possible to investigate dynamic processes on a split-second time-scale, or to track the influence of external conditions on magnetic properties. Another mode provides the performance of a conventional TOF reflectometer, allowing for the separation of specular and off-specular scattering. Additionally the use of the high divergence of the beam for energy-angle-encoding results in a constant resolution for specular reflectivity, a wide q_z -range, and an improved q -space volume for off-specular measurements.

Further options include the generation of a clean parallel beam, e.g. for GISANS experiments, or the addition of spin echo techniques. The instrument will have a full polarisation and polarisation analysis option. It will be able to host heavy and bulky sample environment, and accept high magnetic fields.

The combination of the high-brilliance ESS source and the novel *Selene* guide concept, transferring as much of this brilliance as possible to the sample in a fully controlled way, will result in a high-performance reflectometer with outstanding efficiency for small samples. Εστία uses the full unchopped long pulse provided by the ESS. The gain in comparison to a similar instrument at a continuous source with the same average power is thus a factor 30.

¹Estia is the Greek goddess of the hearth, the family, and architecture. In modern Greek the word means *point of interest or importance* and is used for example when adjusting a telescope or a camera lens.

Contents

Instrument Proposal	1
1 Scientific Case	1
1.1 selected scientific opportunities	1
1.1.1 magnetic heterostructures	1
1.1.2 multifunctional materials	2
1.1.3 novel electronic phases at interfaces	2
1.1.4 in-situ monitoring of film growth	3
1.1.5 diffusion processes in solids	3
1.1.6 laterally structured surfaces	3
1.2 performance criteria	4
1.2.1 sample size	4
1.2.2 measurement time	4
1.2.3 resolution	4
1.2.4 off-specular scattering	5
1.2.5 polarisation	5
1.2.6 extensions	5
1.2.7 sample environment	5
1.3 instrument performance	5
1.4 overlap with the soft-matter reflectometer	6
1.5 user community, existing facilities	6
1.6 infrastructure & support facilities	7
2 Description of Instrument Concept and Performance	9
2.1 instrument lay-out	9
2.2 <i>Selene</i> guide	11
2.3 beam extraction	12
2.4 shielding	13
2.4.1 MCNPX simulations	13
2.4.2 shutter	13
2.5 energy- and time-range	14
2.5.1 flux and λ_{\min}	14
2.5.2 time regime and λ_{\max}	15

2.5.3	intrinsic λ resolution	16
2.5.4	frame-overlap suppression	16
2.5.5	choppers	16
2.6	polarisation	16
2.6.1	permanent polarisation	16
2.6.2	optional polarisation	16
2.6.3	analyser	16
2.6.4	flipper	17
2.7	sample stage	17
2.8	beam shaping	17
2.8.1	beam definition	17
2.8.2	apertures within guides	17
2.8.3	fast aperture	17
2.9	detector	18
2.9.1	area detector	18
2.9.2	single detector	18
2.9.3	CCD camera	18
2.10	operation modes	18
2.10.1	almost conventional & off-specular reflectivity	19
2.10.2	angle-energy-encoding	19
2.10.3	high-intensity specular reflectometry	20
2.10.4	further options	21
2.11	simulations	22
2.12	performance	23
2.13	design options	24
3	Technical Maturity	25
3.1	guide system	25
3.2	optical components, polarisation	26
3.3	mechanics, sample stage	26
3.4	fast slit system	26
3.5	detector	27
3.6	computing, data analysis	27
4	Costing	29
4.1	insert in the extraction unit and instrument shielding	29
4.2	guide	29
4.3	guide support	29
4.4	mechanics (sample stage and the like)	30
4.5	motion control	30
4.6	detector	30
4.7	filter / polariser	30

Appendices	31
5 List of abbreviations	31
6 the Selene guide system	33
6.1 geometrical considerations for an elliptic reflector	34
6.2 angular acceptance	37
6.3 coma aberration — and correction	37
6.4 chromatic aberration due to gravity	40
6.5 transmission	42
6.6 divergence vs. peak-to-background ratio	43
7 Optics and Beam Shaping	45
7.1 frame-overlap and polarisation filter	45
7.2 condenser	47
7.3 zoom	48
8 Boundary Conditions and Consequences	49
8.1 space	49
8.2 shielding and background	50
8.3 exclusion of proton prompt	50
8.3.1 intrinsic resolution	50
9 Technical Details	53
9.1 moving elements	53
9.2 detector characteristics	54
9.2.1 cross-talk	55
10 Measurement Schemes and Data Reduction	57
10.1 conventional mode, solid-liquid cell	58
10.1.1 the sample	58
10.1.2 the measurement scheme	58
10.1.3 sample alignment	58
10.1.4 data acquisition	59
10.1.5 reference measurement	59
10.1.6 normalisation and integration	59
10.1.7 discussion	59
10.2 λ - θ -encoding, off-specular measurements	60
10.2.1 the sample	60
10.2.2 the measurement scheme	60
10.2.3 sample alignment	62
10.2.4 data acquisition	62
10.2.5 reference measurement	62
10.2.6 normalisation and integration	63
10.2.7 discussion	63

10.3	high-intensity specular mode, small magnetic sample	64
10.3.1	the sample	64
10.3.2	the measurement scheme	64
10.3.3	sample alignment	64
10.3.4	data acquisition	64
10.3.5	reference measurement	65
10.3.6	normalisation and integration	66
10.3.7	discussion	67
10.4	aspects on the data reduction	68
10.4.1	raw-data and intensity-maps	68
10.4.2	normalisation	68
10.4.3	resolution	68
11	Prototype	71
11.1	design considerations	71
11.2	devices	71
11.2.1	pulse chopper	71
11.2.2	frame-overlap chopper	71
11.2.3	precision slit	72
11.2.4	double multilayer monochromator	72
11.2.5	sample holder	72
11.2.6	guide support	72
11.2.7	guide system	73
11.3	experiments on BOA	75
11.3.1	BOA	75
11.3.2	set-up	75
11.3.3	experiments in TOF mode	76
11.3.4	experiments with angle-wavelength-encoding	77
11.3.5	use of a diffusor	78
11.3.6	discussion	79
11.4	experiments on Amor	80
11.4.1	Amor	80
11.4.2	high-intensity specular reflectometry	80
11.4.3	angle-wavelength-encoding	83
11.4.4	discussion	83
	References	85

1 Scientific Case

Physical, chemical and biological states or processes at interfaces and surfaces are getting more and more into the focus of both fundamental and applied research. This field extends from improving surface conditioning or understanding biological mechanisms at cell membranes, to the improvement of magnetic data storage and processing, and the investigation of novel phenomena when conflicting properties are forced to coexist on an atomic scale.

One of the best suited methods to investigate interfaces is reflectometry. Neutron reflectometry in particular provides a high penetration depth, and sensitivity also for light elements. And it probes magnetism. Accordingly, the neutron reflectometry user community and therefore also the requirements for the instruments are quite broad. Good coverage can be obtained with three instruments: one for *soft matter* with rather large surface area, vertical scattering geometry, and medium to low resolution; one for *hard condensed matter* and *magnetic* studies, with reduced sample size, variable resolution requirements, and high momentum transfer; and finally one for *laterally structured surfaces*, demanding rather high resolution also in-plane. Building three specialised reflectometers at the ESS is justified by the size of the potential user community and the increasing interest in interfaces. This interest manifests in the large and still growing fraction of reflectometers in the instrument suits of existing facilities. This proposal deals with the solid-state reflectometer.

The combination of the highly brilliant neutron beam at the ESS with novel neutron optics and a novel guide design will improve the performance of reflectometry with polarised neutrons for small samples composed of thin layers by up to two orders of magnitude compared to existing instruments. The reason for this gain is that the design enables changing the resolution conditions in a very wide range, and that it opens the possibility for new measurement schemes. In the following we present a list of the feedback we received from today's leading scientists¹, when asked about key applications for a reflectometer at the ESS, the design criteria, and the performance expected.

1.1 selected scientific opportunities

1.1.1 magnetic heterostructures

Heterostructures involving magnetic materials are the basic building blocks of a large number of magneto-electronic devices such as read heads or magnetic random access memories. In addition, such heterostructures are increasingly being used as magnetic sensors in industrial applications and in the automotive industry. The performance of magnetic devices relies on the magnetic and elastic properties of the individual layers and on the coupling between the layers. These effects are a function of the morphology and microstructure of the grown layers and accordingly change during the growth of the heterostructures. To determine the structure within the layers and the perfection of the layers, reflectometry with polarised neutrons is a very powerful tool as it allows performing vector-magnetometry in heterostructures, layer by layer. The current trend is to decrease the size of the devices and to go towards thinner layers. Therefore, it is very important to adapt the experimental techniques to cope with the small cross-sections of these materials.

¹Input for this chapter was kindly provided by

a Christof Schneider, Paul Scherrer Institut, Switzerland

b Jean-Marc Triscone, Université de Genève, Switzerland

c Peter Böni, Technical University Munich, Germany

d Harald Schmidt, Clausthal University of Technology, Germany

e Christian Bernhard, Université de Fribourg, Switzerland

1.1.2 multifunctional materials

The last few years have witnessed a tremendous activity in the search for multifunctional materials combining magnetic, charge and orbital degrees of freedom, which may be controllably tuned. These systems combine several *ferroic* properties, i.e. symmetry breaking order parameters such as polarisation, magnetisation, and strain, which are subject to control parameters such as electric and magnetic field, and stress, respectively. The most direct way to engineer the desired functionality at room temperature is the combination of ferroic materials in a heterostructure. For the investigation of the interactions between the magnetic and non-magnetic layers, neutron reflectivity is the only means to directly determine the formation of magnetic order and domains.

strain-induced ferromagnetism at the film/substrate interface in orthorhombic LuMnO_3 thin films

Materials featuring the co-existence of coupled magnetic and ferroelectric order allow the switching of magnetic moments by an electric field and vice versa.[1, 2] Experimentally, only a few multiferroic materials are known to be ferromagnetic (FM), with the large majority being antiferromagnetically ordered. This class of materials can potentially be used for future magnetic storage devices with an electronic read-out. To non-destructively identify and probe the spatial extend (thickness dependence) of ferromagnetism in a thin film, polarised neutron reflectometry (PNR) reaching large q_z is the best suited technique.[3, 4] Single crystalline-like thin films of orthorhombic LuMnO_3 , a material which is known to exhibit magnetically-induced ferroelectricity with an E type antiferromagnetic (AFM) ground state, were found to have FM localised close to the substrate-film interface.[5] Surprising is the fact, that an intrinsic robust AFM can be converted into a FM with $T_C > T_N$. The most likely origin is growth-induced strain at the substrate/film interface and a change in crystalline symmetry.

Future PNR experiments will address the exchange biased coupling of the FM and AFM when applying electric fields. The samples have to have electrodes structured onto the surface, which limits the space available to conduct the reflectivity measurements.^a

1.1.3 novel electronic phases at interfaces

Insulating metal-oxide heterostructures may develop mobile electron gases at the interfaces, which show a rich spectrum of physical properties which are of increasing scientific and technological interest. A prominent example is the interface $\text{LaSrO}_3/\text{SrTiO}_3$. It has been established that depending on the number of layers, the interfaces show an integer Quantum Hall Effect, magnetism, or even superconductivity. Gate fields can be used to alter the carrier density to an extent that the electrons are driven to become superconducting. For the investigation of the magnetic and superconducting properties, neutron reflectometry is the method of choice as it is sensitive to buried interfaces.

Induced magnetism at oxide interfaces The recent discoveries of a number of fascinating unexpected phenomena at interfaces between different perovskite oxides have been received with tremendous enthusiasm, leading to the emergence of the field of oxide interface engineering.

The conduction properties found at some interfaces between insulating oxides have attracted a lot of attention. Such conducting interfaces, first discovered in 2002 between a Mott insulator (LaTiO_3) and a band insulator (SrTiO_3) [6] and in 2004 between two band insulators (LaAlO_3 and SrTiO_3) [7], have been shown to host two-dimensional electron gases. These discoveries generated an impressive amount of work trying to understand the origin of the conductivity and studying the properties of these fascinating systems, among them superconductivity and magnetism [8, 9].

Several oxide interface systems display induced magnetic structures. Among those, the observation of exchange bias in superlattices composed of nominally paramagnetic metallic LaNiO_3 , and ultrathin semiconducting ferromagnetic LaMnO_3 layers is particularly exciting [10]. A shift of the magnetisation loop is observed when samples are field-cooled to below 20 – 25 K. Curiously, the effect appears mainly for superlattices grown along the less conventional [111] pseudocubic direction, which maximises the interactions between the Mn and Ni atoms at the interface.

The presence of exchange bias reveals the existence of a strong interfacial coupling, likely to be related to a charge transfer $\text{Mn}^{3+} + \text{Ni}^{3+} \rightarrow \text{Mn}^{4+} + \text{Ni}^{2+}$. It also implies the emergence of magnetism in the nominally paramagnetic LaNiO_3 layers. Although a number of different magnetic structures have been proposed to explain this intriguing observation [10], the exact magnetic properties of the interface are unclear. The ultrathin LaNiO_3 layers could be undergoing a transition to an antiferromagnetic state with the usual up-down spin arrangement, or the more complex spin arrangement common to the other members of the rare earth nickelates family [11] even evolving to a spin-density wave.[10]

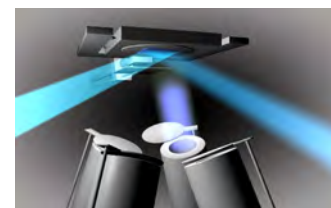
Moreover, TEM measurements have shown that the LNO/LMO interface is not quite the same as the LMO/LNO one. In the first case, a one monolayer interdiffusion is observed versus a two monolayer roughness for the second system. Preliminary magnetic and electrical transport measurements on these bilayers have also provided evidence for a significantly different magnetic behaviour. As a result, it is likely that the interface charge transfer and subsequent magnetic coupling could be different.

For several systems including the LNO/LMO superlattices described in some detail above, neutron reflectivity would be an ideal probe of the magnetic properties induced through the interface. Indeed, a precise chemical and magnetic profile measurement with monolayer sensitivity would represent an important step towards the understanding of charge transfer induced magnetism through these interfaces.^b

1.1.4 in-situ monitoring of film growth

The in-situ characterisation of thin films during growth by means of electron diffraction, for example RHEED, and even scanning probe microscopy or photo-spectroscopy is common practise. However, only few efforts have been made to characterise the evolution of the magnetic properties during the deposition of the layers. Neutron reflectometry is the method of choice as it measures directly the magnitude and the orientation of the magnetic moments throughout the heterostructure on a microscopic scale, in contrast to XMCD where only the surface is measured and vector information is lost.

An optimised beam line at ESS would allow conducting in-situ reflectometry with polarised neutrons in real time.^c



1.1.5 diffusion processes in solids

Self-diffusion of atoms in solids is a fundamental point-defect mediated matter transport process. It plays a key role for the design and optimisation of materials as well as for the performance of devices in various branches of technology like energy storage/conversion, electronic devices, and sensor technology. The investigation of diffusion processes on very short lengths scales ranging from atomic distances up to some tens of nanometers is an emerging field of research. It is especially important for the characterisation and design of nanostructured materials, metastable compounds and thin films as well as for the study of diffusion process close to room temperature and ultra-slow diffusion processes.

A method which can be used to realise such measurements is neutron reflectometry in combination with isotope multilayers [12]. Using this method, the destruction of an artificial lattice of stable isotopes by thermally induced interdiffusion is detected. Up to now, the method was used ex-situ to study self- and impurity diffusion in complex amorphous materials and metastable chemical compounds [12, 13, 14], in nano-crystalline metals [15], in single crystalline semiconductors [16], in ion conductors [17] and in electrode materials for Li-ion batteries [18].

In the framework of a seminal advancement of the method, in-situ experiments at elevated temperatures should be carried out in order to monitor real-time atomic migration processes in equilibrium and non-equilibrium states. This requires superior time resolution (seconds) for specular reflectivity, the use of small samples ($< 25 \text{ mm}^2$) due to handling with expensive isotopes, and for ensuring fast and homogeneous heating and cooling. Furthermore, a q_z -range up to 0.4 \AA^{-1} for the detection of diffusion close to atomic distances is required.^d

In-situ furnace for the *Selene* prototype on Amor@PSI



1.1.6 laterally structured surfaces

For laterally structured samples it is essential to measure the off-specular reflected signal. It is important to stress that the proposed instrument can be operated almost like a conventional TOF reflectometer. *Almost* means that the beam is nevertheless convergent. The only restriction is the maximum sample width, all other features are not compromised. This means that the brilliance available for off-specular measurements is about the same as for a conventional instrument.

finite size effects in complex oxides A number of interesting finite size effects on the magnetic and superconducting properties could be studied in nanostructured samples of complex oxides, like manganites, ruthenates or cuprates. In a collaboration between the University of Fribourg and the laboratory for nanotechnology at PSI, x-ray lithography and lithography with an e-beam writer have been used already to produce large area samples (up to 4 mm²) with micro- and nanostructures (squares and lines with different sizes and spacings).^e

1.2 performance criteria

1.2.1 sample size

A reduction of the size of the neutron beam spot in PNR experiments to an area as small as 1 mm² is a very desirable improvement. It is of significant advantage for a number of samples that are of scientific interest in the field of magnetic and superconducting thin film materials. Specific examples are:^e

limited homogeneous area PLD grown thin film samples are generally limited in their lateral size. Most materials can be comfortably grown for sizes up to 5 × 5 mm². These limits naturally arise due to the finite size of the laser plume and from the requirement of having a very homogeneous temperature over the entire substrate area. Larger area thin films and multilayers can be grown (for example by toggling) but at the cost of unwanted variations in thickness and structural and chemical homogeneity.

scanning graded samples Wedge-multilayers with a ramp-type change of the layer thickness in one direction. These could be used to measure very efficiently the influence of the layer thickness on the magnetic properties, by scanning the neutron beam along the ramp direction.

masking of contacts There are various types of devices based on oxide multilayers in which interesting magnetic effects can be induced by applying a voltage, for example in spintronic or multiferroic devices. In most cases this requires electrodes which need to be contacted on the side of the sample. A small footprint would allow us to keep these contacts away from the area that is probed in the PNR experiments.

The figure shows a contacted sample as used for MuSR measurements.[19]

limited sample size Bulk materials with interesting surface magnetic properties that can only be grown as relatively small single crystals. Examples are topological insulators in which characteristic magnetic states can be induced by electric currents. There are also ruthenates like SrRuO₃ for which a high temperature ferromagnetic surface state has been predicted.

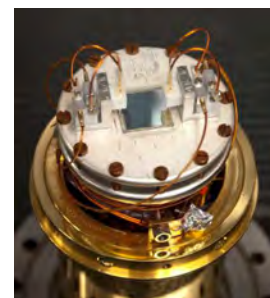
compatibility with other techniques Techniques complementary to neutron reflectivity such as XRD, XMCD or resonant x-ray reflectometry performed at synchrotron sources, or probes like SQUID or transport measurements often impose a restriction on sample size of 5 × 5 mm² to 1 cm². It is a big advantage if the very same sample can be investigated also by neutron reflectometry.

1.2.2 measurement time

Short measurement times are needed for the in-situ investigations mentioned above. E.g. for the growth studies long counting times result in the oxidation of the sample. To monitor real time atomic migration processes a time resolution on the split-second time scale is necessary. And also when scanning parameter-ranges (e.g. external electric or magnetic field, temperature) a fast (maybe even *quick and dirty*) way to map out the phase diagram would be favourable to identify the most interesting conditions for a high-quality measurement.

1.2.3 resolution

Heterostructures made from topological materials involving chiral structures such as the B20 compound MnSi or thin films (even monolayers) showing chiral magnetic order driven by the inversion symmetry at interfaces may become important functional materials for information technology or spintronics because the involved chiral entities are intrinsically very stable because they are protected by topology. In these materials several length scales compete with each other, for example exchange length, modulation length, film thickness, etc. A wide adaptability of the resolution (1% to > 10%) will allow to investigate the structural and magnetic properties over a very wide range of length scales while maintaining a high intensity.^a



1.2.4 off-specular scattering

In-plane off-specular scattering gives information about the lateral inhomogeneity of the sample in the μm -range. This allows for measuring the size of domains, or the periodicity and density profile of artificially structured or patterned surfaces.

1.2.5 polarisation

The investigation of magnetic depth profiles and of magnetic reversal processes is one of the main applications for the solid-state reflectometer. Spin polarisation and spin analysis are essential options of any respective neutron reflectometer already today, and even most of the soft matter reflectometers have at least a polarisation option.

1.2.6 extensions

GISANS There is a growing demand to investigate laterally structured samples. The beam needed for this Grazing Incidence Small Angle Neutron Scattering (GISANS) has to be highly brilliant, which restricts this method to the high-flux neutron sources. And often these measurements are performed on SANS instruments rather than on reflectometers. As a result, the specular reflectivity needed for data analysis has to be obtained on another instrument. It thus is desirable that a new reflectometer at a source with high brilliance allows for the implementation of a GISANS option.

spin-echo methods To implement a spin echo option, several meters of free space before and eventually behind the sample are needed.

1.2.7 sample environment

There is a wide variety of equipment around the sample. In the scientific examples mentioned above this included cryomagnets, in-situ furnaces, PLD- or sputtering-chambers. Further on, one will need solid-liquid cells with thermalisation, cools for spin echo methods. This means that there has to be a lot of space around the sample position available, and a flexible but reliable way of mounting all these items.

1.3 instrument performance

The accessibility of small sample sizes down to the 1 mm^2 -range was chosen as the leading design criterion for the reflectometer proposed here. Concentrating on small samples opens the possibility to use focusing optics for beam transport and beam shaping. The essentially new feature of the proposed reflectometer is the truly focusing (*Selene*-type) guide system. The secondary instrument parts, i.e. sample stage and environment, spin analysis and detector, are *conventional*.

The need to reach high q_z and thus high detector angles favours a horizontal scattering geometry. This is also supported by the fact that in this case gravity affects the beam profile and divergence only in the sample plane. The only restriction caused by the vertical sample plane is that liquid/gas and liquid/liquid interfaces can not be studied, and that sedimentation in liquid/solid cells might cause problems. But exactly these applications are the aim of the other reflectometer type proposed to the ESS.

The expected performance of the proposed reflectometer is

- maximum illuminated sample width 10 mm;
- minimum sample surface 1 mm^2 ;
- fulfilling the standard repertoire of time-of-flight reflectometers without compromises, e.g. specular and in-plane off-specular reflectometry;
- new operation modes are possible, e.g. with selectable constant resolution, or enabling high-speed specular reflectivity measurements by accepting a complex resolution function and a possibly higher background;
- for sample environment and add-ons like spin echo equipment there are several meters of free space around the sample position without compromising the performance;
- the scattering geometry is horizontal, leading to restrictions or even exclusion for certain soft-matter experiments, but allowing for high q_z and minor influence of gravity;

- a clearly defined beam footprint is possible and enables the concentration on a certain area on the sample, therefore allowing for raster scanning, for example;
- optical elements can be used to obtain a parallel beam for GISANS experiments, or a beam focused to the detector rather than the sample for focusing GISANS;
- in cooperation with Robert Georgii and Wolfgang Häußler from the Technical University Munich, we investigate the possibility to have a MIEZE set-up as an add-on. [→2.10.4]

To our knowledge there exists no neutron reflectometer with focusing in the scattering plane. First studies with add-on optics to realise this were performed on Amor@PSI [20] and at J-Parc. A prototype of a full *Selene* guide was built within the project leading to this proposal.[21] The original idea to combine angle-dispersive and energy-dispersive operation modes go back to F. Ott.[22, 23]

1.4 overlap with the soft-matter reflectometer

The vast majority of present-day experiments would in principle be possible on both the horizontal and the vertical reflectometers, where the choice depends on the suited resolution, polarisation (and analysis), sample size, and compatibility with sample environments and add-ons. Nevertheless, the expectations of cutting-edge science in both fields lead to the mutually excluding design criteria resulting in two reflectometers.

Since soft-matter samples often can be produced with surface area of 10 cm^2 to 100 cm^2 they would profit from a footprint larger than $\approx 1 \times 5\text{ cm}^2$, which is about the upper limit for the proposed instrument still giving a well defined resolution and footprint. Completely excluded on Εστία are measurements on gas/liquid or liquid/liquid interfaces due to the horizontal scattering geometry.² These experiments and the related design criteria form the key drivers for the other reflectometer to be built at the ESS. That one will also be able to profit from larger sample sizes.

Besides these constrictions, the proposed instrument can be used for typical soft-matter measurements as well — in some cases even opening up new possibilities: Measuring over a large sample size implies averaging over the whole surface area and thus details from inhomogeneities are completely lost. Focusing on very small surface areas ($\approx 1\text{ mm}^2$) will enable scanning the samples therefore detecting inhomogeneities within the sample plane with high detailed structure in the direction perpendicular to the interface. Thus, this reflectometer can be thought as a neutron profilometer that probes the density profile perpendicular to the interface on a mm scale, rather than just its outer morphology.

Also the power of the *Selene*-type reflectometer relies on the high intensity of its focusing concept. This implies that it will be able to measure in the sub-second time scale. The increase of diffuse scattering due to the much higher divergence in this mode is at least partially compensated for by the reduced sample size.

One essential requirement for the soft matter reflectometer is to cover a large q_z -range without moving the sample. This results in a short instrument using a broad λ -range, and most likely only moderate to low resolution. The proposed instrument selects a smaller λ -range, starting at higher λ so that it optimally uses the flux. This also leads to a higher intrinsic resolution.

1.5 user community, existing facilities

Neutron investigation techniques, namely neutron reflectometry, allows the non-destructive investigation of even very sensitive materials (such as soft condensed matter materials, biological specimens and tissues). Some 35 dedicated neutron reflectometer instruments are available worldwide at about 15 neutron sources (nuclear research reactors as well as spallation sources) for scientific purposes and user operations covering a wide q_z -range for the investigations. There exist some more neutron reflectometers for e.g. neutron optics testing or industrial applications.

One can roughly subdivide the existing neutron reflectometers into two types, one with horizontal scattering plane and another with vertical scattering plane. The latter ones are capable of measuring solid/liquid, liquid/liquid and liquid/air interfaces also, these reflectometers are often specially designed for investigating biological samples and self-organising soft matter molecules. The reflectometers with horizontal scattering planes are widely used for investigations in the branch of hard condensed matter, magnetism and superconducting materials, in almost all cases probing solid/solid interfaces exclusively. .

²According to the estimates of the reflectometry STAP this accounts for about 25% of all reflectivity experiments.

While the available neutron reflectometers at smaller sources are often designed as multi-purpose devices with vertical scattering geometry, larger facilities (such as ORNL, ILL, ISIS or FRM II) usually house more than one reflectometer, and there exist often the combination of a dedicated soft matter (vertical scattering plane) reflectometer, and a hard condensed matter (horizontal scattering plane) reflectometer in addition, to optimally exploit the appropriate q -ranges for the respective investigations.

The typical user request for beam time is much larger than the capacity of the existing reflectometers, typical overload factors range from 1.35 (EROS, Saclay) up to 2.2 (FIGARO, ILL). Depending on the instrument specialization, there is a growing demand for e.g. investigations at the air/water interface. Typical load factors for this type of reflectometry measurements at dedicated instruments range from 6% (REFSANS, FRM II) to 60% (FIGARO, ILL).

1.6 infrastructure & support facilities

The sample environment needed to cover the standard applications contains cryomagnets (state-of-the-art are 7 T, asymmetric field), cryostats, Helmholtz coils (for lower fields, often combined with a closed-cycle refrigerator), and in-situ furnaces. More specialised equipment as liquid/solid cells often is provided by the users. For these a device for thermalisation should be present at the instrument. A furnace for off-situ annealing, a glove box, and a fridge for sample storage should be accessible.

For sample preparation, a chemistry lab should be located not too far away. This is mainly needed by the soft-matter community, but it might also serve e.g. for (HF-) etching a substrate prior to in-situ growth studies.

For non-standard experiments like the in-situ growth studies, the equipment most likely will be provided by the users. But they still need supply of power, gases (N₂, Ar, He) and cooling (water).

It proved to be very helpful at PSI to have direct access to a small workshop in the experimental hall (also as a user), and to mechanical support on short notice. E.g. to modify or build adapter plates or sample holders.

2 Description of Instrument Concept and Performance

It is proposed to build a polarising reflectometer, optimised for samples of $10 \times 50 \text{ mm}^2$ area, or less, capable to cover a wide q_z -range with variable resolution. The scattering plane is horizontal to allow for wide detector angles. The unique feature of this instrument is its truly focusing guide system, which reduces background and illumination of sample environment, and which opens new possibilities for beam shaping and filtering.

In the following, the lay-out of the instrument is presented, followed by a presentation of the guide system and its key features. These strongly influence the design of the components presented thereafter. The essential parameters of the instrument are given in table 2.1.

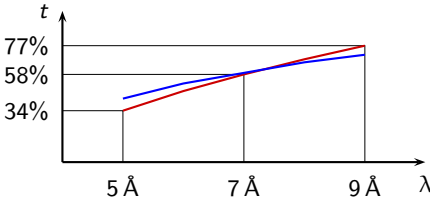
The final sections of this chapter deal with the operation schemes [→2.10], simulations [→2.11], and a discussion of the performance [→2.12].

2.1 instrument lay-out

The principle instrument lay-out is shown in figure 2.1. The various components are briefly presented here. A more detailed discussion follows in the next sections.

Table 2.1: Key features of the reflectometer for small samples.

parameter space		
q_z -range	$[0, 1] \text{ \AA}^{-1}$	to be covered in 5 measurements
λ -range	$[5, 9.4] \text{ \AA}$	
sample size	$[0.3, 50] \times [0.3, 10] \text{ mm}^2$	$x \times y$
maximum divergence	$\Delta\theta_{xy} = 1.5^\circ$ $\Delta\theta_{xz} = 1.5^\circ$	scattering plane sample plane
resolution		
intrinsic $\Delta\lambda/\lambda$	2.1%	5.0 \AA
	4.0%	9.4 \AA
$\Delta q/q = \text{constant}$	3%, 5%, 10%, ...	with multilayer monochromator
geometry		
scattering plane	horizontal	
total length	58.0 m	
sample / detector	6.2 m	
2θ	-2° to 50° (110°)	for $q_z \leq 1 \text{ \AA}^{-1}$ (2 \AA^{-1})
moderator		
cold		
guide transmission		
λ	t	
5 \AA	34%	42%
6 \AA	47%	52%
7 \AA	58%	59%
8 \AA	68%	66%
9 \AA	77%	71%



analytical, based on eqn. 6.5.2

McStas simulations

I source The instrument needs a cold moderator as neutron source, where the effective flux maximum (i.e. including losses and rescaling [$\rightarrow 2.5.1$]) determines the minimum wavelength λ_{\min} .

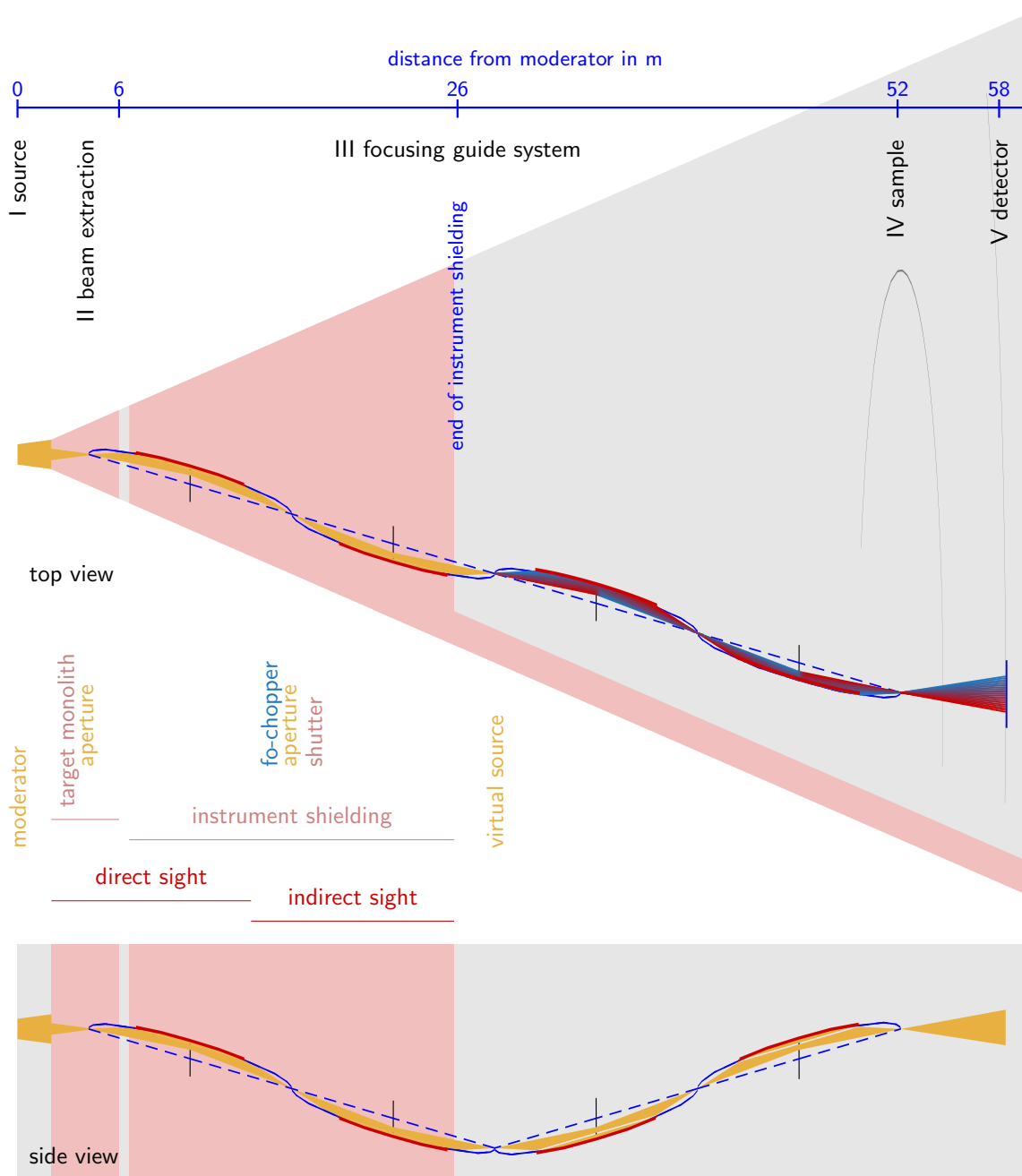


Figure 2.1: Sketch of the instrument lay-out. The direction normal to the beam is stretched by a factor 10 for clarity. The gray area in the upper sketch represents a 5° wedge on the floor. The detector will move outside this area for high angles. The light red area represents shielding, i.e. the target monolith, the common instrument shielding and individual instrument shielding. The thick red lines represent the *Selene* guide segments, where the blue lines give the shapes and the long axis of the related ellipses. The golden area is the beam path within the extraction unit and the first *Selene* guide section. For the second section the λ - θ -encoding mode is shown, where the λ is here encoded in a colour reaching from red to blue. (For the nomenclature of the components, please refer to chapter 5 and to figure 5.1.)

II beam extraction [→2.3] The purposes of the beam extraction unit are to form a $10 \times 10 \text{ mm}^2$ pin-hole at $x = 4.2 \text{ m}$, and otherwise to stop as many fast neutrons and γ radiation as possible.

III focusing guide system [→2.2] The essential difference of the presented instrument compared to conventional reflectometers is the truly focusing guide system.

Between the pin-hole, which forms a virtual source, and the sample, a focusing guide system is realised, based on the *Selene* concept. The complete guide system consists of 4 segments, each a 7.2 m long elliptically shaped reflector where the distance between focal points is 12 m. The use of 4 instead of 2 longer segments allows to get out of line of sight twice at $x \approx 25 \text{ m}$, and to use the mentioned pin-hole in the extraction unit.

This design was chosen to encounter the worst-case scenario for background caused by the primary and secondary spallation processes at and around the source, and along the beam guide.

The first 2 segments create an image of the pin-hole halfway down the guide ($x = 28.2 \text{ m}$, in the following referred to as *virtual source*), where precision beam-shaping and λ - and polarisation filtering is then performed. The last 2 segments focus the clean beam to the sample.

Additional beam-defining elements like slits, choppers, polarisers, and monochromators, can be located in the spaces at $x \in [25.8, 30.6] \text{ m}$, $x \in [25.8, 42.6] \text{ m}$, and $x \in [49.8, 52.2] \text{ m}$.

IV sample [→2.7] The sample is located at the final focal point at $x = 52.2 \text{ m}$. The *Selene* guide ends 2.4 m upstream the sample position. This and the focused beam (making a nearby slit obsolete) allow for installing voluminous sample environment.

V detector [→2.9] A position sensitive detector is located at $x = 58 \text{ m}$, where its angular resolution dominates the resolution of this instrument concept. For diffraction, a second, shorter detector arm allowing for higher 2θ can be installed.

2.2 Selene guide

task: deliver a focused beam to the sample with adjustable divergence and footprint

Since the *Selene* guide dominates the complete instrument lay out, it is presented first. Special aspects discussed in the appendix are: design considerations [→6.1], coma aberration [→6.3], and chromatic aberration due to gravity [→6.4].

The reason for using a truly focusing guide is that it allows for shaping the phase space required at the sample already at the guide entrance. This has the consequence that radiation issues and illumination of the sample environment are strongly reduced. It is important to notice that most other guide concepts based on elliptic guides are not exactly focusing: they suffer from strong coma aberration effects and create a divergent beam at the exit. [24, 25]

The *Selene* guide can be seen as an extended Montel optic [26] as used at synchrotron beam-lines. One guide segment consists of two planar-elliptic reflectors that are joined to form a gorge with L-shaped cross-section. The distance of the guide entrance to the virtual source at the initial focal point is chosen in a way to avoid multiple reflections for each reflector. The first guide segment creates an image at its second focal point which is blurred due to coma aberration. To correct for this, an identical guide segment is used, mounted parallel to the first one, but reflecting in the opposite transverse direction. This largely inverts the coma effect and re-establishes the image of the virtual source at the final focal point. A sketch of the guide geometry is shown in figure 2.2

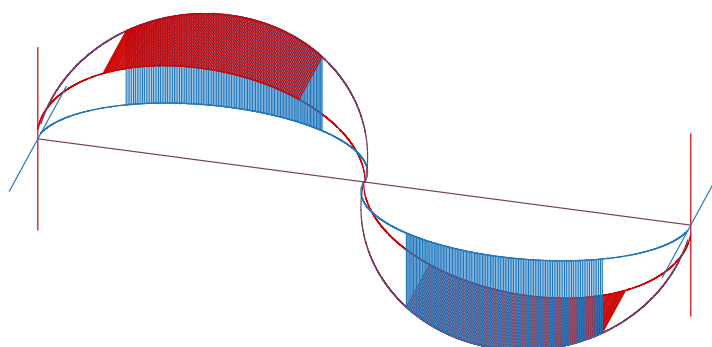


Figure 2.2: Sketch to illustrate the shape of the *Selene* guide. Shown are two segments with L-shaped cross-section, sharing the long axis (magenta) and a focal point.

Table 2.2: Parameters of the *Selene*-type guide. For a given instrument length of 58 m and $\Delta\theta_{xy} = \Delta\theta_{xz} = 1.5^\circ$ the following guide parameters are obtained by analytical calculations. [→6.1]

guide parameters		
c	6.0 m	half distance between focal points
ξ	0.6	effective length of the coated guide
b/a	0.01754	⇒ $b = 105.26$ mm, $a = 6000.92$ mm
distances		
moderator / pin hole	4.2 m	first focal point
$2c$	12.0 m	length of ellipses
$\xi \cdot 2c$	7.2 m	length of (coated) guide sections
$(1 - \xi) \cdot 2c$	4.8 m	space between guides
$(1 - \xi) \cdot c$	2.4 m	space before sample
sample / detector	[1.5 ... 7.5] m	high-angle diffraction vs. high resolution
Δz at sample	0 / 522.7 mm	vertical offset of one <i>Selene</i> section
Δy at sample	0 / 522.7 mm	horizontal offset of one <i>Selene</i> section
free space withing flight-path for beam- / pulse-shaping (distance from the moderator)		
$x =$	6.0 m → 6.6 m	gap behind target monolith
	13.8 m → 18.6 m	eventually frame-overlap chopper
	25.8 m → 30.6 m	precise beam-shaping, polarisation
	37.8 m → 42.6 m	
	49.8 m → 52.2 m	before sample
coating		
m	3.0	critical edge
coated area	4 m ²	
material	Ni/Tisupermirror	

The guide system for the presented reflectometer consists of two such *Selene* guide sections: The first has to create a virtual source with defined size and divergence, but twice out of line-of-sight from the moderator. This virtual source is in a low-radiation region so that sensitive mechanical equipment and optics can be used there. It is also possible to access this area for maintenance during operation (with the instrument shutter closed). At and around the virtual source point, the beam is shaped as is necessary for the measurements. The shape and orientation of the footprint of the beam on the sample can be defined by an appropriate slit system. The second *Selene* guide has to map the shaped beam to the sample. The divergence (and eventually the incident angle) of the beam are defined by slits before or after the guide segments. This way spot-size and divergence are adjusted independently.

The use of two *Selene* guides has the consequence that each neutron is reflected exactly 8 times before it arrives at the sample. The resulting reduction in intensity is the price one has to pay for low radiation and for convenient beam manipulation. [→2.5.1]

Table 2.2 gives the geometrical parameters of the ellipses, the measures of the guide and the coating.

2.3 beam extraction

task: transport the requested phase space volume outside the target monolith, while reducing the radiation as much as possible

Within the first 6 m the only *optics* needed is a pin-hole at $x = 4.2$ m acting as a virtual source for the first *Selene* guide section. The location is chosen to accept the required divergence of $\Delta\theta = 1.5^\circ$ from the 120×120 mm² wide moderator. The extraction insert consists of some highly γ and neutron absorbing material (e.g. copper).

To take the expected settling of the ground into account, the pin-hole size can be increased. The *Selene* guide will still pick up about the same phase space volume, but the radiation shielding gets weaker. This has to be compensated for by increased shielding along the beam guide.

There is no restriction when it comes to including a maintenance shutter in the monolith or in the extraction insert at any position.

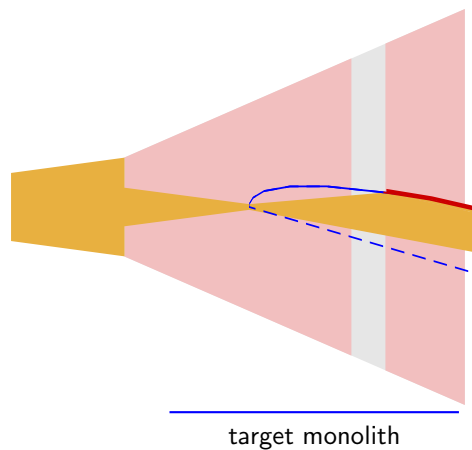


Figure 2.3: Sketch of the beam extraction section with a pin hole. A small ($10 \times 10 \text{ mm}^2$) aperture 4.2 m from the source acts as virtual source and defines the initial focal point for the first *Selene* guide section. This position allows for a divergence of $\Delta\theta_{xy} = \Delta\theta_{xz} = 1.5^\circ$. The openings of the flight path section are 68 mm / 58 mm at the entrance / exit of the target monolith.

2.4 shielding

It is inherent to the *Selene* guide concept that neutrons are reflected on each reflector exactly once, so that the complete beam has changed its direction when leaving a guide segment. An absorber opposing the centre of the reflector blocks all direct trajectories. This means that within each segment one gets out of line of sight from its initial focal point. The guide dimensions and the wide free spaces before and behind the segments enable efficient shielding. Thus after the second segment one is out of line of sight twice with respect to the moderator and its environment, as is required by the ESS [→8.2]. There is space for a vacuum housing and mounting equipment around the guide. The guides' open construction (it forms an L, rather than a rectangle) allows for a tight shielding on two sides, the support mechanics can be mounted on the other sides.

Figure 2.4 shows the shielding concept for the first *Selene* guide section including the target monolith. Behind the monolith there is a gap of 600 mm until the first guide starts. Unless used for filters or a shutter, this gap can be filled by an extension of the insert.

The first and second guide elements are enclosed in a heavy concrete block. In the sketch at least 50 mm free space between guide and shielding are assumed for support, alignment devices, and vacuum housing. Because the dimensions of the openings are about 3 times the actual guide width, additional shielding is needed before and after the concrete shielding. These masks are supposed to consist of copper (displayed in blue). The area directly irradiated from target and moderator ends at the exit of the first concrete block at $x = 13\,800 \text{ mm}$. The indirectly irradiated area ends at $x = 25\,800 \text{ mm}$, i.e. less than half way between source and detector. In the gap $x \in [14, 18] \text{ m}$ optical elements, the instrument shutter and a frame overlap chopper can be installed, again surrounded by a concrete shielding.

The support system for the guides needs more space than just the $160 \times 160 \text{ mm}^2$ within the channel. Swiss-Neutronics suggested to use a granite beam to support the guide. This could also be part of the shielding, with appropriate shape to prevent straight holes parallel to the channel. Whether granite is suited for this purpose has to be investigated. On the other side, one could use a heavy concrete beam as support, if it is stable enough also against thermal influences.

The second *Selene* guide section will also need some shielding, but since neither thermal or fast neutrons, nor γ -radiation should reach this region, only a moderate boron-based absorber should be sufficient. To ensure the absence of fast neutrons, a sapphire filter can be inserted behind the concrete shielding.

2.4.1 MCNPX simulations

Based on the model given in figure 2.4 MCNPX simulations have been performed by U. Filges, PSI. The results are summarised in table 2.3. These tell that the proposed geometry and dimension of the *Selene* guide allows for a shielding which fulfils the requirements by the ESS. Just outside direct line of sight the dose rate is $37 \mu\text{Sv h}^{-1}$, and it drops below the computational threshold at the end of the shielding. The simulations took 7 days on a cluster with 7×24 cores.

2.4.2 shutter

An instrument shutter can be placed in the gap between the first and the second guide segments. This region is already out of line of sight from the moderator, so that only secondary radiation and cold neutrons transported by the guide have to be blocked.

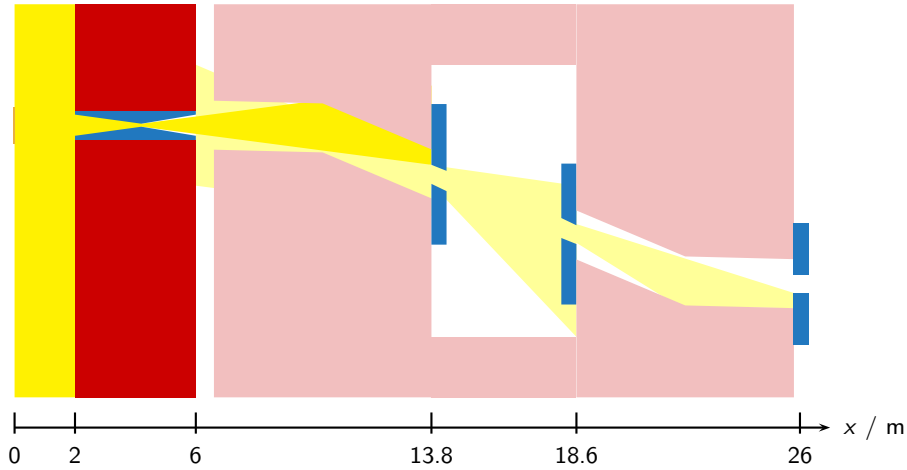


Figure 2.4: Sketch of the fast neutron and γ shielding concept. Here a vertical cut through the shielding is shown, following the beam in horizontal direction. The guide geometry and thus the shielding is the same horizontally and vertically. The source (moderator) is represented by the brown rectangle on the left. The red area stands for the monolith, the blue insert is the extraction unit. The pale red area represents heavy concrete shielding (or a sandwich of various moderators and absorbers), which hosts the guide elements. Additional masks (here blue) are needed to block the opening outside the neutron beam path. The area directly illuminated from the source is shaded yellow, the indirectly illuminated area is pale yellow. The neutron guides are not shown.

position	x / m	y/z position	dose rate / $\mu\text{Sv h}^{-1}$		flux / $\text{s}^{-1}\text{cm}^{-2}$	error
			γ	neutron		
exit common shielding	14.5	in beam	37	78 000	$9.3 \cdot 10^4$	7%
		off beam	37	10 000	$1.6 \cdot 10^4$	7%
entry instrument shielding	18.1		8	1 400	$2.5 \cdot 10^3$	20%
exit instrument shielding	26.5	in beam	—	—	—	—
		off beam	—	—	—	—
5 m behind shielding	31.5	in beam	—	—	—	—

Table 2.3: Dose rates and flux calculated with MCNPX for various positions along the guide. The source was assumed to be continuous with a power of 5 MW. This means that the peak dose and flux are a factor 30 higher. The computational statistics was too low for the positions marked with —.

2.5 energy- and time-range

The time and energy characteristics of the ESS long-pulse source allows for a relatively wide λ -range, while keeping the intrinsic instrument resolution below $\approx 4\%$, and avoiding the proton pulse time for measurements. A full reflectivity curve is thus achieved by piecing together (a few) measurements with varying angle of incidence. Further stitching due to complex chopped beam characteristics is not necessary.

2.5.1 flux and λ_{\min}

The experience with existing TOF reflectometers is, that the lower limit of the wavelength spectrum λ_{\min} corresponds to the effective flux maximum at the sample position. The reason is that even smaller λ result in higher q_z and thus in general in lower reflectivity, and at the same time in lower incident intensity. Thus the accuracy of the data rapidly decreases and it is much more appropriate to measure at a higher angle of incidence to access the corresponding q_z -range.¹

The effective flux at the sample can be estimated by reducing the initial flux $I_0(\lambda)$ by the losses due to reflections on the guide walls, and by taking into account that in the end one aims for $\Delta q/q = \text{constant}$ or close to constant.

¹In case the width of the q_z -range covered within one pulse is essential, one might accept also a smaller λ_{\min} for the cost of a dramatically increased measurement time.

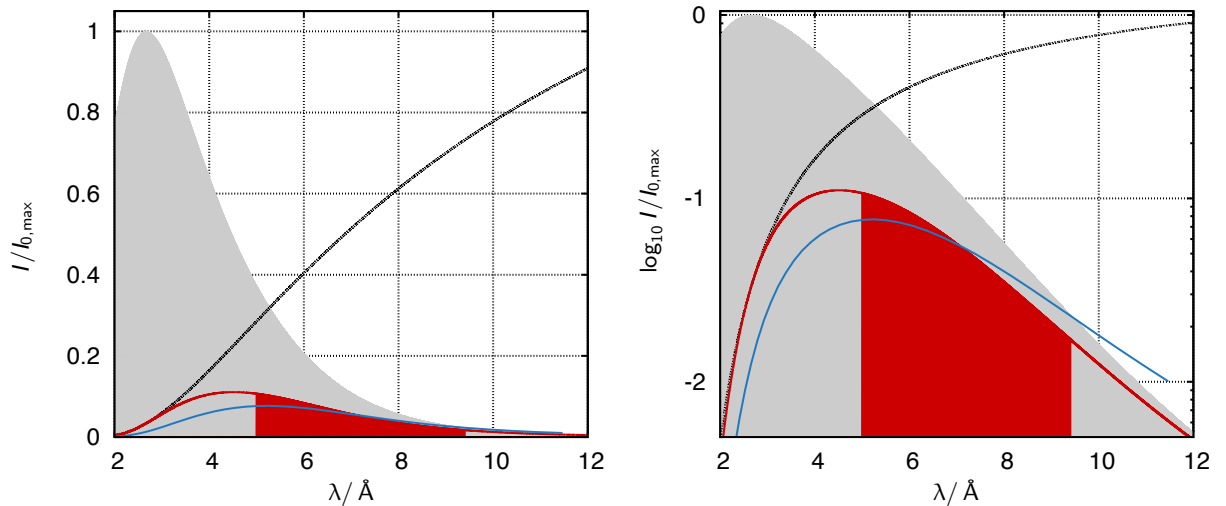


Figure 2.5: Spectra $I(\lambda)/I_0$ (left) and $\log_{10} I(\lambda)/I_0$ (right) as given by the source (gray area), after attenuation according to eqn. (6.5.2) with 8 reflections (red line), and after re-binning it to $\Delta\lambda/\lambda = 2\%$ (blue line). The latter line is scaled by an arbitrary value. The black line is the transmission of the guide. The source spectrum $I_0(\lambda)$ is the one used by the McStas component `ESS_moderator_long`. The red area represents the neutrons actually arriving at the sample.

The double *Selene* guide concept involves 8 reflections for all neutrons on surfaces with a non-perfect reflectivity R . Since the angle of incidence on the guide surface hardly varies along the guide for the presented concept, one can assume an attenuation of $I(\lambda) \approx I_0(\lambda) \cdot R(\lambda)^8$.

A more prominent effect comes from the required $\Delta q/q = \text{constant}$: effectively, the time-bins, and thus the λ -bins necessary for $R(q_z)$ curves follow $\Delta\lambda/\lambda = \text{const}$, which shifts the spectral weight to bins with larger λ . This shift can be approximated by $I(\lambda)_{\Delta\lambda/\lambda = \text{const}} \propto \lambda \cdot I(\lambda)_{\Delta\lambda = \text{const}}$

This way the minimum wavelength $\lambda_{\min} = 5 \text{ \AA}$ was determined, as illustrated in figure 2.5.

2.5.2 time regime and λ_{\max}

In order to avoid a contamination of the measurement with background originating from the proton pulse and secondary processes, the instrument's length was chosen so that the 5 \AA neutrons arrive at the detector right after a pulse. This leads to a minimum length (moderator to detector) of 58 m. And the time between pulses sets the upper wavelength limit to $\lambda_{\max} = 9.4 \text{ \AA}$. Figure 2.6 shows the corresponding t - x -diagram.

To also avoid a contamination of the signal used for normalisation, the monitor is located so that it measures in the first frame. An ideal position is right behind the exit of the second guide at $x \approx 26 \text{ m}$ (dashed line in figure 2.6).

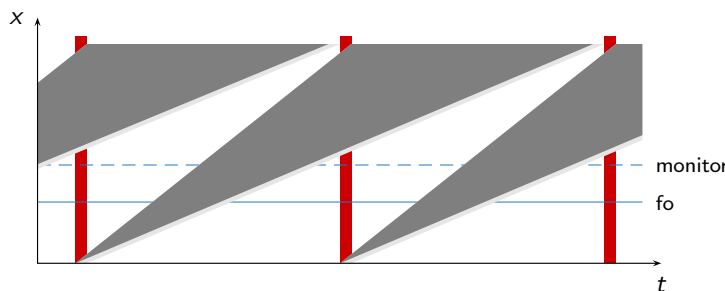


Figure 2.6: Sketch to illustrate how to avoid the influence of the γ and fast neutron burst from the proton pulse hitting the target. The sketch is to scale with period $T = 70 \text{ ms}$, pulse length $t = 3 \text{ ms}$, and a sample detector distance of 58 m, i.e. $\lambda \in [5, 9.4] \text{ \AA}$. The dashed and solid blue lines correspond to the location of the monitor and frame-overlap chopper, respectively.

2.5.3 intrinsic λ resolution

The time- and thus the λ -resolution is $\Delta\lambda \approx 0.2 \text{ \AA}$, given by $\lambda \in [5, 9.4] \text{ \AA}$, the moderator-detector distance of $X = 58 \text{ m}$, and the pulse length τ . [→8.3.1] This leads to $\Delta\lambda/\lambda = 2.1\%$ at $\lambda = 9.4 \text{ \AA}$, and $\Delta\lambda/\lambda = 4.0\%$ at $\lambda = 5.0 \text{ \AA}$.

2.5.4 frame-overlap suppression

A frame-overlap chopper will be installed close to the focal plane within the first guide section at $x = 16.2 \text{ m}$ (blue line in figure 2.6). The beam cross-section there is $\approx 30 \times 30 \text{ mm}^2$. This chopper, running with the source frequency, suppresses all neutrons below 5 \AA , and all neutrons above 9.4 \AA , with windows at $\lambda \in [22.1, 26.5] \text{ \AA}$, $\lambda \in [39.2, 43.6] \text{ \AA}$, and so on. To *close* these windows, neutrons with $\lambda > \lambda_{\max} = 9.4 \text{ \AA}$ will also be suppressed by using a transmission filter. A silicon wafer with a Ni coating ($m = 1$) shaped like a logarithmic spiral [→7.1] is installed before the virtual source. The shape assures that all trajectories pointing towards the virtual source hit the wafer at the same angle (here 0.95°). For neutrons with $\lambda < \lambda_{\min} = 5 \text{ \AA}$ the coating of the guide acts as an attenuator.

2.5.5 choppers

The frame overlap chopper is discussed in the section above.

For this instrument and the operation schemes presented in section 2.10 no pulse-shaping choppers are foreseen.²

2.6 polarisation

Neutron spin polarisation and its analysis are key-features of the reflectometer for small samples. Based on the demand nowadays one can estimate that at least 50% of the measurements will need a polarised beam, and some 10% also polarisation analysis.

The concepts presented below are either well established, or under development so that there is no unknown risk connected. Besides for the permanent coating, the options can be altered later on.

2.6.1 permanent polarisation

A permanent polarisation can be achieved using an appropriate coating on (one side of) one guide segment. This has the advantages that off-specular scattering from the coating will not hit the sample, and that the distance from a high magnetic field at the sample position is sufficiently large to prevent depolarisation.

2.6.2 optional polarisation

In case the 50% intensity loss due to polarisation is not accepted, there are several approaches possible:

polarising (double bounce) reflector The ML monochromator used for λ - θ -encoding or any reflector close to the initial focal point can have a polarising coating.

polarising filter By using a transmission filter with the shape of a logarithmic spiral as discussed in section 7.1 it is possible to polarise a divergent beam emerging from a small source with a moderate m of the SM coating (and thus a high polarisation efficiency).

E.g. a combined λ low-pass and polariser for $\lambda \in [5, 10] \text{ \AA}$, $\Delta\theta = 1.5^\circ$, and a distance of the polariser from the focal point of 300 mm leads to a device of $\approx 1 \text{ m}$ length. The polarising coating has $m = 2$.

³He polariser The small beam size close to the initial (intermediate) focal point allows for the operation of a rather small ³He cell. Typically with a cross-section of a few cm^2 , only. In addition, the long distance from this point to the sample avoids depolarisation due to high magnetic fields at the sample position.

2.6.3 analyser

The different beam geometry behind the sample demands for more complex and larger devices.

² Since the *Selene* guide system in the end fulfils the same task as a *normal* guide, it could be combined with multi-chopper setups for Repetition Rate Multiplication or for Wavelength Frame Multiplication [27]. In the large free regions between the guide segments of the *Selene* guide this would not cause any modifications to the guide. A chopper within the reflecting part results in gap in the divergence distribution.

analysing filter This is the analogue to the polarising filter, but it is not realistic to install it some 300 mm behind the sample. Thus a larger multi-channel device directly in front of the detector has to be build. This is a new concept and has not been tested yet.

wide-angle analyser based on supermirrors A SM-based multi-channel bender can be installed directly in front of the detector. Similar devices are in operation at FOCUS@PSI and at HYSPEC@SNS.

^3He analyser The wide divergence and the needed distance from the sample (to avoid the influence of the sample magnetic field) mean that a large ^3He vessel is needed.

2.6.4 flipper

RF flipper The divergent polychromatic beam can be flipped by using a Radio Frequency flipper.[28, 29]

RSF flipper An alternative approach for monochromatic beams changing the wavelength with time is a Resonance Spin Flipper.[30]

switchable remanent coating For the devices based on SM coatings for polarisation / analysis one can use magnetically remanent coatings, allowing for flipping the polariser, rather than the beam.[31]

2.7 sample stage

The sample stage is the same as for conventional reflectometers. It either uses a hexapod or a classical tower of translation- rotation-, and tilting-stages.

The position of the stage on the floor might vary with the alignment and the operation mode of the instrument. This means that a x-y translation stage (or a platform on air-pads) can form the basis.

Since the sample environment can be quite heavy and voluminous, the sample stage will be able to handle weights of up to 1 t. The *free* space between the platform and the sample is at least of the order of 300 mm. In table 9.1 a possible set-up of translation and rotation devices is listed. The complete sample stage will be non-magnetic, because one principle application of this instrument will be the measurements in high magnetic fields.

The guide ending 2.4 m before the sample leaves enough space for a fast slit system [→2.8.3] and even bulky sample environment devices like troughs or cryomagnets. Also equipment for complementary measurements like UV or X-ray will find space.

2.8 beam shaping

2.8.1 beam definition

The beam shape at the sample position is essentially defined in between the two *Selene* guide sections, 24 m upstream. The symmetry of the problem tells that the same degree of freedom will be needed there as at the sample stage [→2.7], but with a much reduced demand concerning load and magnetic influences.

Since the focal point position can only change due to misalignment of the first *Selene* guide section, the base-x-y translation needs to cover only a small area.

2.8.2 apertures within guides

To block the direct line of sight through the *Selene* guide and to reduce the divergence, one-sided apertures are positioned close to the centres of the 2nd guide segment for both guide sections. The one in the first guide is rather heavy, but does not need to be very accurate, since it should just reduce the radiation level outside the shielding. The apertures in the second guide will be used for precise beam divergence definition and thus need to be very accurate. On the other side, the blades are much thinner and thus lighter.

2.8.3 fast aperture

Behind the *Selene* guides, some 2.2 m before the sample, a precise and fast slit system will be installed. For the conventional operation mode it defines the angle of incidence and the divergence. *Fast* here means that position and opening of the slit can be varied between pulses within 10 ms. Slower operation is possible by dropping one or several pulses.

If technically possible [→3.4] it could also be used in the λ - θ -encoding mode, to cut down the unwanted off-specular intensity from the monochromator by scanning the slit across the beam during one pulse.

2.9 detector

2.9.1 area detector

For the reflectometry measurements one position sensitive detector is needed. The technology available today (2 mm resolution, area $400 \times 400 \text{ mm}^2$) would work. But higher resolution and a wider area would improve the instrument's performance. In principle, the instrument could be upgraded with a *better* detector once it is available without affecting the rest of the instrument. There is no preference for any detector technology from our side. Table 2.4 gives the (realistic) wish-list of the detector properties. [→9.2]

	state-of-the-art	ideal parameters
size	$400 \times 400 \text{ mm}^2$	$500 \times 170 \text{ mm}^2$
resolution horizontal	2 mm	$\leq 0.5 \text{ mm}$
resolution vertical ³	2 mm	$\geq 1 \text{ mm}$
rate at 5 \AA		$5 \cdot 10^8 \text{ s}^{-1} \text{ \AA}^{-1}$
rate at 9.4 \AA		$2 \cdot 10^8 \text{ s}^{-1} \text{ \AA}^{-1}$

Table 2.4: Key parameters for the area detector. The numbers of the state-of-the-art detector were given by R. Hall-Wilton, ESS. ($\Delta\lambda \approx 0.2 \text{ \AA}$)

2.9.2 single detector

For diffraction measurements on the films or the substrates a second (single) detector on a shorter 2θ arm might be used. This possibility proved to be useful e.g. to check possible bending or twinning upon cooling.

2.9.3 CCD camera

To align the guide and to monitor its performance, and also for aligning the sample, a CCD camera in front of the area detector can be used. This has the advantage that the resolution is much higher, while its draw-backs of high noise and low efficiency do not play a role for this purpose.

The active area should be some $150 \times 150 \text{ mm}^2$, the resolution about $0.1 \times 0.1 \text{ mm}^2$.

2.10 operation modes

In figure 2.7 the three principle operation modes are sketched, and the corresponding λ - θ detector diagrams are shown. A short description is given below, and an extensive discussion including data acquisition and reduction is given in the appendix [→10].

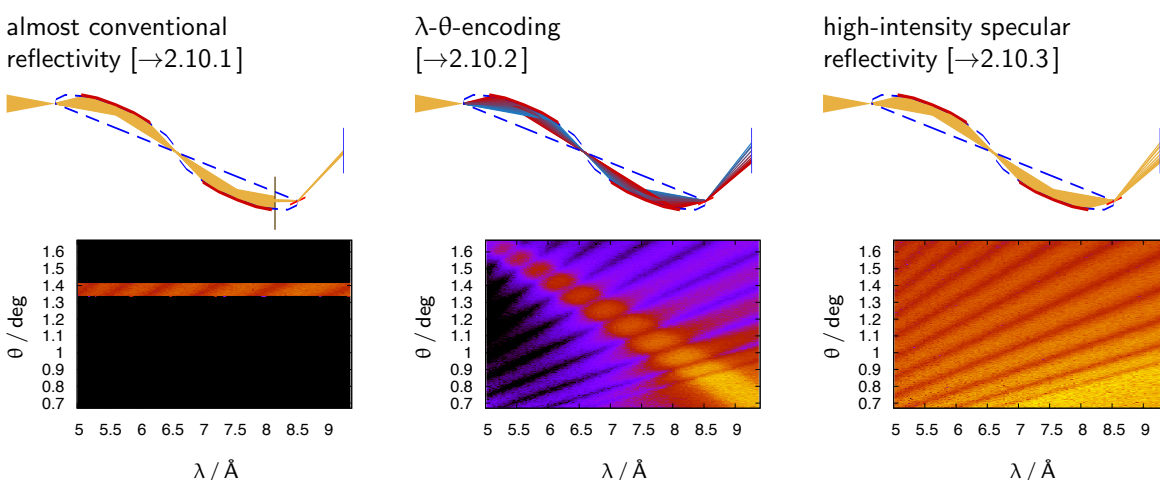


Figure 2.7: Operation schemes and $I(\theta, \lambda)$ maps obtained by simulation [→2.11] assuming a 1000 \AA thick Ni film on glass as sample: using a slit before the sample, using a multilayer monochromator for angle-wavelength-encoding, and using full divergence and pulse.

³Unless used for GISANS, the detector could be integrating vertically, i.e. no spatial resolution would be required

2.10.1 almost conventional & off-specular reflectivity

[→10.1] Though still giving a convergent beam to the sample, this mode is quite close to the operation scheme of conventional TOF reflectometers. An aperture 2.2 m before the sample defines the divergence $\Delta\theta$. The wavelength is obtained by the time-of-flight, and θ is adjusted by rocking the sample. The λ resolution is given by the pulse length and varies from 2.2% (9.4 Å) to 4% (5 Å).

Because of the decoupling of beam spot size and divergence in the *Selene* guide, the footprint on the sample surface is defined by the aperture at $x = 28.2$ m. Over-illumination of the sample and illumination of the sample environment can be suppressed.

By moving the divergence-defining aperture within the θ -range of the beam leaving the guide, one can change θ_i without tilting the sample.

Figure 2.8 shows intensity maps (left), and the reflectivity curve extracted therefrom (right). These data were obtained by simulation.

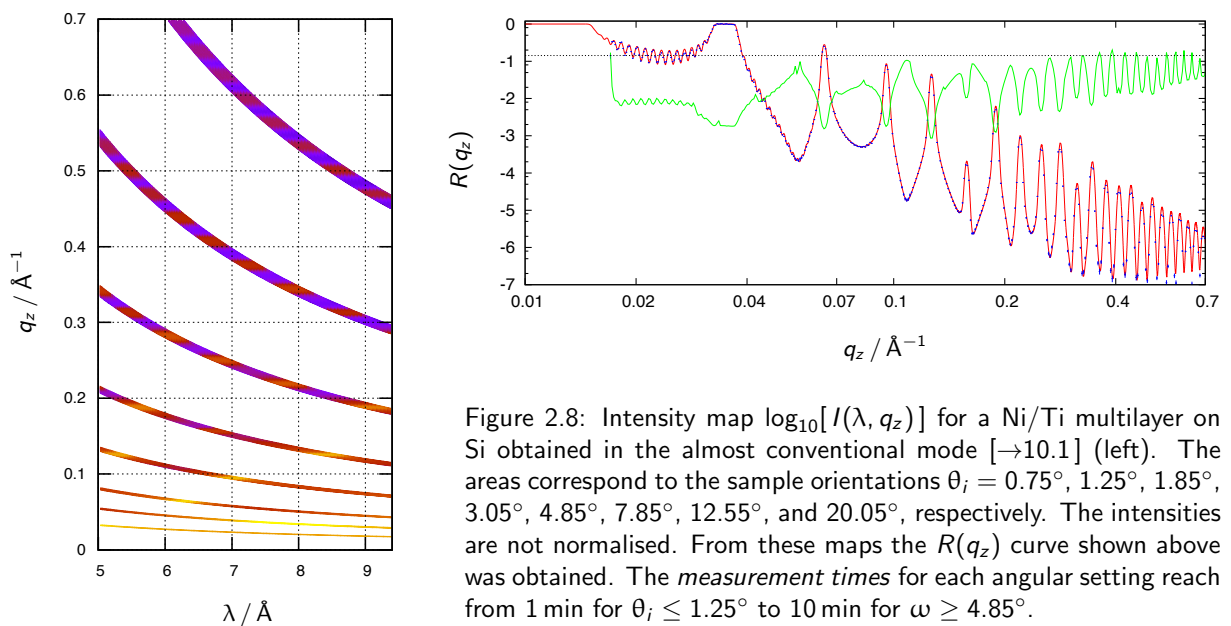


Figure 2.8: Intensity map $\log_{10}[I(\lambda, q_z)]$ for a Ni/Ti multilayer on Si obtained in the almost conventional mode [→10.1] (left). The areas correspond to the sample orientations $\theta_i = 0.75^\circ, 1.25^\circ, 1.85^\circ, 3.05^\circ, 4.85^\circ, 7.85^\circ, 12.55^\circ, \text{ and } 20.05^\circ$, respectively. The intensities are not normalised. From these maps the $R(q_z)$ curve shown above was obtained. The *measurement times* for each angular setting reach from 1 min for $\theta_i \leq 1.25^\circ$ to 10 min for $\omega \geq 4.85^\circ$.

This mode will be needed to align the sample, and for measuring (or discriminating) off-specular scattering.

off-specular scattering In this mode off-specular scattering can be measured exactly in the same way as on conventional TOF reflectometers. Without using pulse shaping choppers the q_z resolution is essentially given by $\Delta\lambda \propto \tau$. The q_x resolution varies strongly as a function of λ and θ_f .

2.10.2 angle-energy-encoding

[→10.2] Compared to the almost conventional mode there are two essential differences: It allows to cover a wider q_z -range in one shot by relating λ_{\max} to small θ and λ_{\min} to large θ . And while λ is encoded in θ , it has the resolution $\Delta\lambda/\lambda = \Delta\theta/\theta$. This means that the resolution can be manipulated without pulse shaping, so no choppers are needed.

The encoding is achieved by using a (double bounce) multilayer monochromator before $x = 28.2$ m. To get a clean beam, a fast slit system 2.2 m before the sample is necessary to scan θ within one pulse.

Figure 2.9 shows intensity maps obtained by simulation for this operation scheme.

off-specular scattering Also in this mode off-specular scattering can be measured. Since the specular scattering occupies the diagonal of the λ - θ diagram, the off-specular *area* consist of two triangles. The q_z resolution is almost constant, the q_x resolution varies strongly as a function of λ . Figure 2.10 compares the q_x - q_z area covered by the almost conventional and the λ - θ -encoding mode.

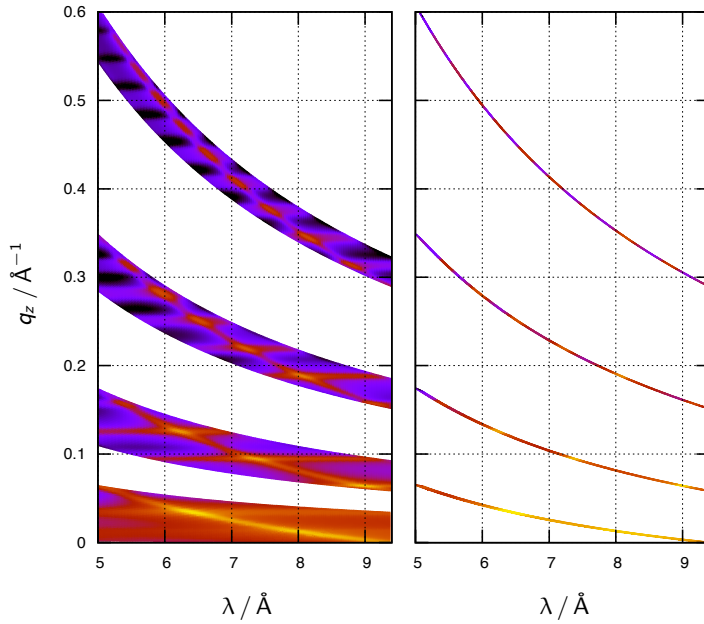


Figure 2.9: Intensity map $\log_{10}[I(\lambda, q_z)]$ for a Ni/Ti multilayer on Si obtained in the λ/θ -encoding mode [→10.2]. The 4 areas correspond to the sample orientations $\omega = -0, 5^\circ, 2^\circ, 6^\circ, \text{ and } 12^\circ$, respectively. The intensities are not normalised. The left maps show the signal after transformation of t to λ and θ to q_z . In the maps on the right side the areas where only off-specular intensity is expected (assuming a perfect monochromator) are shaded.

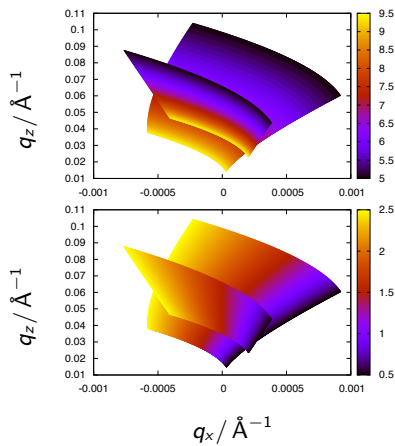


Figure 2.10: q -space covered by off-specular measurements in the λ - θ -encoding mode (larger area) and in the almost conventional mode (smaller, more distorted area). In the top map, λ and in the bottom map θ is plotted as a function of q_x and q_z . The detector was assumed to cover $\theta_f = 0.5^\circ$ to 2.5° , and $\theta_i = 1.5^\circ$ in the conventional mode.

accuracy In the λ - θ -encoding mode it is essential that the reduction of the λ -resolution induced by angular error is below the desired $\Delta\lambda/\lambda$. The encoding is given by $\lambda = 4\pi \sin(\theta_s + \omega_m - \omega_s)/q_m$ with the coating of the monochromator having a Bragg peak at q_m , and the monochromator and sample angles $\omega_{m/s}$. An angular error $\Delta\alpha$ caused by a misaligned guide or by waviness leads to a wrong θ and thus to $\Delta\lambda \approx 4\pi \sin \Delta\alpha/q_m$. If the angular error is so large that the beam misses the sample, the error does not cause a reduction of the resolution, but it just leads to a reduction of the reflected intensity.

For a 10 mm long sample and $\omega_s = 10^\circ$ the projected sample height is ≈ 2 mm. This corresponds to angular errors of 0.006° to 0.025° along the last guide segment, and thus to $\Delta\lambda < 0.02 \text{ \AA}$. This can be neglected. So in most cases an imperfect guide will result in a reduced intensity on the detector (the dark lines seen with the prototype set-up), but the encoding is still valid.

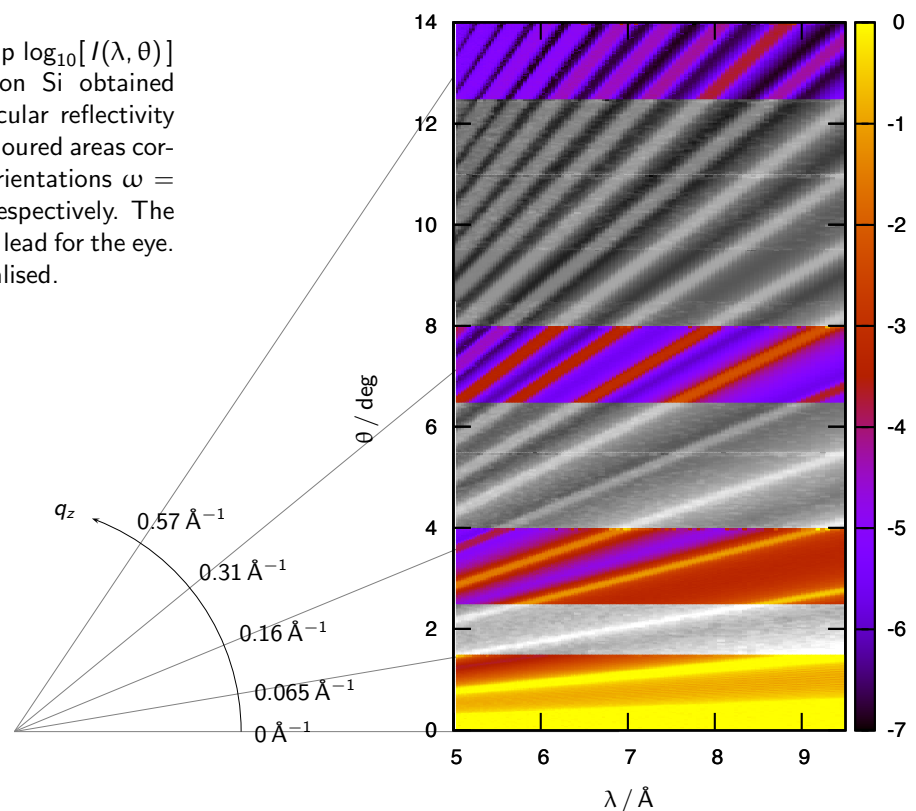
2.10.3 high-intensity specular reflectometry

[→10.3] This is the operation mode which delivers the most flux to the sample. The full divergence and also the full wavelength band accepted by the instrument are used. The wavelength is encoded in the time of flight, and thus the resolution is given by the pulse length of the source. The angular resolution is determined by the spatial detector resolution and the sample-to-detector distance.

The measured signal on the position sensitive detector is a $I(t, z)$ map which can be transformed into a $I(\lambda, \theta)$ map. Each row corresponds to a TOF measurement at a given θ , and each column corresponds to an angle dispersive measurement for a given λ . This means that one combines the two conventional reflectometry set-ups to increase the specularly reflected intensity. [21] However, a disentangling of an off-specular signal is a challenge.

Figure 2.11 shows an intensity map obtained by simulation, which illustrates the principle and the flux gain of this mode.

Figure 2.11: Intensity map $\log_{10}[I(\lambda, \theta)]$ for a Ni/Ti multilayer on Si obtained in the high-intensity specular reflectivity mode [$\rightarrow 10.3$]. The 4 coloured areas correspond to the sample orientations $\omega = -0, 5^\circ, 2^\circ, 6^\circ, \text{ and } 12^\circ$, respectively. The gray-scale areas are just a lead for the eye. The intensities are normalised.



Thus this mode can be used

- on tiny samples where one is satisfied if some reflectivity curve can be obtained in a reasonable time,
- on samples with negligible off-specular or incoherent scattering,
- to screen the dependence of $R(q_z)$ on temperature, electric or magnetic fields, surface tension, or the like, and
- to perform time-resolved measurements on a split-second time scale.

There is no simple answer to the question of how much off-specular scattering from the sample itself, from the optical elements, or scattering from the sample environment affect the measurements. But it is no problem to check this whenever necessary: A comparison of $R(q_z)$ obtained in the almost conventional mode (achieved by just closing a slit) and in the high-intensity mode immediately shows how strong the influences are.

2.10.4 further options

The following options are not yet investigated in detail. If necessary analytical or numerical simulations will be made.

focusing SANS The fact that the *Selene* guide gives a strongly focused beam can be directly used for setting up a focusing small angle scattering scheme. A detector has to be placed in the focal plane (where otherwise the sample is located), and the sample is positioned behind the guide end, some 2 m before the detector. This set-up gives an angular resolution of $\approx 0.03^\circ$. The sample size can be up to $52 \times 52 \text{ mm}^2$ (using the full divergence of 1.5° and the minimum resolution).

GISANS There are two principle modes of how GISANS could be realised. One can convert the focused beam into a parallel beam by using a parabolic reflector [$\rightarrow 7.2$]. This concept can be applied in the sample plane and in the specular scattering plane independently. The divergence of this beam is defined by the size of the virtual source. The width of the beam depends on the distance of the reflector from the focal point and can thus be tuned.

B. Hjörvarsson suggested another approach: Using the convergent beam for GISANS results in a convolution of the detector image with the angular resolution function. While this is constant for all λ , the GISANS map

on the detector scales with $1/\lambda$. Using the TOF data and the known resolution function should thus allow for a rather precise deconvolution of the detector image. Since the divergence of the incoming beam can be modified in both directions independently, one can tune the resolution function.

Rainbow The approach to spectrally analyse the reflected beam using a prism behind the sample [32, 33] can be realised if the beam is made parallel in one direction, e.g. by a parabolic reflector as described above. The detector resolution and distance allows for a high angular resolution needed for this method. The combination with TOF can be used for the measurement of inelastic processes. (The *rainbow* concept is mainly suited to reduce counting time on continuous sources.)

MIEZE A group at TUM including R. Georgii, W. Häußler and G. Brandl investigates the possibility to use a *Selene* type guide system for a dedicated MIEZE (Modulation of Intensity by Zero Effort) instrument.[34] Their know-how can be used to develop an add-on MIEZE set-up for the proposed instrument. The coils can be located before the third or fourth guide segment, and before the sample. The elliptic shape of the guide guarantees the same length for all trajectories. Figure 2.12 illustrates the short version of the MIEZE set-up.

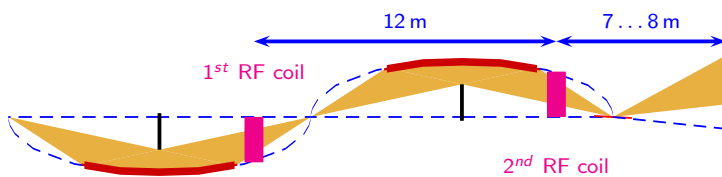


Figure 2.12: Sketch to illustrate the combination of MIEZE and a *Selene* guide.

2.11 simulations

Based on the parameters given in the previous section, an instrument file for McStas was developed (T. Panzner) and a series of simulations were performed.

Figure 2.7 shows sketches of the selected operation modes and the corresponding $I(\lambda, \theta)$ maps as detected with a 1000 Å Ni film on Si as a sample. The sample size was $5 \times 5 \text{ mm}^2$. From these and a second set of maps obtained at a higher angle the reflectivity curves shown in figure 2.13 are obtained.

- a) λ - θ -encoding [\rightarrow 2.10.2] by using a ML monochromator after the beam extraction.

This results in a diagonal streak in the λ/θ space, where $\Delta\lambda/\lambda = \Delta\theta/\theta = \text{const}$. In the off-diagonal region the finite reflectivity of the ML monochromator leads to some structured background. This does not affect the specular reflectivity, but it might prohibit off-specular measurements.
- b) High-intensity specular reflectometry [\rightarrow 2.10.3] by substituting the ML monochromator by a supermirror.

Here all of the available λ/θ space is used for specular reflectometry. Off-specular and incoherent scattering leads to an enhanced background. This mode allows for a fast (and dirty) screening of external parameters as e.g. temperature or magnetic field strength, and for time-resolved studies.
- c) Almost conventional reflectometry [\rightarrow 2.10.1] by using a slit to cut down the divergence given by the set-up (b).

The specular reflectivity concentrates on one line, while the rest of the λ/θ space is available for off-specular measurements. The q_z -range accessible this way is reduced. A movement of the slit between pulses can be used to vary θ without tilting the sample.

From these maps the reflectivity curves shown in figure 2.13 were obtained by integrating the λ/θ maps along constant q_z . The binning was done with $\Delta q_z/q_z = 1\%$. The error-bars shown were obtained by assuming $\Delta I/I = \sqrt{I}$ where I is the flux given by the simulation, multiplied by a *measurement time* t . For the high-intensity specular reflectivity at the lowest angle $t = 1 \text{ s}$ was chosen, the other values were adjusted to get comparable accuracy.

Furthermore, the simulations were used to estimate the instrument's performance (footprint size, beam homogeneity, brilliance transfer [\rightarrow tab. 2.1]) under ideal and under non-ideal conditions. This involves gravity effects [\rightarrow 6.4], and non-perfect alignment of the guides [\rightarrow 3.1].

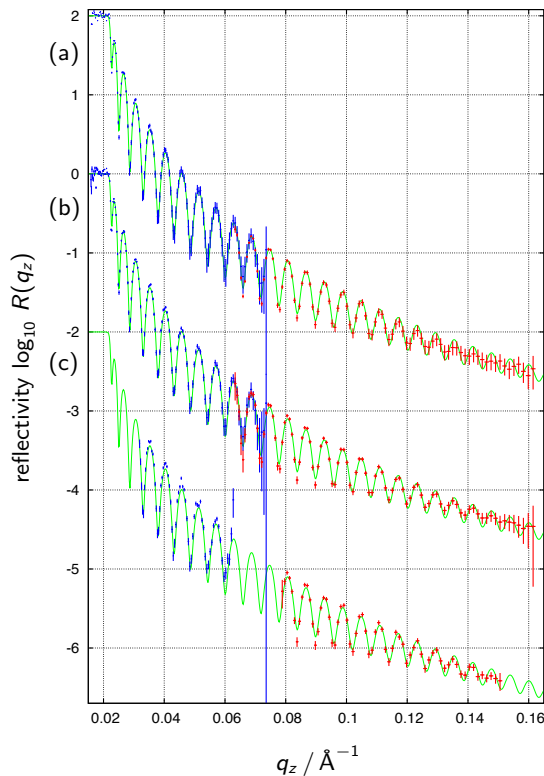


Figure 2.13: Reflectivities $R(q_z)$ extracted from the maps shown in figure 2.7 ($\omega = 2^\circ$, blue) and from the corresponding maps for a higher angle ($\omega = 4^\circ$, red).

The corresponding modes are:

(a) λ - θ -encoding with $\Delta\lambda/\lambda = 3.5\%$,

(b) high-intensity specular reflectivity,

(c) almost conventional set up with $\Delta\theta/\theta = 4\%$.

The curves are scaled by $10^2, 10^0, 10^{-2}$ for clarity. The green lines correspond to the initial reflectivity with $\Delta q/q = 2.4\%$. The covered q_z -range and the resolution functions depend on the measurement scheme. The *measurement times* t used to obtain the error bars are

mode	ω	t
(a)	2°	60 s
	4°	900 s
(b)	2°	1 s
	4°	10 s
(c)	2°	10 s
	4°	100 s

2.12 performance

The instrument's performance is governed by the design of the neutron guide. The truly focusing leads to a well-defined and clean beam, and to a low background. But it also leads to restrictions concerning maximum spot-size, or brilliance transfer. In the following these aspects are discussed in detail.

sample size The beam-spot will have a maximum width of 10 mm. The spot length is not restricted, but it influences the achievable resolution. The majority of the solid state samples studied today fit to these parameters. All wider samples (of high homogeneity) are not optimally exploited.

On the other side, the focusing allows to define the footprint far from the sample and thus no slit or other optical element is needed close to the sample. Bulky sample environment or high magnetic fields are no obstacle for precise beam definition.

q_z -range A maximum $q_z > 2 \text{ \AA}^{-1}$ can be reached with a detector angle of 120° . For reflectometry measurements this is too high (there are hardly any samples which allow for 1 \AA^{-1} , but it enables to measure crystal Bragg peaks of the substrate or the film (with $d > 3 \text{ \AA}$).

The most interesting region $q_z \in [0.005, 0.5] \text{ \AA}^{-1}$ can be covered with 4 orientations of the sample.

resolution The intrinsic instrument resolution is below 5%, which fits for 90% of the experiments. Since the full pulse is already used, a lower resolution will not result in shorter counting times or better statistics. Only if $\Delta q/q < 5\%$ is required one has to trade intensity for resolution.

Simulations showed that at least $\Delta q/q = 2\%$ is accessible without using a chopper (but one fast moving slit).

For very small q_z the detector resolution will dominate and set a limit.

background It is impossible to calculate the actual background, and thus the dynamic range. During the design process of the instrument and the measurement schemes, care was taken to reduce the background as much as possible.

One big advantage of the *Selene* guide system is that it transports much less neutrons compared to other guides. This and the focusing to the sample leads to a lower background and to a reduced illumination of the sample environment. Each *Selene* guide section avoids direct line of sight twice, i.e. already after half the

guide length the ESS criteria are matched. Thus most probably, Εστία will have a much lower fast neutron background than all other instruments.

In addition, the time-intervals of the proton pulse are not used for data acquisition, neither in the monitor nor in the detector.

polarisation There are various state-of-the-art technologies for spin-polarisation and spin-analysis compatible with the design of Εστία.

High magnetic fields at the sample position are possible. There is free space with a radius of more than 2 m available without any optical or mechanical component. Polariser and analyser can be located 12 m, and 6 m from the sample, so that an interaction with the sample field can be avoided.

counting time The counting time is limited by the brilliance transfer of the guide system, and by the fraction of the neutron pulse used for measurements. The *Selene* guide system has in general a lower transmittance than ballistic guides. On Εστία a further decrease of the beam intensity is taken into account because of using two *Selene* sections to reduce the fast neutron background.

These losses are compensated by the fact that all operation modes of Εστία make use of the full neutron pulse length without stitching. There are no losses due to choppers, or the avoidance of measurement frames overlapping in time.

flexibility The truly focused beam converging to the sample position gives new options of measurement schemes. The usage of a slit to cut down the divergence gives full compatibility with existing TOF reflectometers concerning data collection and reduction. Scanning this slit during a pulse extends the q_z -range accessible in one shot, and it results in a nicer q_x - q_z -area for off-specular measurements. By addition of a multilayer monochromator it is possible to realise almost any resolution $\Delta q/q = \text{const}$. And finally, by not using any slit behind the guide, one can decrease the counting time by at least one order of magnitude for split-second time resolved measurements.

The convergent beam can also be manipulated by reflecting on hyperbolic or parabolic surfaces to form a beam focused to the detector, or to obtain a parallel beam, respectively. These options will, for example, enable GISANS or GID measurements.

2.13 design options

The instrument design and its properties as presented above are obtained by following the ESS baseline parameters for the moderator size and emission characteristics, the available space (and restricted area), and radiation issues (e.g. to be out of line of sight twice). It was also attempted to meet the requests and suggestions given by the STAP, e.g. not to measure during the prompt pulse.

If some of these constraints vary, or if the science case changes (larger samples, very high resolution, ...), it is possible to adapt the instrument concept.

small moderator The recently discussed *pan-cake* moderator with a higher brilliance can be easily used by skipping the pin-hole in the extraction unit and using the moderator itself as a focal point. The brilliance gain can be entirely used to reduce the measurement time. The only price one has to pay is an increased shielding of the first guide section.

shorter wavelengths If a gap in the TOF-data due to the prompt pulse time can be accepted (in the conventional mode), it is possible to reduce the instrument length, and thus to increase the wavelength band and lower λ_{min} . This would result in a wider q_z -range and a higher intensity. In the high-intensity mode and when using the fast moving slit for λ - θ -encoding a gap in q_z can be avoided.

sample size Larger samples are accessible with a changed shape of the ellipses - on the cost of divergence or intensity.

vertical scattering plane The guide as presented does not give a preference for horizontal or vertical scattering geometry as the beam at the sample position is convergent with the same divergence in both directions. A slightly modified sample stage and a vertically movable detector enable a vertical scattering geometry. For liquid surfaces the beam still has to be reflected downwards (or upwards).

short instrument By using a feeder section, followed by only one *Selene* guide section for a much shorter instrument would increase the brilliance transfer considerably. But beam manipulation would have to be performed within the shielding.

3 Technical Maturity

3.1 guide system

The biggest challenge of the presented instrument is the long-term stability of the *Selene* guide alignment. It is relatively straight forward to set up and align the individual components, as long as one has full access. Once buried under concrete and activated, this is no longer the case for the 1st guide section.

A misalignment of the 1st guide section as a whole can be accepted if the pin-hole in the extraction unit is large enough to act as a virtual source also for the tilted or shifted guide. The misalignment of individual components is easy to trace, but not so easy to correct. A solution would be to put all components on actuators. But this would result in ≈ 150 degrees of freedom — which is essentially a costing problem. The realignment with these actuators is possible by using light optics or interferometry and an adapted computer algorithm. Tests to align the prototype elements with an interferometer were performed successfully at the SLS metrology lab.

P. Böni, SwissNeutronics, suggested to mount all individual mirror elements of one guide segment (7.2 m long) on a rigid support (steel or granite beam). He claims that no realignment would be needed within this unit later on. The 4 guide segments then have to be adjustable with regard to the source and pin-hole, and relative to each other. This results in 24 degrees of freedom in total (position and orientation of each segment).

A comparison with the accuracy and stability required for the elements of the ESS linear accelerator, or at a synchrotron beam line tells that the technology to keep the *Selene* guide aligned is available.

guide accuracy The angular accuracy needed for the guide alignment can be estimated by looking at the longest free flight path before the sample. This is the trajectory from the entrance of the last guide segment to the sample. A beam off-set of 0.1 mm at the sample position corresponds to an angular error of $0.1 \text{ mm}/9600 \text{ mm} \approx 10^{-5} \text{ rad}$. The waviness of a state-of-the-art float glass guide is of the order $5 \cdot 10^{-5} \text{ rad}$. A yz-position accuracy better than 0.1 mm can be achieved, so that this can be neglected compared to the influence of waviness.

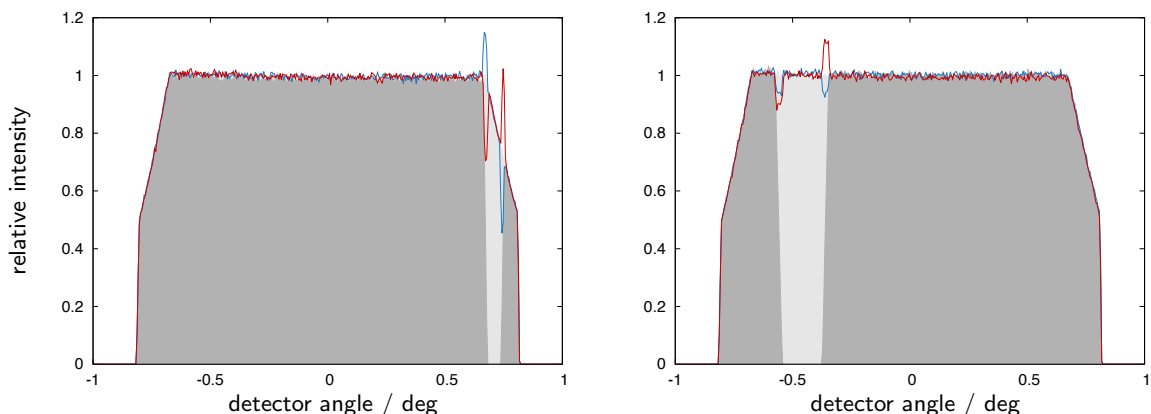


Figure 3.1: Intensity distribution on the detector in y direction of a beam reflected off a perfect sample of $10 \times 10 \text{ mm}^2$. The total shaded area corresponds to the perfectly aligned guide. The light gray shaded areas correspond to intensity losses when the second (left), and the next-to-last 500 mm long building block (right) of the last segment of the guide were removed, respectively. The solid lines correspond to shifting each building block by 0.1 mm (red), and by rotating it by 0.001° (blue), respectively.

Figure 3.1 shows the intensity distribution on the detector in y direction for a beam reflected off an ideal sample of $10 \times 10 \text{ mm}^2$ for various guide building blocks being misaligned. This tells that a position error of 0.1 mm has about the same effect as a rotational misalignment of 0.001° ($\approx 2 \cdot 10^{-5} \text{ rad}$). The latter corresponds to the waviness of a brilliant state-of-the-art neutron guide. This means that the limiting factor is rather the waviness than the guide alignment. From the simulations it can be deduced that the main features of a misaligned guide are due to the discontinuities at the ends of the building blocks. This means that a misaligned, but continuous guide surface should perform better than individually misaligned parts. This has to be investigated further.

monitoring The geometry of the *Selene* guide allows for a relative simple monitoring of the guide alignment. A point-like white light source (e.g. a LED) at the initial focal point of one segment should ideally produce a homogeneous rectangular image on a screen behind the final focal point. Any deviation of the guide surface from the exact elliptic profile leads to a redistribution of the intensity on the screen. Since there is a unique relation of any point on the screen to a certain beam trajectory, it is possible to trace a intensity drop back to the part of the guide which is misaligned.

By coupling in/out the light by optical mirrors (e.g. Si wafers), this monitoring set-up can be installed permanently, allowing for fast feedback.

The open questions are to find a radiation-resistant actuator, and to develop (or adapt) the feedback system.

3.2 optical components, polarisation

A prototype of a frame-overlap-filter / polariser working in transmission [$\rightarrow 7.1$] was successfully tested in 5. 2013 at PSI. The double bounce monochromator was already successfully tested [$\rightarrow 11.2.4$].

Spin analysers using supermirror technology to cover a wide angular range or a large window are operational, e.g. at FOCUS, PSI, or at HYSPEC, SNS.

3.3 mechanics, sample stage

The mechanical support system for the sample and sample environment, and the analog support for the virtual source are standard components. The same is true for slow slit systems, and for stages to exchange optics or insert a CCD camera.

A challenge is the support system for the 2nd *Selene* guide section. This is some 20 m long, but it has to be adjusted with respect to the virtual source with an accuracy in the sub-mm-range and an angular error well below 0.1° . Since it is expected that the heavy shielding leads to a drop of the monolith area with time, it is necessary that the guide can be realigned as a whole, without too much effort.

3.4 fast slit system

For all operation modes a slit behind the last guide segment is needed. For the almost conventional mode it defines the beam divergence and the angle of incidence, for all modes it helps aligning the sample. Such a slit is a standard component.

If one wants to switch the slit position and opening in between pulses, it must be able to change the blade positions by up to 60 mm within 10 ms. If this high speed (20 km s^{-1}) can not be reached, one loses one or several pulses during repositioning and thus time-resolved measurements might suffer.

When used to scan the beam during one pulse, both blades must move independently and very accurately over $\approx 60 \text{ mm}$ within 60 ms and reset within 10 ms. This would allow to cut down unwanted scattering from the monochromator in the λ - θ -encoding mode. If such a device is possible to realise is not clear. It was discussed with T. Gahl, ESS, but there is no clear conclusion yet and further clarification is needed.¹

¹For comparison: \circ State-of-the-art CNC laser-cutter machines allow for positioning speeds of 20 mm/10 ms with heavy loads over large distances with 4 degrees of freedom. The position accuracy is 10 μm . \circ Industry robots sorting pralines non-stop (4 axis, $\approx 1 \text{ m}$ distance) realise up to 4 pics per second.

3.5 detector

The detector technology available nowadays can be used in principle, so that even when new detector concepts fail, the operation of the instrument is guaranteed. The limitations of present day detectors are the resolution, the size and the accepted count rate.

In section 9.2 a wish-list of the detector properties is given together with the motivations.²

Besides the additional costs for a new detector, there are no principle obstacles to later replace the *day one* detector for a better one.

3.6 computing, data analysis

The raw data will have a format of the type $I(t, y, z)$ (or the single event analog). Simple perl scripts to normalise, integrate and re-bin the data are written for the analysis of the prototype measurements. This means that the algorithms for data analysis are available.

The situation changes when one wants to conserve all information contained in the raw data for fitting. The re-binning and integration (especially in the high-intensity mode) leads to a reduction and mixing of resolution. To overcome this, one can compare measured and simulated intensity maps, rather than curves. The challenge is then to modify the output of a simulation program (eventually supported by reference measurements), and to implement a good fitting algorithm. The fitting *by eye* is no longer possible.

² This wish-list was sent to R. Hall Wilton, ESS, beginning of 2013. No feedback has been received yet, also considering that several reminders were sent.

4 Costing

The costs given below for some selected components of the instrument are based on requests to the manufacturer, on price lists and on feedback by the ESS. They display the situation beginning to mid 2013. These are **only non-personell costs**.

4.1 insert in the extraction unit and instrument shielding

The measures and materials used for this estimate are based on input by P. Bentley, ESS, 10. 04. 2013.

The insert within the target monolith is assumed to consist of copper. Its measures are: $0.2 \times 0.2 \times 4.0 \text{ m}^3 = 0.16 \text{ m}^3 \hat{=} 1.4 \text{ t}$ (the free space for the beam can be neglected here).

The masks at 18.6 m and at 26 m and between monolith and common shielding are assumed to use 1 m^3 copper, each. This corresponds to 27 t.

Assuming a copper price (04. 2013) of $6 \text{ k€}/\text{t}$ this gives 170 k€.

The instrument shielding (without the common shielding) from $x = 15 \text{ m}$ to $x = 25.8 \text{ m}$ is assumed to have a heavy concrete core with a cross section of $2 \times 2 \text{ m}^2$ (with the guide in the centre), and an outer shell of light concrete with a cross section of $5 \times 5 \text{ m}^2$. This corresponds to 44 m^3 of heavy concrete, and 226 m^3 of light concrete. A recent (01. 2013) offer to PSI for 200 m^3 light concrete and 50 m^3 heavy concrete summed up to 2000 k€ (without form factor or reinforcement).

The common shielding up to $x = 15 \text{ m}$ is not taken into account.

insert and instrument shielding	2 200 k€
---------------------------------	----------

4.2 guide

SwissNeutronics made an offer for the *Selene* neutron guide and the support system on January 2013.

The offer covers the neutron guide on glass or aluminium, the alignment frames, granite beams as a base and an aluminium housing to contain the vacuum. This does not exactly match the requirements by the ESS, since shielding issues most likely will not allow for the offered wide and straight vacuum housing and the alignment system with frames. But it still gives an idea of the actual costs to be expected. For the guides the offer covers the curved substrates with a $m = 2.5 \text{ Ni/Ti}$ coating. In detail, there are 4 guide sections of 7.2 m, each, consisting of 15 elements, made up of 2 truly curved mirrors.

double- <i>Selene</i> guide system	550 k€
------------------------------------	--------

4.3 guide support

The support consists of 4 granite beams on kinematic mounts, the alignment frames, the vacuum housing, and vacuum windows. No shielding is included. Mounting is due to the customer.

guide support	520 k€
---------------	--------

4.4 mechanics (sample stage and the like)

Based on offers by Huber, ADC and Franke, P. Keller, PSI, estimated the costs for the standard components for the sample stage, the beam-definition stage and other similar devices to be ≈ 180 k€. This does not take into account that at the sample stage non-magnetic components will be needed. For the motion of the second *Selene* guide section and for the detector stage a solution with air-pads and a friction wheel was assumed. Together with the special floor this costs ≈ 150 ke. The fast moving slit is not included.

motion mechanics	330 k€
------------------	--------

4.5 motion control

For the *standard* components (i.e. without fast aperture [\rightarrow 3.4]) an approximate price per freedom of 4 k€ is assumed, including motor controller, encoder, motor, and cabling (discussed with T. Gahl, ESS, 18. 03. 2013). This leads to

motion control	150 k€
----------------	--------

4.6 detector

We did not get any feedback from the ESS detector group concerning costs of a detector system.

A fission chamber monitor costs ≈ 10 k€.

A CCD camera with scintillator and housing for instrument and sample alignment (based on a similar system purchased for BOA at PSI) costs ≈ 60 k€.

detectors	? k€
-----------	------

4.7 filter / polariser

Based on the costs of a prototype of the bent frame-overlap and polarisation filter, a similar but longer device will cost some 25 k€.

The price for one RF flipper (electronics, coils, magnets and housing) is approximately 30 k€ (private communication with P. Hautle, PSI).

In addition, a guide field of some 24 m length has to be realised.

The wide-angle analyser based on SM-coated, bent substrates for the instrument FOCUS at PSI cost some 500 k€ (U. Filges, PSI).

polarisation equipment	600 k€
------------------------	--------

total costs

Summing up the positions mentioned above and rounding generously, Εστία will cost some 5 million €, without taking manpower for design, construction, and installation into account.

total costs w/o manpower	5 m€
--------------------------	------

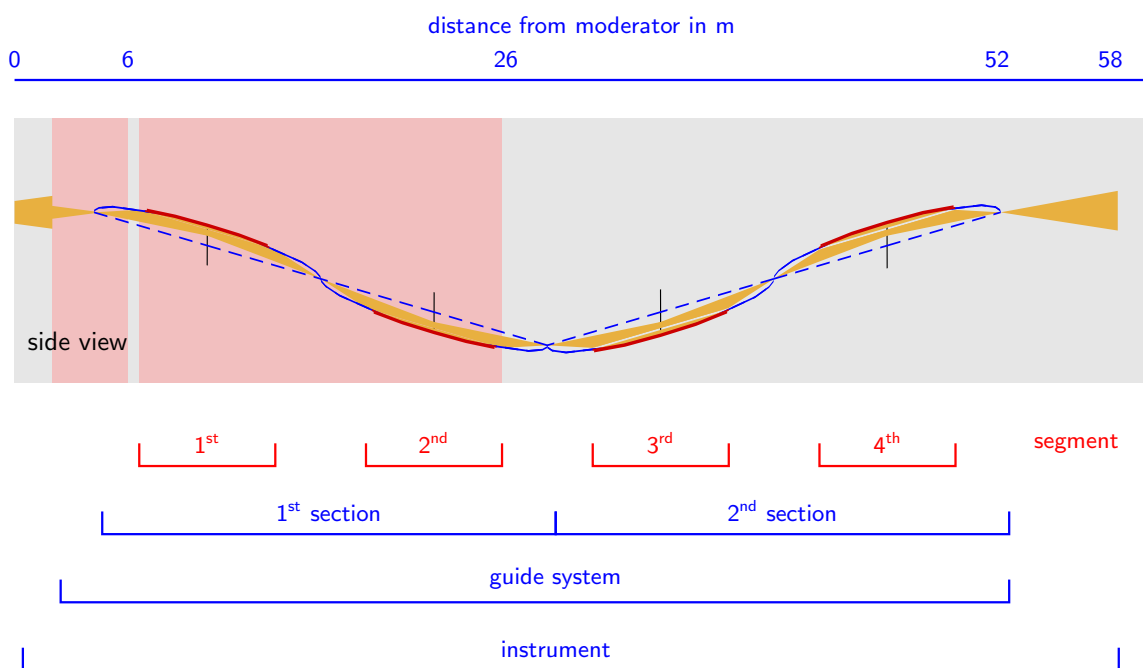


Figure 5.1: Nomenclature used in this script to address the various items and measures of the double *Selene* guide. The sketch is taken from figure 2.1. The **guide segments** are the elliptically curved and SM coated guides. The distance between the initial and final focal point of one *Selene* guide is called **section**. Here, two sections and the extraction unit make up the **guide system**, ending at the sample position.

6 the Selene guide system

We chose two subsequent elliptically shaped reflectors to focus the beam to the sample. The reason is that this set-up allows for:

- independent definition of the divergence $\Delta\theta$, and of the beam spot size at the sample;
- a three-dimensional definition of the footprint;
- convenient beam manipulation;
- early reduction of the phase space, i.e. low background and radiation in the sample and detector region.

At the same time all trajectories have the same length. In the following sections several aspects of the *Selene* guide system are presented.

history The idea for the *Selene* guide is based on concepts by F. Ott to use a focused beam with a wide divergence in combination with λ - θ -encoding, obtained by a graded monochromator of half-elliptic shape.[22, 23] First experiments with a graded multilayer coating [35] revealed conceptual problems and led to the approach to use a flat multilayer monochromator for λ - θ -encoding, followed by the elliptic reflector. And attempts to correct for coma aberration finally led to the *Selene* guide geometry with two subsequent elliptic reflectors. This way, neutron guide and encoding are decoupled. This means that encoding is optional and might be also achieved by other approaches like the *rainbow* concept by R. Cubitt.[32, 33]

Though developed for a reflectometer, the *Selene* guide concept can in principle also be used for other instruments. The limiting factors are the transported divergence, the minimum wavelength, and the sample size.

optimisation strategy The design and a large part of the optimisation of the *Selene* guide system was performed analytically. This is possible because of the rather straight-forward and clear mathematical description of the possible beam trajectories. As a consequence one can relate almost all geometrical parameters of the guide system, the coating and the transmission. The rather large number of parameters collapses this way to essentially three which can be chosen freely. All the rest is then determined. In the following sections these relations are derived and discussed.

Figure 6.1 illustrates the approach chosen here for the design of the instrument, starting with an estimate for the desired divergences and wavelength-range at the sample position. The second set of input parameters are the given source brightness $I_0(\lambda)$ and a reasonable length of the guide, described by the ratio of the actual guide segment length to the focal point distance, ξ . As figure of merit the measurement time t is used. The physical parameters of the guide (b/a and ϵ) are deduced from the starting parameters and they determine the coating (m), reflectivity (R) and thus the transmission T of the guide. Together with the divergence and $I_0(\lambda)$ this determines the counting time.

The *optimisation problem* can be illustrated at the example of $\Delta\theta$, which enters the counting time quadratically (for high-intensity specular reflectivity), but which also affects m linearly. Since high m leads to a lower transmission T with a more complicated dependence, one has to iteratively find the best $\Delta\theta$.

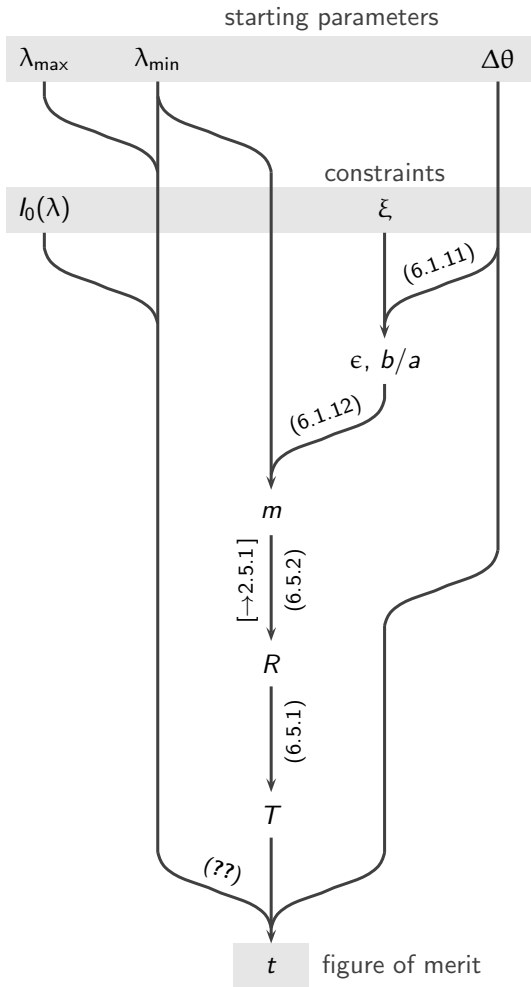


Figure 6.1: Flow diagram used to estimate the counting time t as a figure of merit from chosen (λ -range, $\Delta\theta$) and given ($I_0(\lambda)$, ξ) starting parameters.

The meaning of the other symbols is: $\epsilon, b/a$ orientation and shape of the ellipses, m coating of guides, R reflectivity of the guide, and T transmission of the guide system.

The diagram is simplified since it is based on the ideal assumption of a point-like sample, perfect guides and coatings, and some external constraints such as the exclusion of the prompt time for data collection [→8.3] are not taken into account.

6.1 geometrical considerations for an elliptic reflector

The geometry of the elliptic guides (i.e. the ratio of the half axes b/a), their length and coating should be defined starting by the requirements at the sample position. The limitations are the maximum curvature of the guide, the available coating, $I_0(\lambda)$, and the space available.

The following formulae can be used to estimate the optimum geometry of a *Selene*-type guide for given parameters like expected divergence $\Delta\theta$, and wavelength-range $\lambda_{\min} \dots \lambda_{\max}$.

These formulae are based on the small-angle approximation $\tan \alpha \approx \alpha$, $\tan \beta \approx \beta$, and a strong asymmetry of the ellipse $a \gg b \Rightarrow c \approx a$. Furthermore, the distance from the initial focal point to the guide entrance is assumed to be the same as the distance from its exit to the second focal point.

ellipse relation:

$$\frac{x^2}{a^2} + \frac{y^2}{b^2} = 1 \quad (6.1.1)$$

$$y = \pm \frac{b}{a} \sqrt{a^2 - x^2} \quad (6.1.2)$$

$$c = \sqrt{a^2 - b^2} \quad \text{half distance between focal points} \quad (6.1.3)$$

minimum acceptance angle (relative to long axis):

$$\begin{aligned}
 \alpha &\approx \frac{b \sqrt{a^2 - (\xi a)^2}}{a (\xi + 1)a} \\
 &\approx \frac{b}{a} \sqrt{\frac{(1 - \xi)(1 + \xi)}{(1 + \xi)^2}} \\
 &\approx \frac{b}{a} \sqrt{\frac{1 - \xi}{1 + \xi}} \\
 &\approx \frac{b}{a} \frac{1 - \xi}{\sqrt{1 - \xi^2}}
 \end{aligned} \tag{6.1.4}$$

maximum acceptance angle (relative to long axis):

$$\begin{aligned}
 \beta &\approx \frac{b \sqrt{a^2 - (\xi a)^2}}{a (\xi - 1)a} \\
 &\approx \frac{b}{a} \sqrt{\frac{(1 - \xi)(1 + \xi)}{(1 - \xi)^2}} \\
 &\approx \frac{b}{a} \sqrt{\frac{1 + \xi}{1 - \xi}} \\
 &\approx \frac{b}{a} \frac{1 + \xi}{\sqrt{1 - \xi^2}}
 \end{aligned} \tag{6.1.5}$$

accepted / delivered divergence:

$$\begin{aligned}
 \Delta\theta &= \beta - \alpha \\
 &\approx \frac{b}{a} \left(\frac{1 + \xi}{\sqrt{1 - \xi^2}} - \frac{1 - \xi}{\sqrt{1 - \xi^2}} \right) \\
 &\approx \frac{b}{a} \frac{2\xi}{\sqrt{1 - \xi^2}}
 \end{aligned} \tag{6.1.6}$$

inclination of the center of the beam relative to the long half axis:

$$\begin{aligned}
 \epsilon &= \frac{1}{2}(\alpha + \beta) \\
 &\approx \frac{1}{2} \frac{b}{a} \left(\frac{1 + \xi}{\sqrt{1 - \xi^2}} + \frac{1 - \xi}{\sqrt{1 - \xi^2}} \right) \\
 &\approx \frac{1}{2} \frac{b}{a} \frac{2}{\sqrt{1 - \xi^2}} \\
 &= \frac{\Delta\theta}{2\xi}
 \end{aligned} \tag{6.1.7}$$

minimum coating of the guide surface:

$$\begin{aligned}
 m &= \frac{4\pi \frac{\alpha + \beta}{2}}{\lambda_{\min} q_{Ni}^c} \quad \text{with (6.1.7):} \\
 &= \frac{4\pi \epsilon}{\lambda_{\min} q_{Ni}^c}
 \end{aligned} \tag{6.1.9}$$

Starting with input parameters λ_{\min} and $\Delta\theta$ required at the sample, and with given ξ , it is possible to deduce all other parameters:

$$\frac{b}{a} \approx \frac{\Delta\theta}{2} \sqrt{\frac{1}{\xi^2} - 1} \tag{6.1.10}$$

$$\epsilon \approx \frac{\Delta\theta}{2\xi} \quad \begin{array}{l} \text{inclination of the guide, and} \\ \text{maximum angle of incidence on the guide} \end{array} \tag{6.1.11}$$

$$m = \frac{4\pi \epsilon}{\lambda_{\min} q_{Ni}^c} \quad \begin{array}{l} \text{for a finite source, the angular error has to be} \\ \text{taken into account to calculate the } \textit{real} \ m \end{array} \tag{6.1.12}$$

and

$$\alpha \approx \epsilon \cdot (1 - \xi) \quad (6.1.13)$$

$$\beta \approx \epsilon \cdot (1 + \xi) \quad (6.1.14)$$

For $\xi = 0.6$ one gets the following approximations:

$$\begin{aligned} \frac{b}{a} &\approx \frac{2}{3} \Delta\theta \\ &\approx 0.012 \Delta\theta / \text{deg} \end{aligned}$$

$$\epsilon \approx 0.8 \Delta\theta$$

$$m \approx 8 \frac{\Delta\theta / \text{deg}}{\lambda_{\min} / \text{\AA}}$$

For $\Delta\theta \approx 2\epsilon$ the pre-assumptions are no longer fulfilled! A reasonable upper limit for ξ is about 80%.

Figure 6.2 shows the iso-lines for constant m and for constant $\Delta\theta$ on a map of b/a vs. ξ , obtained for $\lambda = 4 \text{ \AA}$. E.g. if a divergence of $\Delta\theta > 3^\circ$ is required, but the coating is limited to $m = 6$, the possible values for b/a and the relative length ξ are within the (light gray) area below the blue iso-line for $m = 6$ and above the red iso-line for $\Delta\theta = 3^\circ$. So the smallest ξ is ≈ 0.62 with the strong curvature $b/a \approx 0.033$. Relaxing the latter value leads to a longer guide and allows for a coating with lower m .

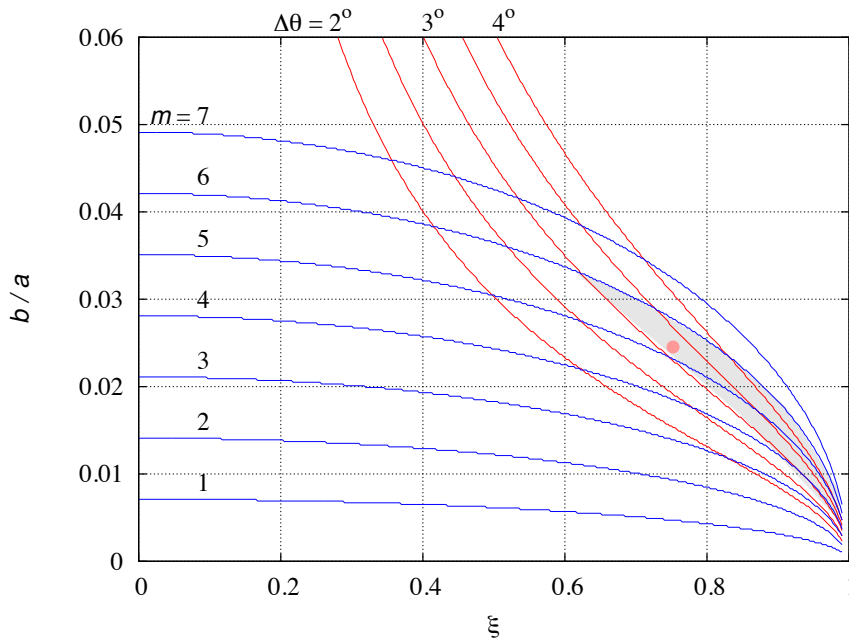


Figure 6.2: Iso-line for constant m (blue) and for constant divergence $\Delta\theta$ (red) for $\lambda = 4 \text{ \AA}$ as a function of the effective length of the guide ξ and the ratio of the half axes parameters b/a .

Reducing the wavelength e.g. from 4 \AA to 2 \AA does not affect the red iso-line, but the blue ones are scaled down by 0.5 along b/a . There is no intersection left (for reasonable guide lengths) with the $\Delta\theta = 3^\circ$ criterion, so that there is no guide geometry possible fulfilling the requirements.

For $\Delta\theta = 3^\circ$ and $\lambda = 4 \text{ \AA}$ a reasonable choice would be $b/a \approx 0.025$ and $\xi = 0.75$ (marked by a red dot). The coating then should be $m \approx 5.5$. (These are for the sake of example and are not the parameters chosen for Εστία.)

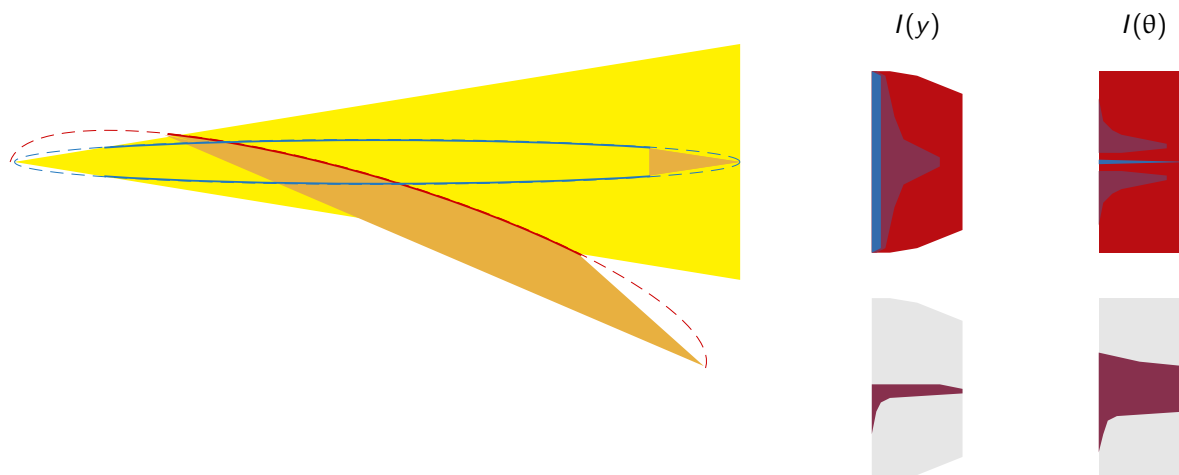


Figure 6.3: Sketch to illustrate the difference between a full elliptic guide (blue) and a *Selene* guide (red). Both are designed to deliver a beam of a certain divergence to the sample (gold). The beam emitted by the source (yellow) of a certain divergence is accepted by both guides. The elliptic guide generates $I(y)$ and $I(\theta)$ distributions containing contributions with no (blue area), one (dark red) and multiple reflections (red). Due to the strong coma of the full ellipse (large ξ , small b/a) the single-reflected beam is quite broad in $I(y)$, and it shows a bi-modal distribution in $I(\theta)$ caused by the guide not closing about the source. The complete beam overilluminates the sample position and it provides a wide divergence, while the divergence at the sample position is considerably narrower (defined by the distance and width of the guide end). In contrast, the *Selene* guide delivers only neutrons reflected exactly one time, with the wanted divergence and a sharp beam spot. (The one-reflector set up shown here still suffers from coma aberration which leads to the visible tails in the $I(y)$ and $I(\theta)$ distributions.)

6.2 angular acceptance

We are often confronted with the remark that a full ellipse could transport twice the divergence of half an elliptic guide. The point is that the divergence should be defined by the needs on the sample, or it is given by geometrical limitations. In this case one has to ask for the most efficient way to transport this divergence. And if this can be realised with one branch of an ellipse, there is no need to accept the disadvantages of the full ellipse. Figure 6.3 illustrates this.

6.3 coma aberration — and correction

Elliptic reflectors show coma aberration. This means two things: radiation emitted from (close to) the first focal point into a solid angle Ω and reflected before the mid of the ellipse reaches the second focal point under a smaller solid angle. Radiation emitted in Ω but reflected behind the mid of the ellipse results in a large solid angle. Consequently, the focusing / de-focusing property of the reflector varies along its length.

At the same time the position of the image of an off-axis pre-image point depends on the position where along the reflector the beam is reflected. For an early reflection the distance of the image from the long axis increases, for a late reflection it decreases.

In total the phase space density is conserved, but the distribution of intensity vs. angle and beam-height $I(\theta, z)$ is distorted. An identical second collinear reflector, sharing one focal point with the first one, shows the same aberration, but since early reflection in the first reflector leads to a late reflection in the second one, the distortion is almost cancelled.

This is illustrated in figure 6.4. The maps show $I(\theta, z)$ as accepted by the elliptic reflector (left), the corresponding intermediate image with the distorted shape (middle) and the almost restored shape at the image (source) position. The deviations still visible originate from the final length of the second reflectometer, and from the quite large pre-image chosen to emphasize the effect of coma aberration.

For small angles, i.e. small b/a and $\xi < 0.8$ one can deduce a simplified mapping algorithm. A trajectory connecting the first focal point, a point on the ellipse at (x', z') , and the second focal point intersects the

long axis at angles α_1 and α_2 . These are given by

$$\begin{aligned}\alpha_1 &\approx \tan \alpha_1 \\ &\approx z'/(c - x') \quad \text{and} \\ \alpha_2 &\approx z'/(c + x')\end{aligned}$$

Using eqn. 6.1.2 and $c \approx a$ one gets

$$\begin{aligned}z' &= \frac{b}{a} \sqrt{c^2 - x'^2} \\ \alpha_1 \alpha_2 &= \frac{z'^2}{(c - x')(c + x')} \\ &= \left(\frac{b}{a}\right)^2 \frac{c^2 - x'^2}{c^2 - x'^2} \\ &= \left(\frac{b}{a}\right)^2\end{aligned}$$

If the trajectory intersects the first focal plane with a (small) offset z_1 this leads to an angular error $\Delta\alpha \approx z_1/(c - x')$. Since the beam is specularly reflected, α_2 changes by the same $\Delta\alpha$. The resulting offset at the

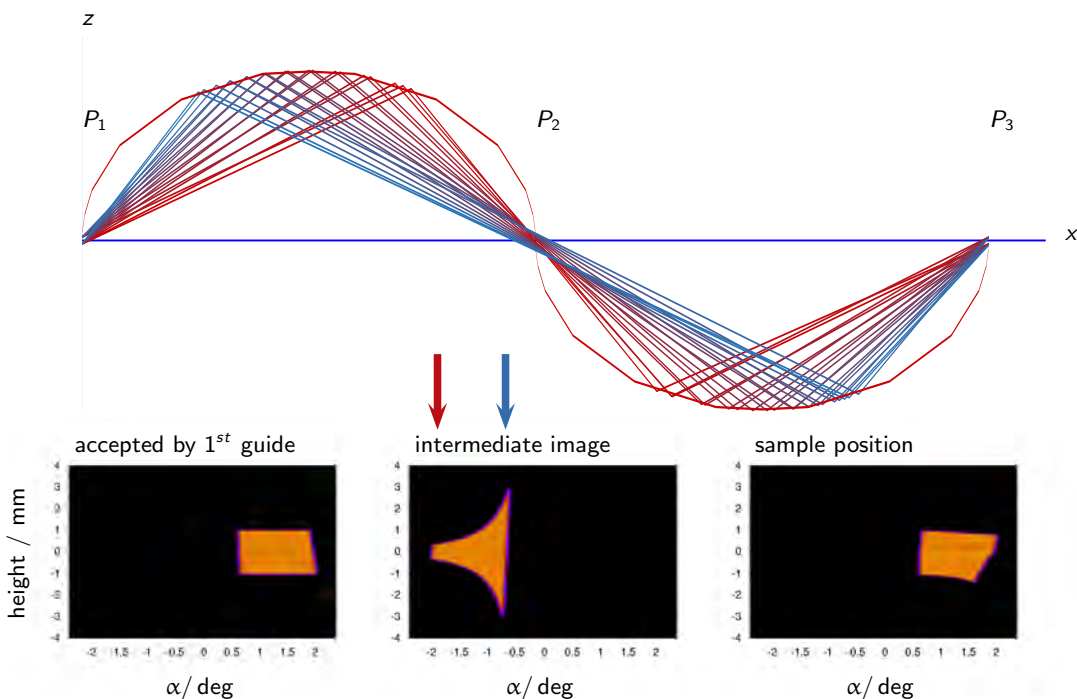


Figure 6.4: Sketch to illustrate the effect of coma aberration. The pre-image consists of 2 point-sources, located at $z = \pm 1$ mm. The half-axis parameters used here are $a = 2000$ mm, $b = 50$ mm, the sketch is stretched by 30 normal to the long axis. The take-off angle α is encoded in the colour of the beam. At the intermediate position a clear separation of the colours can be seen. High α results in an almost parallel wide beam, while low α results in a beam focused to the second focal point. Behind the second ellipse, the initial image is almost restored. The $I(\alpha, z)$ maps illustrate the shape of the phase space as accepted by the ellipse and defined by a 2 mm slit at P_1 (left), at the intermediate position P_2 (middle), and finally after correction at P_3 (right). The arrows atop the middle map denote for which α the beam is compressed (red) or expanded (green).

second focal plane is

$$\begin{aligned}
 z_2 &\approx (c + x') \Delta\alpha \\
 &\approx \frac{c + x'}{c - x'} z_1 \\
 &\approx \frac{\alpha_1}{\alpha_2} z_1 \\
 &\approx \frac{(b/a)^2}{\alpha_2^2} z_1
 \end{aligned}$$

The second elliptic reflector transforms z_2 into

$$\begin{aligned}
 z_3 &\approx \frac{(b/a)^2}{\alpha_3^2} z_2 \\
 &\approx \frac{(b/a)^2}{\alpha_3^2} \frac{(b/a)^2}{\alpha_2^2} z_1 \\
 &\quad \text{with } \alpha_2 \alpha_3 = (b/a)^2 \\
 &\approx z_1
 \end{aligned}$$

This means that reflection on a range $\{x\}$ rather than a point x' results in a line at the second focal plane, but again in a point at the third focal plane. The coma¹ aberration is corrected for.

There are several limitations for this approach:

source height The source height is limited by the requirement that no garland reflections should occur. The *first* garland case one reaches by making z larger is the one when the trajectory connects $(-c, z(-c))$, the entrance of the guide $(-\xi c, z(-\xi c))$, the exit of the guide $(\xi c, z(\xi c))$, and a point on the second focal point. The symmetry of the problem tells, that the trajectory is parallel to the long axis between the two points on the ellipse. The inclination of the guide at the entrance is $\beta - \epsilon$. Thus the inclination of the incoming trajectory is twice this value:

$$\begin{aligned}
 z_1 &= \beta(1 - \xi)c - 2(\beta - \epsilon)(1 - \xi)c \\
 &= (2\epsilon - \beta)(1 - \xi)c \\
 &= (2\epsilon - (1 + \xi)\epsilon)(1 - \xi)c \\
 &= \epsilon(1 - \xi)^2 c
 \end{aligned}$$

For the Εστία parameters this means $z_1 < 21$ mm! To the other side of the long axis, away from the reflector, there is no such restriction. The *missing* lower right edge of the phase space volume at the sample position of figure 6.4 illustrates this effect.

higher angles Exact calculation of the trajectories not using the small angle approximation show that the aberration is not completely compensated for. This can be seen in the slight bending of the phase space volume in figure 6.4.

finite reflector length Trajectories with a large offset at the intermediate focal point might miss the entrance or the exit (i.e. they are not reflected) of the second guide. These are lost. As a consequence the image at the final focal point gets blurred on one side (the other side is limited by the acceptance of the first reflector). This sets a limit for the source size in the other direction.

making use of coma aberration It is not always useful to correct for coma aberration: If e.g. a small beam is required, one can reach this by using the beam reflected at the end of the reflector. For the present case, its height is only 30% of the initial slit. On the other side one can get a wide beam of low divergence by using only the beginning of the reflector. This is what at synchrotron sources is achieved with a Kirkpatrick-Baez optics (which consists of two elliptically shaped reflectors, one for each transverse direction).

¹ *coma* (lat.) means *tail* and refers to the shape of the image of a not-centered point source or, more generally, a finite source

6.4 chromatic aberration due to gravity

P. Korelis, E. Rantsiou

While the focusing properties of reflecting optics are achromatic (besides the λ dependent reflectivity) for straight trajectories, there are chromatic effects induced by gravity. Its influence on the spot size and divergence is not immediately apparent because there are amplifying and compensating aspects for reflections on an elliptic guide. For example, if one assumes the first reflection pointing downwards, gravity leads to a longer free flight path before the neutron hits the reflector. But it will hit it at a smaller angle.

The drop of the neutrons due to gravity is given by

$$\begin{aligned}\Delta z &= -\frac{1}{2} g t^2 \\ g &\approx 9.81 \text{ m/s}^2 \\ t &\approx 2.52 \cdot 10^{-4} \text{ s m}^{-1} \text{ \AA}^{-1} x \lambda \\ \Rightarrow \frac{\Delta z}{m} &\approx 3.07 \cdot 10^{-7} \left(\frac{x}{m} \frac{\lambda}{\text{\AA}} \right)^2\end{aligned}$$

So Δz scales with distance and wavelength squared.

Δz	$x = 2400 \text{ mm}$	9600 mm	19200 mm
$\lambda = 5.0 \text{ \AA}$	-0.04 mm	-0.7 mm	-2.8 mm
9.4 \AA	-0.16 mm	-2.5 mm	-10 mm

The main question to be answered then is whether or not gravity sets limitations to the focusing performance of a *Selene* guide at the sample position. To elucidate the effect of gravity, virtual studies using the McStas simulation software package have been performed.

The model instrument is comprised of a single *Selene* guide with the first element reflecting downwards and the second reflecting upwards as shown in figure 6.5. The geometrical parameters are the same for the horizontal (xy plane) and vertical (xz plane) elliptic reflectors: $b/a = 0.0228$, $\xi = 0.5$, and length of the focusing section $4c = 40 \text{ m}$. The resulting angular acceptance is $\Delta\theta = 1.5^\circ$.

To single out the effect of gravity and to better illustrate that, certain simplifications have been added to the model. Regarding reflector performance, the reflectors are constructed from ideal supermirrors, disregarding changes in supermirror reflectivity as a function of momentum transfer and effects such as absorption. A virtual source is used, with a uniform wavelength distribution extending from 2 to 10 \AA , and it is located at the entrance focal point of the *Selene* guide. The size of the source is $1 \times 1 \text{ mm}^2$ and its divergence is adjusted to compensate for the crooked neutron trajectories that might result in some of the long-wavelength neutrons missing the far end of the reflector. As a result, the entirety of the reflecting surface of the first *Selene* element is illuminated by neutrons of all wavelengths.

Figure 6.6 shows the intensity maps at the intermediate focal point P_2 , simulated with and without including gravity (bottom and top row, respectively). To single out with which trajectory certain features in the intensity maps are related, the first and second half of the first guide element were interchangeably switched to be vertically absorbing. The horizontal reflection element was fully reflecting in all cases.

The coma aberration, inherent to the elliptical shape of the reflectors, is evident in the intensity maps in the top row. Reflecting on the first half of the vertical elliptical reflector (left image) contributes a broad beam profile at P_2 . In an inverse manner, reflecting on the second half of the vertical elliptical reflector (right image) results in a highly focused beam profile. As expected, the centre image in the top row, generated by reflecting on the complete first element, shows no difference in the intensity profile between the vertical and horizontal direction.

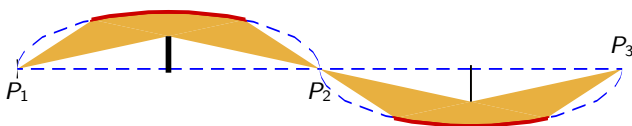


Figure 6.5: Sketch of the setup used for simulations including gravity. The guide parameters are $c = 10000 \text{ mm}$, $b/a = 0.0228$ and $\xi = 0.5$. The initial slit has a height of 1 mm and is centred at the focal point.

Gravity is included in the simulations shown in the bottom row. While no change in focusing is observed in the horizontal direction, a tail becomes visible in the vertical direction. Gravity does little to improve the focusing of neutrons reflected on the first half of the vertical elliptical reflector. The vertical tail is also shown to originate almost exclusively from reflections on the first half of the reflector. Reflections on the second half of the vertical elliptical reflector (bottom right image), are found to result in some smearing out of the bright focused spot, along the positive direction of the vertical axis. It was further clarified, through simulations using a single wavelength, that the vertical position of the focusing spot at P_2 shifts upwards, scaling with neutron wavelength. On one hand, the height of the focusing position for longer wavelengths is shifted upwards, and on the other hand, the long-wavelength neutrons are also more heavily influenced by gravity on their way to the second *Selene* element.

The intensity maps of the beam spot at the exit focal point P_3 are shown in figure 6.7, simulated with and without gravity. In the graph to the right, the intensity is integrated along the horizontal direction and the distribution of intensity as a function of the vertical position is shown for selected wavelengths.

Comparing the intensity maps, the beam profile appears to be close to fully restored. It becomes apparent that a compensating mechanism exists for the effect of gravity for small λ , once the neutrons have travelled through and interacted with the full length of the *Selene* guide. The integrated intensity as a function of vertical position indicates that for small wavelengths, e.g., 3 Å, the effect of gravity is negligible. For wavelengths near the upper end of the range that is expected at ESS for a *Selene* type reflectometer, there is an observable change, manifested by a vertical shift of the centre of the focused spot by approximately 0.3 mm, broadening at the base by nearly the same amount and a corresponding reduction in the intensity of the maximum plateau by about 15%.

The $I_\lambda(z)$ graph illustrates that there is only a weak chromatic aberration up to at least 6 Å and a moderate effect at 9 Å. Above that the picture changes, the intensity for $\lambda = 15$ Å, for example, is distributed over 4.5 mm with a bimodal distribution. Obviously there is an upper limit for $x^2 \lambda^2$, up to which the *Selene* guide has low chromatic aberration due to gravity.

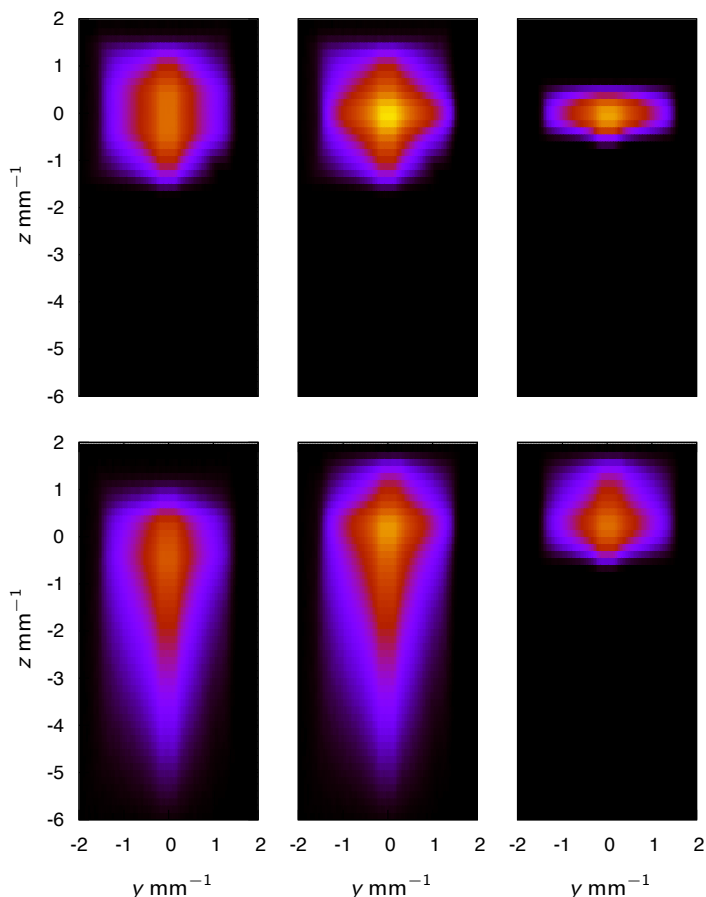


Figure 6.6: Intensity maps $\log_{10}[I(y, z)]$ at the intermediate focal point P_2 of a *Selene* guide system with a total length of 40 m. The upper row was simulated without gravity, the lower one with gravity. For the left/right column only the first/second half of the vertically reflecting guide element was actually reflecting. The middle column was obtained with reflection along the full guide element. The incident slit was $1 \times 1 \text{ mm}^2$, the wavelength-range was $\lambda \in [2, 10] \text{ \AA}$.

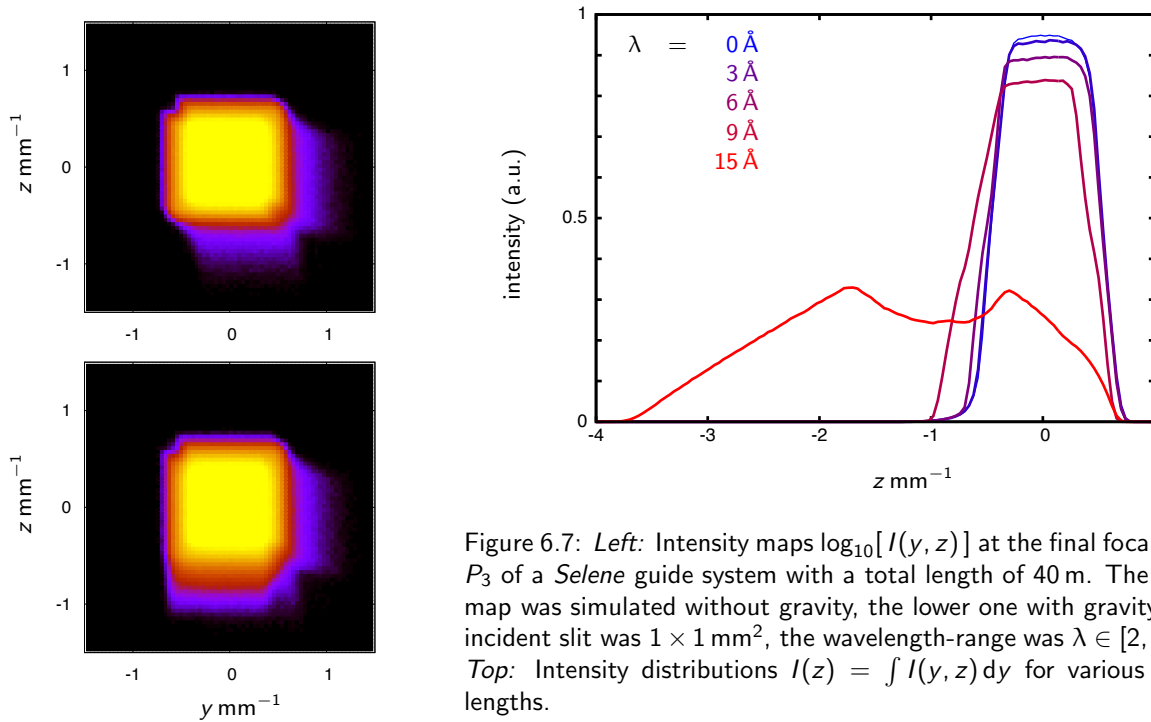


Figure 6.7: *Left*: Intensity maps $\log_{10}[I(y, z)]$ at the final focal point P_3 of a *Selene* guide system with a total length of 40 m. The upper map was simulated without gravity, the lower one with gravity. The incident slit was $1 \times 1 \text{ mm}^2$, the wavelength-range was $\lambda \in [2, 10] \text{ \AA}$. *Top*: Intensity distributions $I(z) = \int I(y, z) dy$ for various wavelengths.

In a further set of simulations the geometry shown in figure 6.5 was turned upside down, i.e. the first guide element reflecting downwards and the second upwards. The essential difference is, that for longer wavelengths the intensity is reduced (some 10% at $\lambda = 9 \text{ \AA}$), while the spot size is slightly smaller.

discussion Taking into account that the actual length of one *Selene* section will be 24 m instead of the 40 m used here, while keeping the λ -range, one can assume that the chromatic aberration plays in the sub-mm-range for the proposed reflectometer with two *Selene* sections. In addition, it affects only the spot size normal to the scattering plane.

chromatic aberration on Εστία Similar simulations as described above were performed for the lay-out and geometry of Εστία as given in table 2.2. Figure 6.8 shows the vertical intensity distribution $I(z)$ at the sample position.

Here gravity has three obvious effects: \circ It leads to a slight reduction of the transmission, caused by the fact that some neutrons do not reach a coma-correcting second guide segment due to gravity. \circ The intensity peak shifts upward by at most 1 mm. \circ And the profile gets sharper with increasing wavelength. The latter effect overcompensates the mentioned shift, so that the full beam still hits the sample.

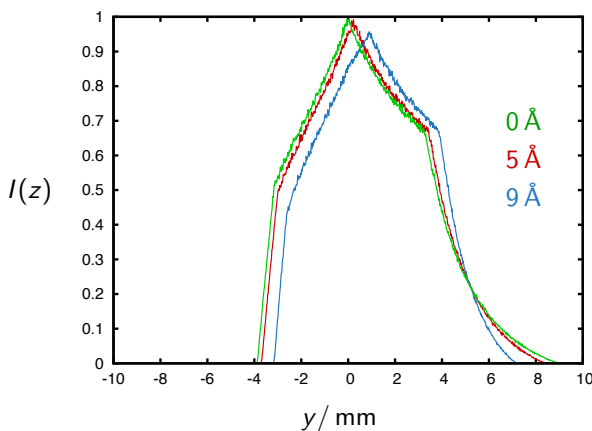


Figure 6.8: Simulated vertical intensity distribution $I(z)$ at the sample position (normal to the scattering plane). The green line was obtained without gravity, the red and blue lines correspond to 5 \AA and 9 \AA , respectively.

6.5 transmission

The effective flux at the sample can be estimated by reducing the initial flux $I_0(\lambda)$ by the losses due to reflections on the guide walls. The double *Selene* guide concept involves 8 reflections for all neutrons on surfaces with

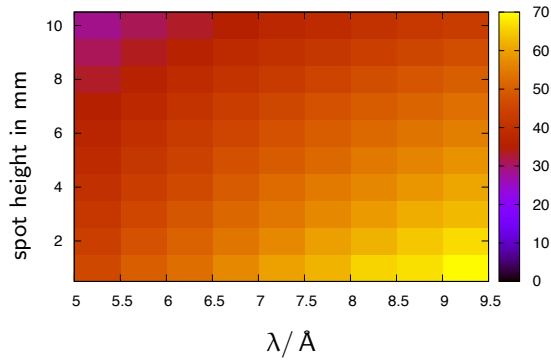


Figure 6.9: Brilliance transfer of Εστία obtained by McStas simulations for a divergence of $1.5^\circ \times 1.5^\circ$ and beam spot sizes reaching from $1 \times 10 \text{ mm}^2$ to $10 \times 10 \text{ mm}^2$.

a non-perfect reflectivity R (plus further reflections in the extraction unit). The angle of incidence on the guide surface hardly varies along the guide for the presented concept: $\theta \approx \epsilon = \Delta\theta/2\xi$. One can thus assume $R(q_z) = R(\lambda, m)$, with the optimised coating m [→6.1.12]. This leads to and an attenuation of

$$I(\lambda) = I_0(\lambda) \cdot \prod_{i=1}^n R(\lambda, m_i) \quad (6.5.1)$$

n is the number of reflections,. This pushes the flux maximum to higher λ . Based on typical reflectivities (by SwissNeutronics) the following linear relation was used for a fast estimate of the transmission:

$$R(\lambda, m) = \begin{cases} 1 & \text{for } \lambda > m \lambda_{\min} \\ 0 & \text{for } \lambda < \lambda_{\min} \\ \frac{13}{12} - \frac{1}{12} \frac{m \lambda_{\min}}{\lambda} & \text{else (i.e. 50\% reflectivity at } m = 7 \text{ and 100\% at } m = 1) \end{cases} \quad (6.5.2)$$

The resulting transmission for Εστία is shown in the graph in table 2.1.

More precise results were obtained by performing McStas simulations on the full guide (without gravity, assuming a perfect surface). The resulting brilliance transfer strongly depends on the beam spot size. In figure 6.9 the brilliance transfer as a function of wavelength and beam spot size is given.

6.6 divergence vs. peak-to-background ratio

A general problem with samples with inherent background (e.g. incoherent scattering by hydrogen) is the separation of specular intensity and background. The specular signal is obtained by integrating over some area A on the detector, given by the sample size $x \times y$, and the divergence of the beam $\Delta\theta_{xz} \times \Delta\theta_{yz}$.

$$A = (l \tan \Delta\theta_{xz} + x \tan \theta) \times (l \tan \Delta\theta_{yz} + y) \quad (6.6.1)$$

with the sample-detector distance l and the angle of incidence θ .

The specular signal is proportional to the number of scatterers (the sample size) and the divergence of the incoming beam.

$$I_{\text{sp}} \propto x y \Delta\theta_{xz} \Delta\theta_{yz} \quad (6.6.2)$$

and the background I_{bg} is proportional to $I_{\text{sp}} A$ if an isotropic distribution of the background scattering is assumed. Thus the dynamic range is at most $I_{\text{sp}}/I_{\text{bg}} = 1/A$. And the often used figure-of-merit $I_{\text{sp}}^2/I_{\text{bg}} = I_{\text{sp}}/A$.

For the measures of Εστία, i.e. $l = 6200 \text{ mm}$ the dominant contributions to the spot size A is the divergence.² This leads to

$$\frac{I_{\text{sp}}}{I_{\text{bg}}} \propto \frac{1}{\Delta\theta_{xz} \Delta\theta_{yz}} \quad (6.6.3)$$

²For $\Delta\theta_{yz} = 1.5^\circ$ the spot-width is 160 mm, compared to at most $y = 50 \text{ mm}$ added by the sample.

Thus the background is affected by the divergence in both directions alike! The wide in-plane divergence used in conventional reflectometry measurements to increase the signal has the same influence as a wide divergence in the scattering plane. The figure-of-merit in this case is

$$\frac{I_{sp}^2}{I_{bg}} \propto x y \quad (6.6.4)$$

scales only with the sample size. This is obviously non sensical here. Thus I_{sp}^2/I_{bg} is not a good choice for reflectometry measurements.

consequences for the high-intensity specular reflectivity Since the expected background scales approximately with the divergence in the scattering plane $\Delta\theta_{xz}$, the high-intensity mode of Εστία is strongly affected. It does not really help to reduce $\Delta\theta_{yz}$ because then the sample-width becomes a limiting factor.³ Thus if the sample has a high intrinsic background and a high dynamic range has to be investigated, this mode will not work.

focusing to the detector The size of the beam-spot can be dramatically reduced by focusing to the detector in the sample plane. The spot-width is then only dependent on the focusing property of the optics and might reach below the detector resolution. The beam divergence in the sample plane is then limited to $\Delta\theta_{yz} = \arctan y/l$, which reduces also I_{sp} .

On Εστία it is possible to use a hyperbolic mirror before the sample position to focus to the detector in the sample plane. The incoming intensity is then just reduced by the finite reflectivity of the mirror. Provided the sample is wide enough to accept the re-focused beam, there is almost no loss in I_{sp} . But I_{bg} is reduced by up to 2 orders of magnitude.⁴

This opens the possibility to still use the high-intensity mode or to increase I_{sp}/I_{bg} in normal operation for problematic samples.⁵

³One must keep in mind that y in general is at least an order of magnitude larger than the effective sample height $x \tan \theta$.

⁴This assumes that there is no background coming from the hyperbolic mirror!

⁵Yet this is an idea and no simulations have been performed.

7 Optics and Beam Shaping

7.1 frame-overlap and polarisation filter

An optical element used for polarising a beam or for frame-overlap suppression (i.e. used as a low-pass for λ) should ideally intersect the beam at the same optimised angle γ everywhere within the beam. For a parallel beam this is fulfilled by a flat surface, inclined relative to the beam by γ . For a beam emerging from a point the corresponding surface has the shape of a logarithmic spiral

$$\begin{aligned} x &= a e^{bt} \cos t \\ y &= a e^{bt} \sin t \end{aligned}$$

with $b = 1/\tan \gamma$, and the scaling factor a .

For a small γ and a rather low divergence $\Delta\alpha \ll 10^\circ$ the spiral can be approximated by a function $f(x)$. A beam trajectory passing through the origin has the function

$$y_\alpha(x) = x \tan \alpha \tag{7.1.1}$$

It intersects $f(x)$ at the point where $f(x) = y_\alpha(x)$. At this point the slope of $f(x)$ has to be $\tan(\alpha + \gamma)$, where $\tan \alpha$ is the slope of the trajectory. Thus

$$\begin{aligned} \tan \alpha &= \frac{f(x)}{x} \\ f'(x) &= \tan(\alpha + \gamma) \\ &= \frac{\tan \alpha + \tan \gamma}{1 - \tan \alpha \tan \gamma} \\ &= \frac{f(x)/x + \tan \gamma}{1 - f(x)/x \tan \gamma} \end{aligned} \tag{7.1.2}$$

$$\approx \frac{f(x)}{x} + \gamma \quad \text{for small } \gamma \text{ and } \alpha \tag{7.1.3}$$

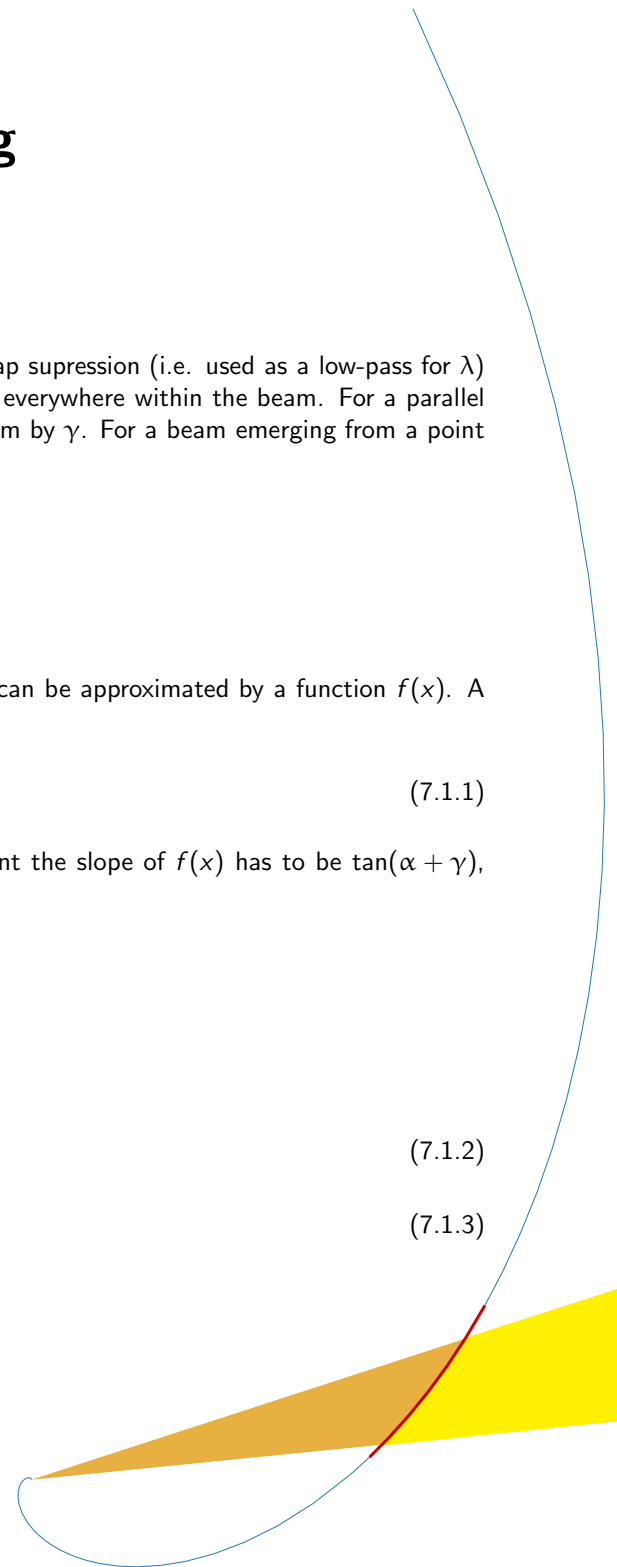
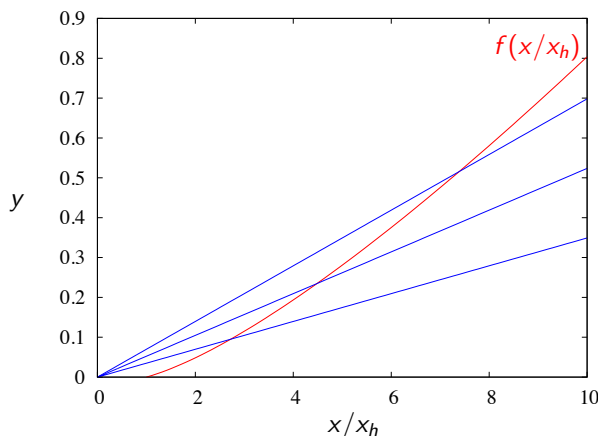


Figure 7.1: Sketch of the geometry of a surface $f(x)$ which is hit by all trajectories $y = x \tan \alpha (\forall \alpha)$ at the same angle γ . Here $\gamma = 2^\circ$ and $\alpha = 2^\circ, 3^\circ, 4^\circ$ are displayed.

It is assumed here that all angles are small. The solution for the simplified differential equation (7.1.3) is

$$f(x) = \gamma x \ln \left[\frac{x}{x_h} \right] \quad (7.1.4)$$

where x_h is a scaling factor given by the intersection of $f(x)$ with the horizon $f(x_h) = 0$.

Since the problem is centrosymmetric, one can rotate f around the origin (which is the same as changing x_h).

The intersecting point is obtained by

$$\begin{aligned} \gamma x \ln \left[\frac{x}{x_h} \right] &= x \tan \alpha \\ \gamma \ln \left[\frac{x}{x_h} \right] &\approx \alpha \\ x(\alpha) &= x_h \exp \left[\frac{\alpha}{\gamma} \right] \end{aligned}$$

A possible application is the *simultaneous* use of such a device as frame overlap filter and polariser. For the **low-pass** for λ the ideal coating is Ni with $R = 1$ for $q < q_{Ni}$. The (idealised) cut-off angle is then given by

$$\sin \gamma = q_{Ni} \frac{\lambda_{max}}{4\pi}$$

Below the Ni coating a polarising SM can be deposited with

$$m = 4\pi \frac{\sin \gamma}{\lambda_{min} q_{Ni}} = \frac{\lambda_{max}}{\lambda_{min}}$$

For the present parameters $\lambda \in [5, 9.4] \text{ \AA}$ one gets $\gamma \approx 1^\circ$, and $m_{SC} < 2$. Assuming $\Delta\theta = 1.5^\circ$ and a minimum distance of the device from the point-source of 300 mm, the total length is $300 \text{ mm} \cdot \exp[1.5^\circ/1^\circ] \approx 1400 \text{ mm}$. These numbers are obtained for a point source. For a finite source they increase.

prototype A polariser based on the principle mentioned above was designed and build for the test-*Selene* set-up at PSI. The rather short distances and the relatively large virtual source with a height of 1 mm resulted in a split assembly.

The device was designed at the Laboratory for Neutron Scattering, PSI, and manufactured by SwissNeutronics.

The technical parameters are $\lambda \in [4, 16] \text{ \AA}$, and $x \in [170, 395] \text{ mm}$, with x the distance from the focal point. The upper limit is given by the entrance of the prototype *Selene* guide at $x = 400 \text{ mm}$. The divergence to be covered is $\Delta\theta = 1.8^\circ$. The polarising coating is a $m = 4.2 \text{ FeCoV} / \text{Ti:N}$ supermirror, covered with Ni to simultaneously act as a low-pass for $\lambda < 16.8 \text{ \AA}$.

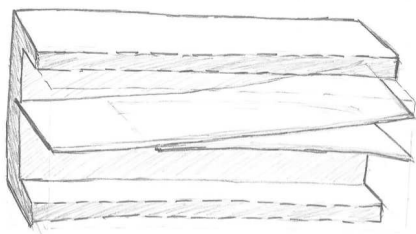


Figure 7.2: Left: First sketch for a frame-overlap filter and polariser for the *Selene* prototype set-up, based on transmission/reflection through/at spiral-curved surfaces. Right: Final device, produced by SwissNeutronics. The glass tube is 215 mm long and has an inner height and width of $50 \times 50 \text{ mm}^2$. The virtual source is to be 170 mm before the entrance (to the left).

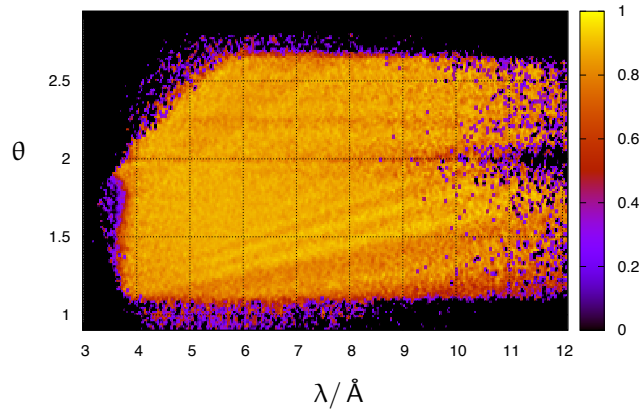


Figure 7.3: Measured polarisation efficiency of the beam filtered by the transmission polariser, transmitted through the *Selene* guide, and analysed by a remanent FeCoV/Ti:N supermirror on glass ($10 \times 10 \text{ mm}^2$, $m = 3$). The magnetisation of the analyser was performed with a permanent magnet by hand, i.e. not under optimal conditions. No spin-flipper was available for this test. The brighter diagonal lines in the map reveal imperfections in the analyser (= sample) coating. The cut-off at $\lambda \approx 4 \text{ \AA}$, $\theta \approx 2.5^\circ$ corresponds to the critical edge of the analyser coating. Imperfections of the polariser should result in horizontal lines, so they can not be distinguished from imperfections of the guide. This map tells that the polariser has an efficiency of at least 90% over an angular range of 1.6° for a source opening of 1 mm.

7.2 condenser

A convergent beam can be transformed into a parallel beam by deflection on the outside of a parabolically shaped surface, where the foci coincide. In analogy with light optics this device is called *condenser*, here.

The function for a parabola with the focal point at $(0,0)$, a horizontal axis, and the opening to negative x is

$$y = \sqrt{p^2 - 2px} \tag{7.2.1}$$

p defines the curvature of the parabola, $p/2$ is the distance of the apex from the focal point. The incoming neutron trajectories (pointing to the focal point) are

$$y = x \tan \alpha \tag{7.2.2}$$

with $-90^\circ < \alpha < 0^\circ$. Both functions intersect at

$$\begin{aligned} \sqrt{p^2 - 2px} &= x \tan \alpha \\ x^2 \tan^2 \alpha + 2px - p^2 &= 0 \\ x &= \frac{-2p \pm \sqrt{4p^2 + 4p^2 \tan^2 \alpha}}{2 \tan^2 \alpha} \\ &= \frac{p}{\tan^2 \alpha} (-1 \pm \sqrt{1 + \tan^2 \alpha}) \\ &= \frac{p}{\tan^2 \alpha} \left(-1 - \frac{1}{\cos \alpha} \right) \end{aligned} \tag{7.2.3}$$

$$y = \frac{p}{\tan \alpha} \left(-1 - \frac{1}{\cos \alpha} \right) \tag{7.2.4}$$

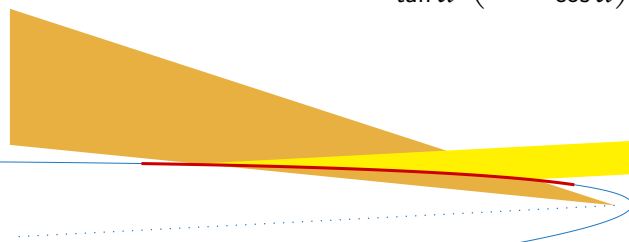


Figure 7.4: Sketch to illustrate the path of rays for a condenser-like optics based on a parabolically bent, reflecting surface. The incoming convergent beam (gold) is deflected on the surface (red) and forms a parallel beam (yellow).

It was used that only intersections before the focal point ($x < 0$) are of interest. For a given distance x and angle α the parameter p can be obtained from eqn. 7.2.3:

$$p = \frac{x \tan^2 \alpha}{-1 - 1/\cos \alpha} \quad (7.2.5)$$

The direction of the parallelised beam is given by the parabola axis. The width can be tuned by changing p and thus the distance from the focal point where the deflection occurs.

divergence The divergence of the beam behind the condenser depends on the spot size at the focal position, and on the degree of compression. The latter is a result of Liouville's theorem which states $\Delta y \times \Delta \theta = \text{constant}$.

example To make a convergent beam with $\Delta \theta = 1.5^\circ$ parallel with a beam width of 26 mm, the deflector extends from $x = -2000$ mm to $x = -500$ mm, and it has a shape defined by $p = 0.686$. The angle of incidence on the deflector varies from 0.75° to 1.50° . This corresponds to a SM coating of $m = 3$ for $\lambda \geq 5 \text{ \AA}$.

GISANS Such a condenser can be used for GISANS measurements, where a low-divergent beam is needed.

To make the beam parallel in both directions, two subsequent devices (analogue to a Kirkpatrick-Baez mirror), or a nested device (Montel Optics) can be used. The first approach allows to use individually tunable surfaces (adaptive optics) so that beam width and divergence can be adjusted.

7.3 zoom

A beam convergent to one pole of a hyperbola can be reflected on the outside of the hyperbola and focused to its other pole. The reflector thus changes the focal length and acts like a zoom.

This could be used to focus the beam on the detector rather than on the sample position to perform focusing GISANS.

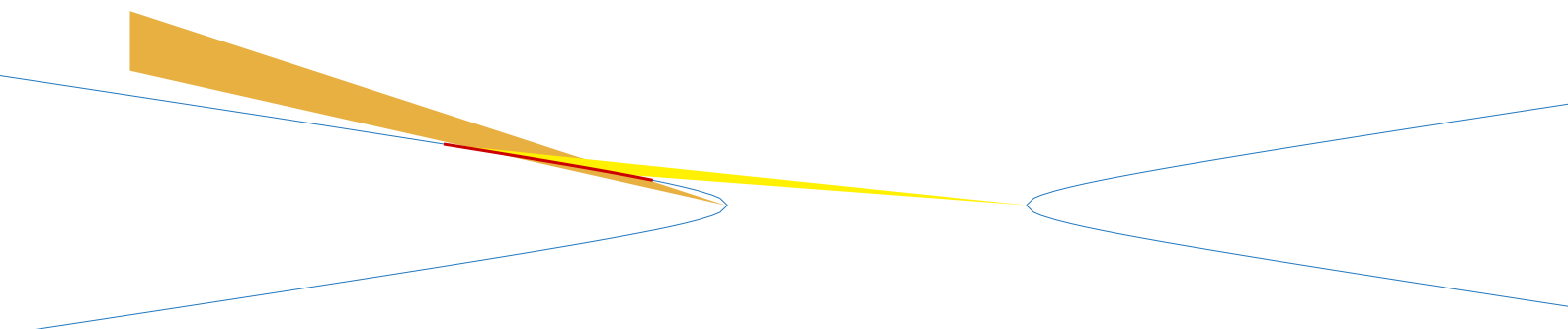


Figure 7.5: Sketch to illustrate the path of rays reflected on the surface of a hyperbolically shaped surface (blue line). The hyperbola has one pole at the focal point of the incoming beam (gold). The beam is redirected to the second pole (yellow).

As for the condenser, the direction of the reflected beam can be varied by tilting the hyperbola main axis. The spot-size and the shape of the parabola determine the resolution.

There is an infinite set of parameters a and b defining a hyperbola

$$\frac{x}{a} - \frac{y}{b} = 1$$

with a distance between the poles of

$$2e = 2\sqrt{a^2 + b^2}$$

so that with adaptive optics it will be possible to tune the beam size for the sample.

8 Boundary Conditions and Consequences

Based on information distributed at IKON3, and on private communications with P. Bentley, K. Anderson, and H. Wacklin, 11.2012, there are the following boundary conditions to be expected for a *short* reflectometer. Short means of the order of 50 m long or less, i.e. situated in one of the inner guide halls at the ESS.

8.1 space

- The first 2 m around the moderator are free of any elements.
- Within the target monolith shielding (2 to 6 m) an insert of 210 mm width (but at most forming a 5° wedge) and of 210 mm height can be freely shaped. Optical elements are allowed in the insert. Since there will be a cooled He atmosphere (from moderator up to the end of the monolith) also free-standing Si-wavers can be used.

The last 500 mm of the monolith might be occupied by a shutter (which can host optical elements).

- Behind the monolith there might be a chopper or other moving parts.
- From the monolith up to a radius of 15 m a common shielding for all instruments will be built. The beam guide can be of any shape and size. There is the option to insert choppers and other devices (most likely accessible from the top).
- At a distance larger than 15 m to the moderator, the individual instrument guide shielding starts. Its length depends on the dose rate caused mainly by fast neutrons (also by secondary processes).
- The *short* instruments will have a 10° wedge-shaped space available. This is necessary to allow for sufficient shielding to prevent cross-talk of background.
- The height differences from moderator to floor are 3 m and 2 m. The hall allowing for high magnetic fields will have the 2 m distance. If needed it is possible to get a lower floor locally.

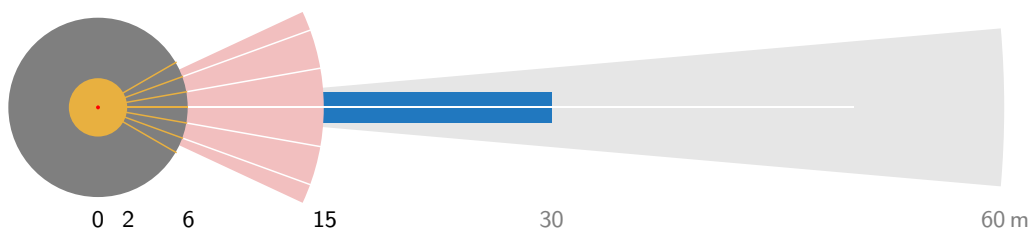


Figure 8.1: Sketch to illustrate the various shielding jackets intended for the source and the instrument. The colours mean: red—moderator, yellow—He-atmosphere, gray—target-shielding, light red—common instrument shielding, blue—individual guide-shielding (as far as possible), light gray—10° wedge available for a short instrument.

8.2 shielding and background

- The target monolith (for the moment) is intended to consist of steel.
- The common instrument shielding will be made of various materials to moderate fast neutrons, convert muons and neutrons, and absorb γ and neutrons.
- The effective direct line of sight from any point of the instrument area to the moderator and target is to be avoided. This means at least 12 m material in the direct line.
At most half of the length of the guide (shielding) is to have direct line of sight.
- Indirect line of sight has to be avoided, i.e. from outside the shielding no area directly illuminated by the source (moderator and target) is visible. Here the thickness of the shielding material is about 2 m.

8.3 exclusion of proton prompt

At ISIS second target station and at the SNS the fast neutrons and hard x-rays produced during the proton pulses (or by secondary processes in the shielding) cause problems in the data acquisition. The corresponding STAP members R. Dalgliesh and J. Ankner suggest not to collect data during these times. So it is favourable to tune the instrument length and λ -range in a way to exclude the pulse times without creating holes in the q -range.

For the time being all reflectometers should be developed in a way that the time interval of high fast neutron background is excluded from the measurements.

Following the argumentation of section 2.5.1 the usable wavelength-range for reflectometry starts at about 4 Å to 5 Å for *Selene* guides. An instrument length of some 60 m results in a wavelength-range of e.g. $\lambda \in [5, 10]$ Å. For the ESS baseline parameters this has the consequence that the background burst from the proton pulse appears at the beginning or the end of the used wavelength-range. Further optimisation leads to the situation that the bursts are just outside the required λ -range, as is sketched in figure 8.2.

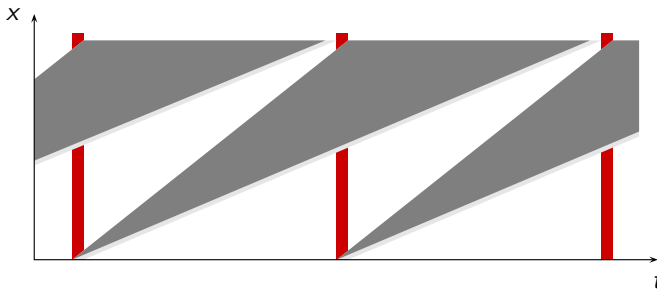


Figure 8.2: Sketch to illustrate how to avoid the influence of the γ and fast neutron burst from the proton pulse hitting the target. The sketch is to scale with period $T = 70$ ms, pulse length $t = 3$ ms, and a sample detector distance of 58 m, i.e. $\lambda \in [5, 9.3]$ Å.

For this scheme, the flight times for the shortest / longest wavelength are $t = 73$ ms / 137 ms (assuming a burst time of 3 ms and a period of 70 ms). For $\lambda_{\min} = 5.00$ Å this leads¹ to an instrument length of $\overline{SD} = 58'400$ mm, and this in turn to $\lambda_{\max} = 9.38$ Å.

8.3.1 intrinsic resolution

The intrinsic λ resolution for this instrument is given by the length of the flight path X , and the pulse length τ via

$$\begin{aligned} \frac{\Delta\lambda}{\lambda} &= \frac{\Delta t}{t} \\ \Delta\lambda &= \frac{\tau}{\frac{m}{h} X \lambda} \lambda \\ &= 3956 \cdot 10^{-7} \text{ m}^2 \text{ s}^{-1} \frac{\tau}{X} \\ &\approx 0.2 \text{ \AA} \quad \text{for } X = 58.4 \text{ m}, \tau = 2.85 \text{ ms} \end{aligned}$$

¹ From $E = \frac{mv^2}{2} = \frac{h^2}{2m\lambda^2}$ and $v = \frac{x}{t}$ (with distance x , time t , and neutron mass $m = 1.6745 \cdot 10^{-27}$ kg) follows
 $x = \frac{h}{m} \frac{t}{\lambda} \approx 3.956 \cdot 10^{-7} \frac{\text{m}^2}{\text{s}} \frac{t}{\lambda}$.

This leads to

$$\frac{\Delta\lambda}{\lambda} = 4.0\% \dots 2.1\% \quad \text{for } \lambda = 5 \text{ \AA} \dots 9.4 \text{ \AA}.$$

9 Technical Details

9.1 moving elements

This section gives a preliminary list of translation and rotation stages, sorted by location and purpose. All motion devices besides the guide positioning and alignment are also listed in table 9.1 with estimated ranges, accuracy, and load.

	motion	range	accuracy	load
apertures within ellipses	y translation	0 – 80 mm	< 1 mm	20 kg
	z translation	0 – 80 mm	< 1 mm	20 kg
	y translation	0 – 80 mm	< 0.1 mm	2.0 kg
	z translation	0 – 80 mm	< 0.1 mm	2.0 kg
beam definition	x translation	0... 40 mm	< 0.1 mm	2 kg
	z translation	±20 mm	< 0.1 mm	5 kg
	tilt	±5°	< 0.01°	10 kg
	roll	±5°	< 0.01°	15 kg
	x translation	±20 mm	< 0.01 mm	20 kg
	y translation	±20 mm	< 0.01 mm	25 kg
	ω	0°... 360°	< 0.002°	30 kg
	2 θ	±2°	< 0.01°	1)
	x translation	±100 mm	< 0.1 mm	0.5 t
	y translation	±100 mm	< 0.1 mm	0.5 t
fast aperture	y^+ translation	0... 80 mm	< 0.01 mm	1.0 kg
	y^- translation	0... 80 mm	< 0.01 mm	1.0 kg
	z^+ translation	0... 80 mm	< 0.1 mm	1.0 kg
	z^- translation	0... 80 mm	< 0.1 mm	1.0 kg
sample stage	z translation	±20 mm	< 0.1 mm	0.6 t
	tilt	±5°	< 0.01°	0.7 t
	roll	±5°	< 0.01°	0.7 t
	x translation	±20 mm	< 0.01 mm	0.8 t
	y translation	±20 mm	< 0.01 mm	0.8 t
	ω	0°... 360°	< 0.002°	1.0 t
	2 θ	-5°... 140°	< 0.01°	2)
	x translation	±500 mm	< 0.1 mm	1.5 t
	y translation	±500 mm	< 0.1 mm	1.5 t
CCD camera	z translation	0... 400 mm	< 0.01 mm	10 kg 3)

Table 9.1: Parameters for motion control, sorted by locations and purpose., For beam manipulation and sample stage a classical set-up using rotation and translation stages was assumed. 1) rotation of the full second guide section; 2) rotation of the detector arm; 3) accuracy only for the end-position.

9.2 detector characteristics

According to Richard Hall-Wilton, ESS, it is realistic to expect the following parameters:

resolution:	$0.5 \times 0.5 \text{ mm}^2$	minimum
size:	$500 \times 500 \text{ mm}^2$	maximum

As consequence the highest resolution at $q = 0.01 \text{ \AA}^{-1}$ with a sample-detector distance of 6.2 m, limited by the detector is

$$\begin{aligned}\Delta\theta &= \arctan[0.5/6200] \\ &\approx 0.005^\circ \\ \theta &= 0.43^\circ \quad \text{for } \lambda_{\max} = 9.4 \text{ \AA} \\ \Delta\theta/\theta &= 1.1\%\end{aligned}$$

position Since the length of the flight path is optimised to avoid the proton pulse time it is not advisable to change the sample-detector distance. So it could be mounted on a 2θ arm of fixed length, with a evacuated, frustum-shaped nozzle pointing towards the sample.

size A width of 500 mm results in an angle-range of 4.6° . This is three times the maximum divergence of the beam incident on the sample. The excess area in the scattering plane is needed for off-specular measurements. When using λ - θ -encoding, the specular beam scans over the inner 1.5° , so that effectively only another $\pm 1.5^\circ$ are available.

Normal to the scattering plane the maximum area of interest is only 170 mm wide. So the expected minimum detector size is

$$\begin{aligned}\text{width } y &= 500 \text{ mm} \\ \text{height } z &= 170 \text{ mm}\end{aligned}$$

resolution In the scattering direction (i.e. horizontally) a high resolution is required. Ideal would be a pixel-size of 0.5 mm or less. The lower limit is given by the effective sample size of a fraction of a mm.

Normal to the scattering plane (vertical) a much coarser resolution can be accepted. In an ideal case no position sensitivity is needed at all. A real effect that might still require some resolution are the suppression of background *outside* the region of interest. And also to align the *roll* of the sample (tilt around the x -axis) a 2-dimensional detector would be favourable. But this task could also be performed with an optional CCD-camera.

$$\begin{aligned}\text{horizontal } \Delta y &\leq 0.5 \text{ mm} \\ \text{vertical } \Delta z &\in [\Delta y, \infty]\end{aligned}$$

rate per pixel Since the pixel size is not defined, here the maximum rate per mm^2 is given. It was obtained by assuming a perfectly reflecting reference sample of $10 \times 10 \text{ mm}^2$ and full beam divergence. The rate¹ per pixel varies in the range

$$\begin{aligned}10^5 \text{ s}^{-1} \text{ \AA}^{-1} \text{ mm}^{-2} &\quad \text{for } \lambda = 5 \text{ \AA} \\ 3 \cdot 10^4 \text{ s}^{-1} \text{ \AA}^{-1} \text{ mm}^{-2} &\quad \text{for } \lambda = 9.4 \text{ \AA}\end{aligned}$$

total rate This quantity was obtained by simulation with the same setting as mentioned above, but by integrating over the full detector. The maximum specularly illuminated area is $2.7 \cdot 10^4 \text{ mm}^2$, but the illumination is not homogeneous. The maximum integral rates are

$$\begin{aligned}5 \cdot 10^8 \text{ s}^{-1} \text{ \AA}^{-1} &\quad \text{for } \lambda = 5 \text{ \AA} \\ 2 \cdot 10^8 \text{ s}^{-1} \text{ \AA}^{-1} &\quad \text{for } \lambda = 9.4 \text{ \AA}\end{aligned}$$

¹The wavelength band width is 0.2 \AA at the detector position, 58.4 m from moderator [$\rightarrow 8.3.1$].

homogeneity The detector images are normalised by division by a reference measurement. Already a relative misalignment of 0.005° leads to a shift of one (0.5 mm) pixel. It is thus crucial that the detector area is homogeneous (if necessary after pixel-wise normalisation) on the order of 1%.

stability The intended measurement scheme requires a reference for each detector image obtained with a sample. To save measurement time, there will be a set of reference sample sizes and orientations available, obtained with standard samples. This requires that the homogeneity of the detector does not change with time (over months), and that the total sensitivity can be detected continuously, so that a renormalisation of the reference is possible.

dynamic range The dynamic range of the detector must be quite high since at the same time one can expect maximum flux on some area of the detector, while it drops by 6 orders of magnitude (or more) for high- q_z or off-specular regions. This can be seen in figure 2.7.

A signal of 10^{-8} relative to the full intensity given by a *small* sample has to be measurable. Small here means 2 orders of magnitude smaller than the reference mentioned above. The signal will then be of the order $5 \cdot 10^8 \text{ s}^{-1} \text{ \AA}^{-1} \times 10^{-2} 10^{-8}$, with $\Delta\lambda = 0.2 \text{ \AA}$. Thus the integral noise of the detector should be below 10^{-2} s^{-1} .

9.2.1 cross-talk

All measurements with the *Selene* prototype were performed with an EMBL wire detector. Recent (08.2013) tests to estimate the contribution of air-scattering to the background revealed that all noteworthy background for these measurements is detector-intrinsic.

The test compared the signal on the detector obtained with a highly collimated beam with various set-ups, namely a flight tube filled with air with and without Al windows, and filled with Ar, all with the detector slit fully open. And a reference with the detector slit closed to 5 mm. The only sizeable effect was the intensity gain when using Ar due to the reduced scattering on N_2 . Figure 9.1 shows the horizontally integrated intensity as a function of the height (in terms of detector angle). The direct beam can be clearly seen at $\theta \approx -0.05^\circ$. The background sets in some 2.5 orders of magnitude below the peak intensity and drops down to 4 orders at the corners. The detector slit opening corresponds to $\Delta\theta \approx 0.2^\circ$

The test-situation is not so far from a typical situation in the high-intensity-mode or the λ - θ -encoding-mode. One part of the detector is illuminated by the totally reflected beam, while other parts should record a signal down to 6 (or even more) orders of magnitude below.

Presumably this cross-talk is responsible for the finite-background problems we've seen in the experiments with the *Selene* prototype.

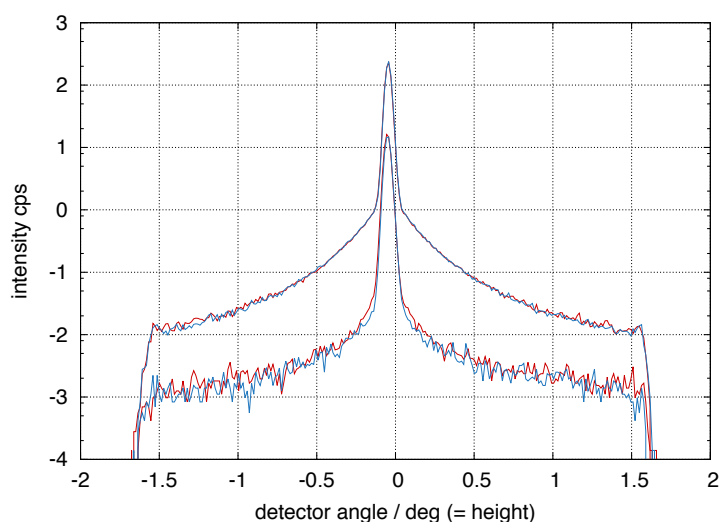


Figure 9.1: Intensity distribution on the Amor area detector integrated horizontally. The detector was illuminated with a vertically collimated beam, corresponding to the sharp peak. For the red curves, the detector slit was completely open, for the blue it was closed to shade the area outside the beam. The upper curves are obtained by integrating λ from 3 \AA to 5 \AA , the lower curves by integrating from 8 \AA to 10 \AA .

10 Measurement Schemes and Data Reduction

This chapter gives a more detailed description of the data collection and processing for the three principle operation modes. Each is presented for a representative sample.¹

[→10.1] A solid/liquid cell, filled with D₂O, measured in the almost conventional mode.²

[→10.2] A NiTi multilayer with (artificial) off-specular scattering, measured with λ - θ -encoding.

[→10.3] A small ferromagnetic sample, measured in the high-intensity specular mode.

For the last mode a full McStas simulation was performed. Due to the lack of (computing and working) time there is no simulation for the conventional mode yet, and for the encoding mode some simplifications (for normalisation and encoding) were made.

To allow for some comparability among the various instrument concepts, the involved teams and some STAP members agreed on a common set of parameters and definitions. It turned out later that these were not precise enough. The parameters used here are:

resolution All data of the following examples are re-binned to $\Delta q/q = c = \text{const}$, where the actual bin-width is half of the wanted experimental resolution. This leads to a q_z -grid with bin n covering

$$q_z \in \left[q_0 \cdot (1 + c)^n, q_0 \cdot (1 + c)^{n+1} \right[$$

The lower q_z limit (for positive n) is \mathbb{E} defined here to be $q_0 = 0.001 \text{ \AA}^{-1}$.

counting time The counting time per individual measurement is chosen in a way that in specular reflectivity the (used) bin with the lowest signal contains 50 counts.³ This corresponds to a relative error of $\sigma = 1/\sqrt{50} \approx 14\%$.

¹ Ideally the samples used here would be reference samples to allow for a comparison of different reflectometer designs. But since they are not defined with all details, we choose a set of samples allowing to highlight the features of $\text{E}\sigma\tau\alpha$.

² Sample suggested by H. Wacklin; size and resolution to be defined.

³ This definition is problematic because it punishes measurement schemes covering a wide q_z -range simultaneously. It might be favourable to measure at more angles of incidence with a wider overlap to shorten the measurement time - sacrificing the design criterion to cover a wide q -range with one angle (e.g. for time-resolved studies or for liquid surfaces). This could partially be compensated by adding some time for sample and detector movement.

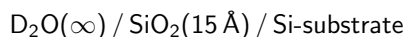
10.1 conventional mode, solid-liquid cell

Liquid samples typically show a high diffuse scattering. This means that one has to choose an operation mode where diffuse scattering does not strongly affect the specular signal, and where it can be measured to some extent to allow for correction. This is why the combination liquid cell / almost conventional mode is chosen.

Measurements using a solid-liquid cell imply the constraint that the beam footprint on the sample surface has to avoid the gasket and the trough walls of the cell.

10.1.1 the sample

The sample is an solid-liquid cell, filled with D_2O .



The sample surface is (size not yet defined). The measurement will be performed through the Si-block.

The interesting aspects of this sample are its diffuse scattering (incoherent scattering from deuterium) and the large dimensions.

There are no sharp features expected in the reflectivity curve of this sample and thus the resolution can be quite relaxed.

10.1.2 the measurement scheme

This mode corresponds to the conventional TOF reflectometry, where the beam divergence and footprint size are defined by slits. The angle of incidence and the divergence are constant for the duration of one pulse. Using the *Selene* guide the footprint is defined by the slit system at the virtual source point. For adjusting the divergence one slit behind the last guide element is sufficient. The still convergent beam avoids illumination of the sample environment.

Due to the analogy with conventional TOF reflectometers, the data collection, normalisation and further treatment for one angle of incidence follow exactly the procedure used there.

An additional feature when using a wide divergence cut down by a slit is that by scanning the slit in between measurements, one can change θ without rotating the sample.

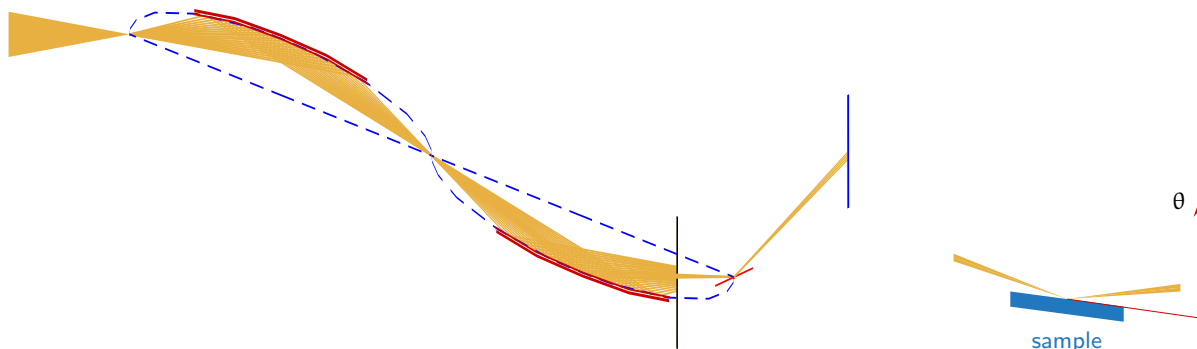


Figure 10.1: Sketch to illustrate the operation scheme: the beam (gold) is transported with the full divergence and without chopping to the end of the guide system. There a slit (black) defines $\Delta\theta$, and together with the sample orientation ω also the angle of incidence θ .

10.1.3 sample alignment

The low-divergent beam defined by the slit allows to align the sample by alternating rocking scans and z -scans⁴. The accuracy is given by the divergence and for larger samples by the footprint. The only difference from conventional TOF reflectometers is that the beam converging at the centre of rotation ideally does not have any parallel components. A z -scan at $2\theta = 0^\circ$ to find the absorbing substrate at the half-shaded beam is thus modified. At $\theta = 0^\circ$ one has the end of the substrate leading to half the intensity, and not the sample centre. For small samples this can be neglected, for large samples one still gets the approximate position.

For a high precision alignment an additional CCD-based detector can be used. It has much higher resolution and fast feed-back (no TOF analysis is necessary).

⁴ Here, z is in the sample coordinate system, i.e. normal to the sample surface

Depending on (the transparency of) the sample environment one can use optical light to pre-align the sample. The divergent white light coupled into the beam before the virtual source point. Besides gravity effects this follows the same trajectories as the neutrons, creating a spot where the centre of rotation should be. This method is used on Amor and on the *Selene* prototype with large success.

10.1.4 data acquisition

For the Si/D₂O interface measured through Si the critical edge is at $q_z^c = 0.0145 \text{ \AA}^{-1}$. This leads to the lowest angular setting $\omega = -1^\circ$. All settings ω and the corresponding q_z -ranges are given in table 10.1.

ω	θ	q_z
-1.0°	0.43°	$0.010 \dots 0.019 \text{ \AA}^{-1}$
-0.9°	0.73°	$0.017 \dots 0.032 \text{ \AA}^{-1}$
-0.6°	1.23°	$0.029 \dots 0.054 \text{ \AA}^{-1}$
-0.2°	2.08°	$0.048 \dots 0.091 \text{ \AA}^{-1}$
0.5°	3.51°	$0.082 \dots 0.154 \text{ \AA}^{-1}$
1.7°	5.95°	$0.139 \dots 0.261 \text{ \AA}^{-1}$
3.8°	10.11°	$0.235 \dots 0.441 \text{ \AA}^{-1}$
7.4°	17.28°	$0.397 \dots 0.746 \text{ \AA}^{-1}$

Table 10.1: Angular settings ω , corresponding θ , and the related q_z -ranges.

The criterion for the counting time is that the highest statistical error per bin (with $\Delta q/q = 2.5\%$) is below 14%.

The measurements each lead to an array $I(y, z, t)$. In most cases (as here), there is no information expected in y direction so that one can project the array to $I(z, t)$. The uncertainties are Δz given by the detector resolution, and $\Delta t = \tau$.

10.1.5 reference measurement

The best normalisation can be obtained using a reference sample cell, where the film is replaced by a supermirror coating of known reflectivity. It is realistic to assume a $m = 10$ coating with a moderate reflectivity.

So for up to $q_z = 0.22 \text{ \AA}^{-1}$ one gets the reference arrays $I_r(y, z, t)$ or $I_r(z, t)$. Correction for the known reflectivity gives $I_{rc}(z, t)$.

Here, the reference cell would be a Si-block with the same measures as the one of the cell, covered with a supermirror coating. No trough or liquid is needed, since only geometrical features and the flight path through Si are relevant.

10.1.6 normalisation and integration

If required, the not specularly illuminated area of the $I(z, t)$ -map can be used to estimate the diffuse background, which can then be subtracted from $I(z, t)$.

A division of $I(z, t)$ by the reference $I_{rc}(z, t)$ pixel-by-pixel gives the reflectivity of the film $R(z, t)$. This can be transferred to $R(q_x, q_z)$, or if the off-specular region can be ignored, the corresponding region of $R(z, t)$ can be projected on a q_z -grid with $\Delta q_z/q_z = \text{const}$. The new q_z -grid should have a lower resolution compared to $R(z, t)$, which is defined by the detector resolution Δz and by τ .

10.1.7 discussion

...⁵

A limiting factor for using the proposed instrument for solid-liquid-cells is the maximum footprint of $50 \times 10 \text{ mm}^2$. Larger samples will profit from some other geometry [$\rightarrow 6.6$], or from a non-focusing instrument.

Within these limitations the intensities and measurement times should be almost the same on all reflectometer types, because the maximum intensity (as allowed by Liouville) is reduced only by the guide transmission.

The q_z -range covered with one angular setting ω is relatively narrow with $q_{z\text{max}}/q_{z\text{min}} = \lambda_{\text{max}}/\lambda_{\text{min}} \approx 1.9$.

⁵ This will follow once the simulations are completed

10.2 λ - θ -encoding, off-specular measurements

The strengths of the λ - θ -encoding are the wider q_z -range accessible with one angular setting, a possible constant $\Delta q/q$, and eventually the *nicer* off-specular area, compared to the almost conventional mode.

This is illustrated at the example of a Ni/Ti multilayer sample with (artificial) Bragg-sheet scattering.

The high resolution $\Delta q_z/q_z = 2\%$ aimed for *here* results in much longer counting times.

10.2.1 the sample

The sample is a multilayer of the composition

$$[\text{Ni} (120 \text{ \AA}) / \text{Ti} (80 \text{ \AA})]_{20} / \text{Si-substrate}$$

with a constant interface roughness $\sigma = 4 \text{ \AA}$. The sample size is

$$10 \times 10 \text{ mm}^2$$

The specular reflectivity was simulated with EDXR [36] The off-specular signal is *generated* by convolution of the specular reflectivity $R(q_z)$ with 2 Gaussian functions $R(q_x, q_z) = R(q_z) * (g_1(q_x) + g_2(q_x))$. with a cut-off at the sample horizon. A bending of the Bragg sheets, Yoneda wings and the low-intensity region between Yoneda and horizon are not produced this way. Within McStas this folding is achieved by randomly adding a q_{xy} component, but with a Gaussian probability distribution centred at $q_{xy} = 0$.

10.2.2 the measurement scheme

There are (at least) two possibilities to obtain a λ - θ -encoding: either by using the pulsed structure and varying the angle of incidence θ with time - and thus with λ . Or to spectrally analyse the beam (no pulsed beam is needed) e.g. by reflecting on a multilayer monochromator, or by refraction using a prism [33].

fast moving slit The slit scans across the convergent beam in the direction of the sample normal for each pulse and thus also creates a λ - θ -encoding. Figure 10.2 shows the principle. The slit position defines $\theta(t \propto \lambda)$. For covering a wide q_z -range it should be located at the high- θ edge at the time the 5 \AA neutrons arrive and at the low- θ edge for 9.4 \AA . The slit width defines $\Delta\theta$. Thus a variation of the slit-width Δy with time can be used to realise $\Delta\theta/\theta = \text{const}$, or more sophisticated, $\Delta q/q = \sqrt{(\Delta\lambda/\lambda)^2 + (\Delta\theta/\theta)^2} = \text{const}$, where $\Delta\lambda = \text{const} \approx 0.2 \text{ \AA}$ here.⁶

⁶ Solving this equation for $\Delta\theta$ gives (l is the slit-sample distance):

$$\begin{aligned} \Delta\theta(t) &= \theta(t) \sqrt{\left(\frac{\Delta q}{q}\right)^2 - \frac{\Delta\lambda^2}{(\lambda_{\min} + (\lambda_{\max} - \lambda_{\min})(\theta(t) - \omega + \epsilon)/\Delta\theta_{\text{beam}})^2}} \\ &\approx \arctan \frac{\Delta y(t)}{l} \\ \theta(t) &= \omega + \epsilon + \frac{\Delta\theta_{\text{beam}}}{2} + \frac{\lambda(t) - \lambda_{\min}}{\lambda_{\max} - \lambda_{\min}} \Delta\theta_{\text{beam}} \\ &= \omega + \arctan \frac{y(t)}{l} \end{aligned}$$

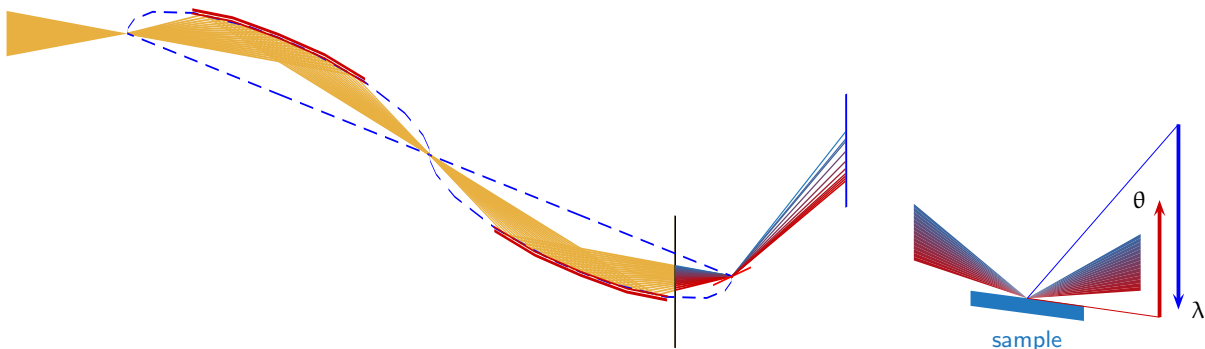


Figure 10.2: Sketch to illustrate the operation scheme: the beam (gold) is transported with the full divergence and without chopping to the end of the guide system. As in the conventional mode [→10.1], a slit (black) defines $\Delta\theta$ and together with the sample orientation ω also the angle of incidence θ . But the opening and position change during the passing of each pulse. This way high θ can be related to low λ and vice versa.

For the simulations presented in this section this mode was chosen.

spectral analysis using a multilayer A ML monochromator at or before the virtual source point encodes the wavelengths of the neutrons in the final angle of the monochromator. For small θ one gets $\theta \propto \lambda$. The specular reflectivity from the sample then leads to a diagonal streak in $I(\lambda, 2\theta)$ on the detector, so that off-specular scattering can be measured. Figure 10.3 shows *snap-shots* of the beam-distribution within the guide and at the sample.

The resolution in q_z is essentially given by the ML monochromator and can reach 2%, while the TOF resolution influences Δq_x (this has to be verified). So this mode could be realised without any chopper. The losses one gets by using a monochromator are (partly) compensated by the quasi-simultaneous measurement on a wide θ -range.

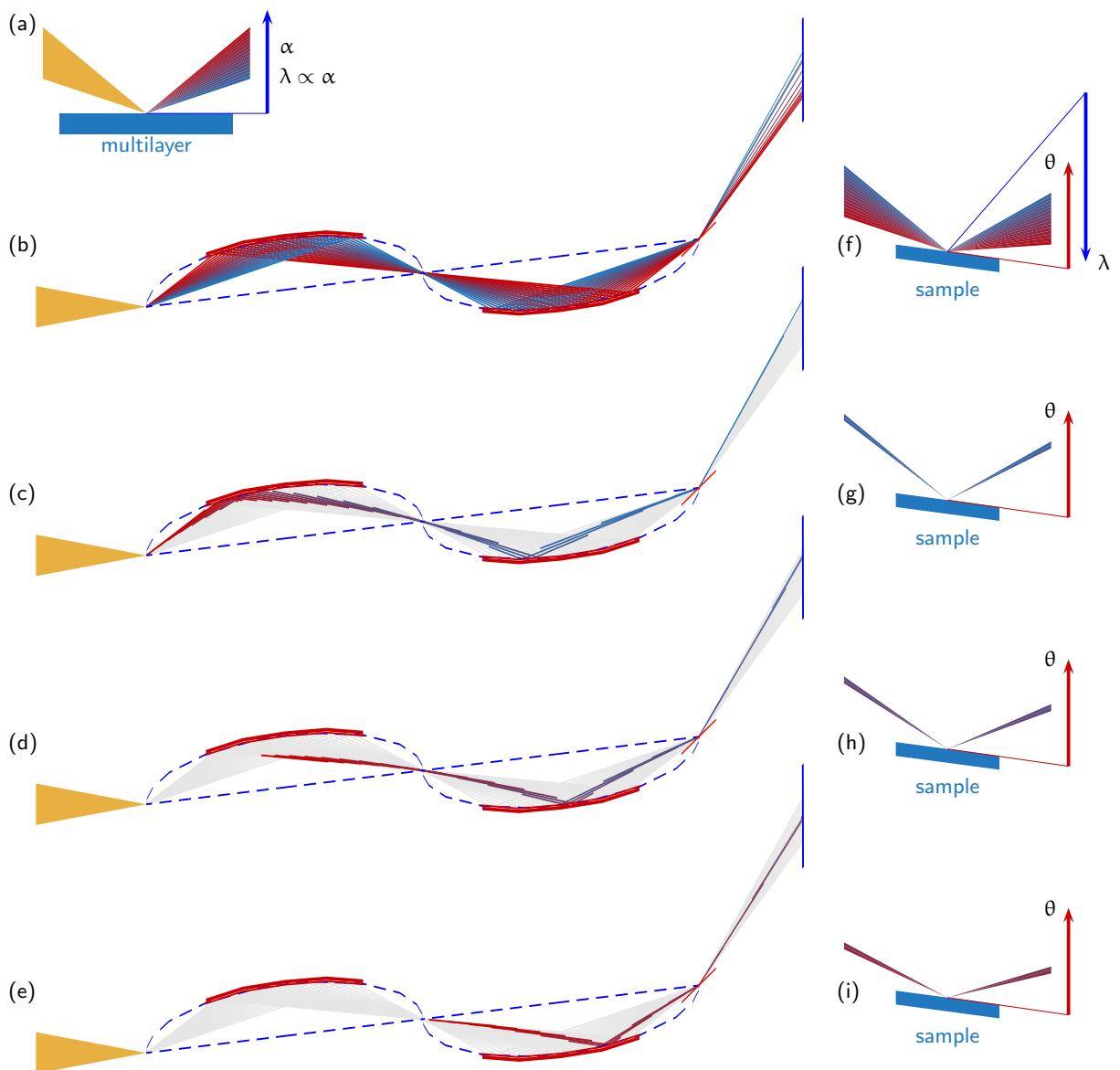


Figure 10.3: Illustration of the principle of the λ - θ -encoding. A convergent white (pulsed) beam is spectrally analysed by a ML monochromator (a). The beam then propagates to the sample keeping the relation between λ and θ (b). For a pulsed beam at any time an almost monochromatic beam is impinging on the sample, where θ and $\lambda \sim \theta$ vary with time. The sketches (c) to (e) show snap-shots of the beam within the *Selene* guide system and after the sample. In (f) to (i) the corresponding situation on the sample is shown.

For a ML with a Bragg peak at $m \cdot 0.022 \text{ \AA}^{-1}$ one gets the proportionality

$$\theta / \text{deg} \approx 0.1 m \lambda / \text{ \AA} \quad (10.2.1)$$

The guide geometry, its coating and the wavelength-range define $\Delta\theta$ [$\rightarrow 6.1$], i.e. for $\lambda \in [5, 9.4] \text{ \AA}$ and $\Delta\theta = 1.5^\circ$ one gets $m \approx 3.4$ with $\theta \in [1.7^\circ, 3.2^\circ]$. A plateau of total reflection ($m \leq 1$) results in $\theta \leq 1^\circ$ for the same λ -range. Thus totally reflected neutrons do not reach the guide.

A ML monochromator leads to an illumination of the *off-specular region* on the detector by diffuse and off-specular scattering at the multilayer, but also by specular scattering away from the Bragg condition. This can be seen in figure 2.7. An additional fast moving slit before the sample (see above) can be used to filter this unwanted intensity from the monochromator. This combination allows for a clean beam and a high and constant resolution.

10.2.3 sample alignment

The sample can be aligned by keeping the otherwise scanning slit behind the guide at a fixed position with small opening. The beam transmitted there is then well-defined, and in the case of using spectral analysis also almost monochromatic. The further procedure follows the one described above [$\rightarrow 10.1.3$].

10.2.4 data acquisition

Also the data acquisition follows the scheme of the almost conventional reflectometry. Only the number of q_z -ranges is reduced, and the counting times are increased. Table 10.2 gives the orientation ω and the related θ - and q_z -ranges for the simulations.

ω	θ -range	q_z -range	t
-0.4°	$0.1^\circ \rightarrow 1.6^\circ$	$0.003 \text{ \AA}^{-1} \rightarrow 0.068 \text{ \AA}^{-1}$	
1.7°	$2.2^\circ \rightarrow 3.7^\circ$	$0.052 \text{ \AA}^{-1} \rightarrow 0.160 \text{ \AA}^{-1}$	30 s
5.0°	$5.5^\circ \rightarrow 7.0^\circ$	$0.128 \text{ \AA}^{-1} \rightarrow 0.305 \text{ \AA}^{-1}$	140 s
10.0°	$10.5^\circ \rightarrow 12.0^\circ$	$0.253 \text{ \AA}^{-1} \rightarrow 0.522 \text{ \AA}^{-1}$	280 s

Table 10.2: Sample orientations ω and related θ - and q_z -ranges for the simulations. The time t is determined by the highest relative error of 14% after rebinning to 2.5%.

For $\omega = -0.4^\circ$ the computational statistics was not sufficient to obtain reasonable results. The angle of incidence close to zero results in a very small number of virtual neutrons to reach the detector. Thus there are lots of empty pixels in the t - y -map of the detector.

Figure 10.4 shows the $I(\lambda, \theta)$ -map for $\omega = 5^\circ$. The diagonal specular streak is clearly visible. The finite resolution due to the opening of the moving slit leads to the elongation of the Bragg peaks along lines originating from $(\lambda = 0, \theta = 0)$. Here this effect is completely covered by the broadening of the reflected beam. The visible off-specular Bragg-sheets are inclined with respect to the mentioned resolution streaks.

10.2.5 reference measurement

For the specular part and $q_z < 0.22 \text{ \AA}^{-1}$ a high- m supermirror with known reflectivity and same shape as the sample can be used for normalisation.⁷ For higher q_z it is possible to correct the reference measurements for the footprint size. To avoid problems with detector inhomogeneities, the same detector area should be illuminated for all measurements.

⁷ A $m = 10$ supermirror with a reflectivity decaying smoothly down to below 10% can be produced with state-of-the-art technology.

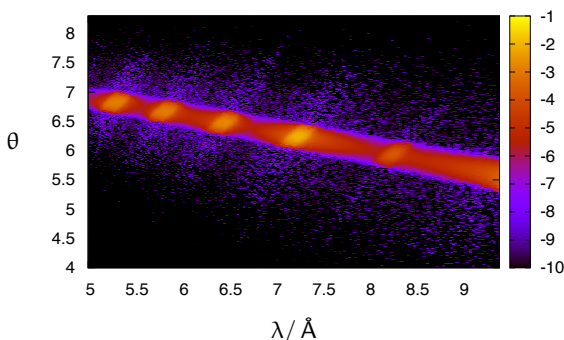


Figure 10.4: Intensity-map $\log_{10}[I(\lambda, \theta)]$ of the NiTi multilayer for $\omega = 5^\circ$. The map is already corrected for $I(\lambda)$ of the incoming beam.

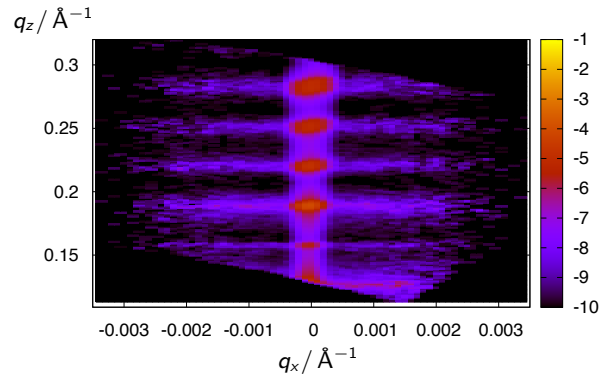
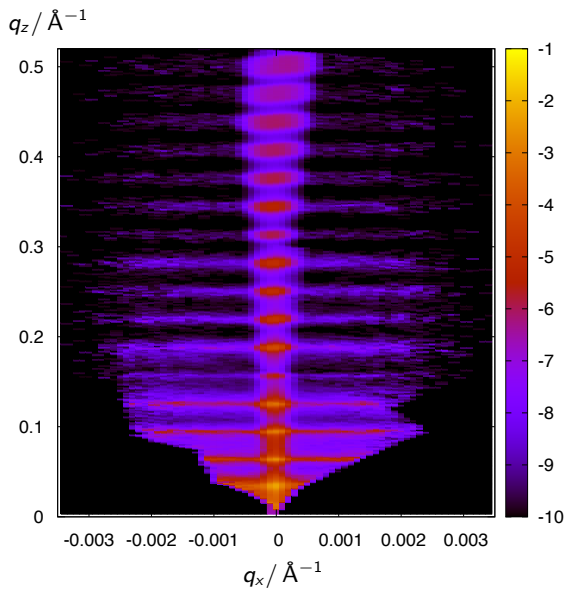


Figure 10.5: Intensity-maps $\log_{10}[I(q_x, q_z)]$ of the NiTi multilayer for $\omega = 5^\circ$ (top), and for all sample orientations given in table 10.2, obtained by summation over the individual maps (left). There is no total reflection plateau visible, here. This is a result of the insufficient computing statistics of the presented map.

10.2.6 normalisation and integration

Normalisation for the off-specular region is a bit more complicated because there is no reference sample with a well-known high-intensity off-specular scattering.

Most likely one has to use the specular reference to also scale the off-specular region, taking inhomogeneities of the detector into account. An alternative, but time-consuming approach is to perform an ω -scan with the reference sample. After illumination correction this mimics an off-specular signal with specular intensity, and the latter is known.

Here, for normalising the simulations a perfect reference sample was assumed, and the *measurement* was repeated without the moving slit. Figure 10.5 shows the $I(q_x, q_z)$ -maps obtained for the four ω orientations, and figure 10.6 the resulting $R(q_z)$ curves.

10.2.7 discussion

The sample was ill-defined with respect to the desired resolution of 2%. The simulations will be repeated with a narrower broadening of the specular intensity. Also the computing time for the lower angles has to be increased.

The main outcome of this simulation is that a good separation of specular and off-specular reflectivity can be reached with the λ - θ -encoding. The number of angular settings to cover $q_z \in [0.01, 0.5] \text{ \AA}^{-1}$ is reduced to 4 relative to the conventional mode needing 7 settings (with 10% overlap).

What can be seen from figure 10.5 is that this method results in a nice shape of the off-specular region.

It is not yet clear if a fast slit system is available. In the worst case one could use a pair of choppers for this purpose, but they would be located quite close to the sample (some 2.3 m).

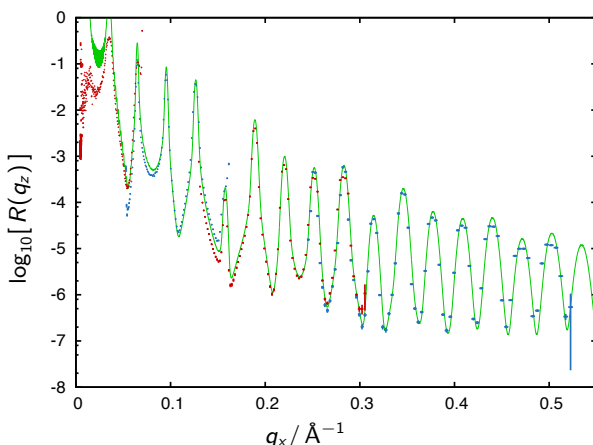


Figure 10.6: $R(q_z)$ of the NiTi multilayer, obtained from the maps shown in figure 10.5 with a binning of $\Delta q/q = 1\%$. The green line is the initial reflectivity convoluted to $\Delta q/q = 2\%$. The data set for $\omega = -0.4^\circ$ clearly shows the insufficient computational statistics. The other data points show a systematic tilt to lower intensities for small q_z . This originates from an improper choice of the Gaussian, widening the specular intensity in q_x direction. This width is larger than the 2% resolution used for data analysis, and thus part of the specular intensity is missing.

10.3 high-intensity specular mode, small magnetic sample

10.3.1 the sample

The sample used for the simulations presented below is a multilayer of the composition

$$\text{Si}(179 \text{ \AA}) / \text{Fe}(12 \text{ \AA}) / \text{Cu}(462 \text{ \AA}) / \text{Si-substrate}$$

The ideal reflectivity was simulated using EDXR [36], where the SLD for magnetic Fe was chosen to be $14.096 \cdot 10^{-6} \text{ \AA}^{-2}$ for $\text{Fe}^{|\rightarrow)}$, and $2.096 \cdot 10^{-6} \text{ \AA}^{-2}$ for $\text{Fe}^{|\leftarrow)}$, respectively. No off-specular or incoherent scattering was assumed. The binning is $\Delta q = 4.4 \cdot 10^{-4} \text{ \AA}^{-1}$. The substrate area is

$$5 \times 5 \text{ mm}^2$$

The sample for this example was inspired by work of B. Wiedemann, TUM, who investigates the magnetic behaviour of thin iron films during growth. According in-situ measurements were performed at REFSANS, MLZ, and are in preparation for Amor, PSI, using the *Selene* prototype. Feasibility studies for the latter were performed with a sample similar to the one used here, but with a larger area.⁸ Figure 11.13 shows the experimental raw-data, the reduced $I(\lambda, \theta)$ -map and the resulting reflectivity curve for spin-down⁹.

10.3.2 the measurement scheme

The full beam leaving the *Selene* guide is directed to the sample. The reflected beam is measured with an area-sensitive detector, whose distance and resolution defines the angular resolution $\Delta\theta$. Each intensity curve obtained by integrating over the detector normal to the scattering plane for a given position along the scattering vector (i.e. a certain θ) corresponds to one TOF measurement.

The increase of specularly reflected intensity is about an order of magnitude larger than with the conventional set-up, or with the λ - θ -encoding. The price to be paid is that the off-specular resolution gets completely lost. The off-specular scattering corresponding to one θ -channel forms a background for all other channels. [→6.6] Most likely there is no way to de-convolve the specular and the off-specular signals.

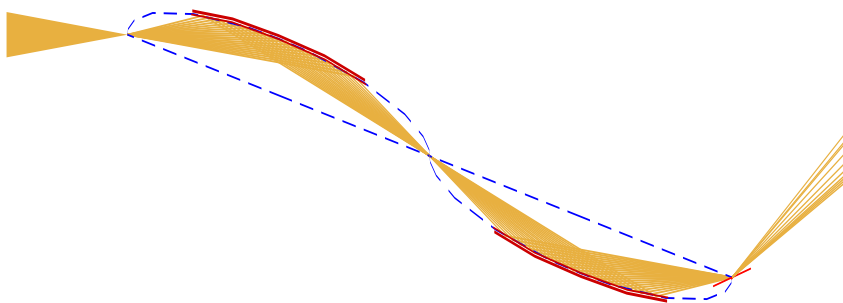


Figure 10.7: Sketch to illustrate the high-intensity specular reflectivity operation mode.

10.3.3 sample alignment

The sample can be aligned by using the slit behind the guide at a fixed position with small opening. This is identical to the situation in the almost conventional mode and thus the scheme described there can be used [→10.1.3].

10.3.4 data acquisition

To cover $q_z \in [0.01, 1] \text{ \AA}^{-1}$ there are 6 angular settings necessary (with a large overlap of 20%). The following table gives the sample tilt ω , the corresponding θ -range, the q_z -range and the counting time needed to have a relative error below 14% in each $\Delta q/q = 2.5\%$ bin.

The simulations were done without polariser (which is not yet realised as a McStas component), and thus only a intensity-loss of 50% due to polarisation was assumed for estimating the counting time. The numbers tell that the limiting factors for the total measurement time will be the sample and detector movements, and the change of temperature and magnetic fields, rather than the actual counting time.

Figure 10.8 (a) shows the $I(\lambda, \theta)$ -map for $\omega = -0.3^\circ$. This was chosen because it can be compared to the actual measurements on a similar (but larger) sample with the prototype set-up on Amor, which is presented on page 81.

⁸ For the off-situ experiments the Fe-layer was prevented from oxidation by covering it with the Si-layer.

⁹ At that time no white spin-flipper was available on Amor.

ω	θ -range	q_z -range	t
-0.3°	$0.2^\circ \rightarrow 1.7^\circ$	$0.005 \text{ \AA}^{-1} \rightarrow 0.074 \text{ \AA}^{-1}$	2 s
1.8°	$2.3^\circ \rightarrow 3.8^\circ$	$0.054 \text{ \AA}^{-1} \rightarrow 0.166 \text{ \AA}^{-1}$	10 s
5.0°	$5.5^\circ \rightarrow 7.0^\circ$	$0.128 \text{ \AA}^{-1} \rightarrow 0.305 \text{ \AA}^{-1}$	20 s
10.0°	$10.5^\circ \rightarrow 12.0^\circ$	$0.253 \text{ \AA}^{-1} \rightarrow 0.522 \text{ \AA}^{-1}$	56 s
17.5°	$18.0^\circ \rightarrow 19.5^\circ$	$0.412 \text{ \AA}^{-1} \rightarrow 0.834 \text{ \AA}^{-1}$	112 s
30.0°	$30.5^\circ \rightarrow 32.0^\circ$	$0.677 \text{ \AA}^{-1} \rightarrow 1.102 \text{ \AA}^{-1}$	336 s

Table 10.3: Sample orientations ω and related θ - and q_z -ranges for the simulations. The time t is determined by the highest relative error of 14% after rebinning to 2.5%.

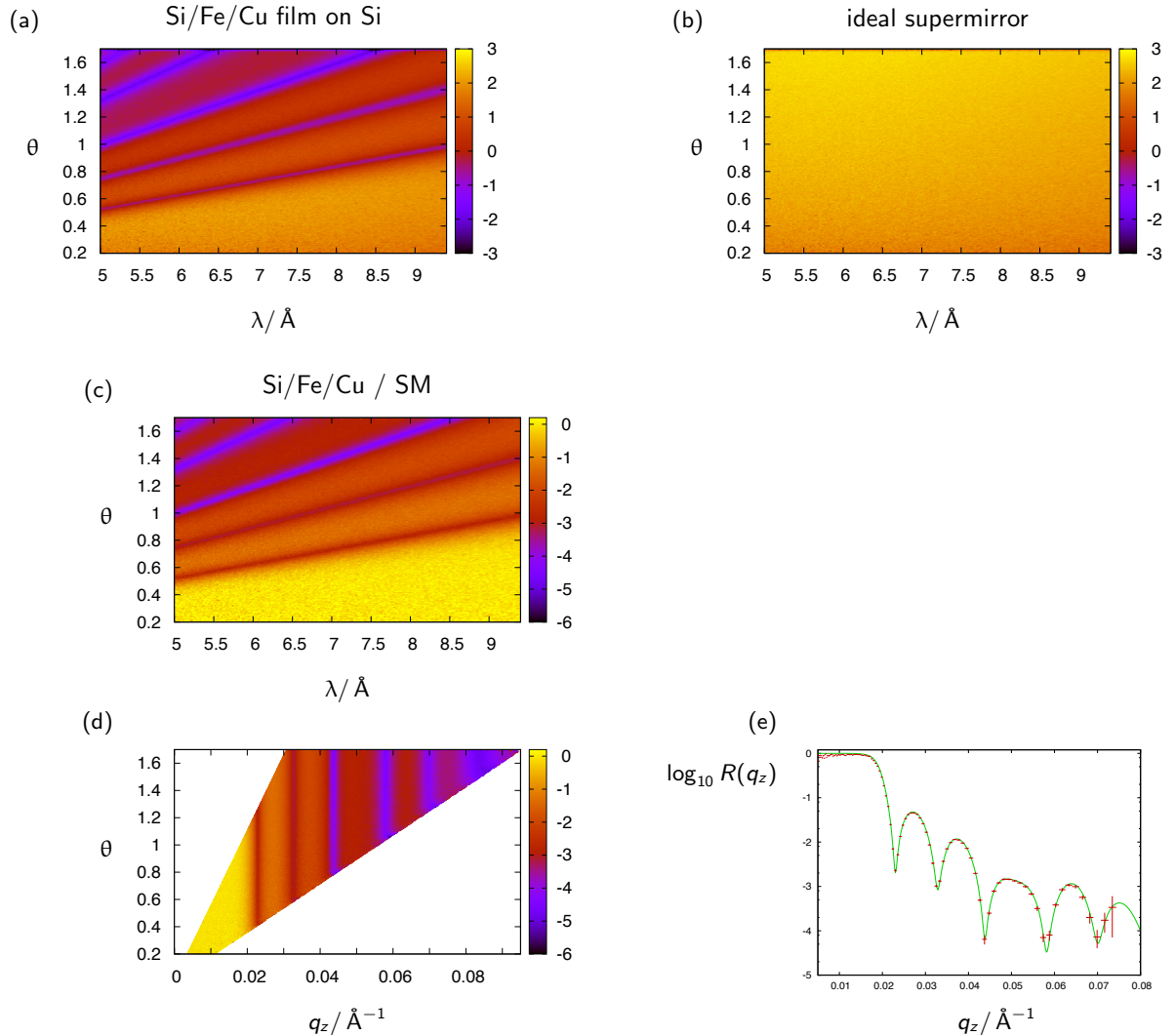


Figure 10.8: Simulated intensity-maps $I(\lambda, \theta)$ for a sample with the composition (a) Si (179 Å) / Fe (12 Å) / Cu (462 Å) / Si and a size of $5 \times 5 \text{ mm}^2$, and for a perfect supermirror with the sample shape (b), respectively. Map (c) is obtained by pixel-wise division of maps (a) and (b). For map (d) λ was converted to q_z . Integration along θ and rebinning to $\Delta q/q = 2.5\%$ lead to the red marks in diagram (e). The green line is obtained by convolving the initial $R(q_z)$ used for the simulations with $\Delta q/q = 2.5\%$.

10.3.5 reference measurement

To normalise the $I(t, y, z)$ data set the best choice is to use a reference sample with the same measures (to guarantee the same footprint) and a high reflectivity over a wide q_z -range. As long as $R_r(q_z)$ of this reference is known, one can correct the reference $I_r(t, y, z)$ to $I_{rc}(t, y, z) = I_r(t, y, z) / R_r(t, y, z)$.

One can think of using a supermirror with $m = 10$, and reflectivity $R > 1\%$ as a reference. This would allow direct corrections up to $q_z = 0.22 \text{ \AA}^{-1}$. Since each reference measurement takes some time, a set of standard

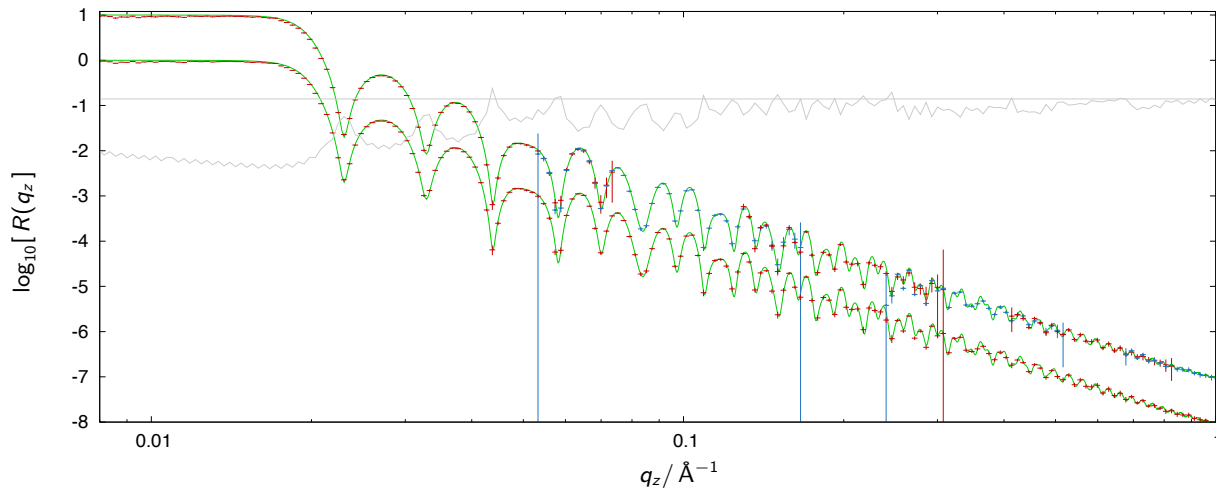


Figure 10.9: Specular reflectivity $R(q_z)$ of the multilayer Si (179 Å) / Fe (12 Å) / Cu (462 Å) / Si. The green curves correspond to the ideal reflectivity, convoluted with $\Delta q/q = 2.5\%$, the upper red and blue data points were obtained by simulations in the high-intensity specular mode for various sample orientations ω [→10.3.4]. These are scaled by 10 for clarity. The lower red data points were obtained by merging the individual *measurements*. The binning has a width of $\Delta q/q = 2.5\%$. The gray curve gives the relative error of the merged $R(q_z)$, the straight gray line is at 0.14.

sample sizes should be defined, for which the corresponding reference measurements are available. This applies also to liquid-solid cells.

For the example in figure 10.8 (b) an ideal supermirror ($R(q_z) = 1 \forall q_z$) was assumed. It can be seen there that the highest intensity occurs at low λ and high θ . The first finding results from the choice of the λ -range [→2.5.1]. The second finding results from the increasing projected sample area for larger θ .

10.3.6 normalisation and integration

In case a reference measurement $I_{rc}(t, y, z)$ is available (i.e. $q_z \leq 0.22 \text{ \AA}^{-1}$) it's possible to normalise the measurement pixel-by-pixel to get

$$R(t, y, z) = I(t, y, z) / I_{rc}(t, y, z) \quad (10.3.1)$$

Summation over y , transformation of t to λ with $\Delta t = \tau$, and z to 2θ with the detector resolution Δz gives a $R(\lambda, \theta)$ -map (Figure 10.8 (c)) with corresponding error-map (not shown). Each line (one θ) corresponds to a reflectivity $R_\theta(\lambda)$ obtained in TOF mode, and each column (one λ) corresponds to a reflectivity $R_\lambda(\theta)$ obtained in an angle-dispersive mode.

There are various schemes to collapse the $R(\lambda, \theta)$ to $R(q_z)$. The approach we followed up to now is the define a q_z -grid (with $\Delta q_z/q_z = \text{constant}$) and to fill in all entries of the $R(\lambda, \theta)$ array according to their q_z . This can be done with full error handling so that at the end each $R(q_{z,i})$ has its own error. Since the resolution varies over the $R(\lambda, \theta)$ array, one gets a non-trivial but known resolution function for $R(q_z)$. [→10.4.3]

Figure 10.8 (e) shows the simulated $R(q_z)$ data points obtained this way, together with the initial (perfect) reflectivity curve smeared with $\Delta q/q = 2.5\%$. The complete procedure was repeated for all ω settings mentioned in section 10.3.4, and the resulting individual reflectivity curves as well as the merged curve are shown in figure 10.9.

For higher q_z , where no reference is available, or the measurement would take too long, it proved to be possible to take a low- ω measurement and eventually correct for the different footprint or projected sample height. In case the detector is not sufficiently homogeneous, one has to take care to illuminate the same area on the detector for all ω .

10.3.7 discussion

counting time The gain of the high-intensity mode over the λ - θ -encoding mode in the present case is a factor 20 for the lowest ω and decreases for increasing ω . The reason is that in the encoding mode $\Delta\theta$ and thus the slit-opening are proportional to θ . At $\omega \approx 30^\circ$ ($\theta \in [30, 5^\circ, 32^\circ]$) the slit-width corresponds to half the full divergence. The time-gain there is only about a factor 2.

The average gain in counting time for a moderate q_z -range (up to $\approx 0.5 \text{ \AA}^{-1}$) will be one order of magnitude.

For larger samples, relaxed resolution (binning) requirements, or lower counting statistics it is possible to reach the split-second time-scale for time-resolved measurements. The q_z -range one can cover in one shot e.g. spans from 0.01 \AA^{-1} to 0.085 \AA^{-1} .

resolution Even though the resolution function is quite complex, the final $R(q_z)$ curve follows the simulated curve convoluted with 2.5% resolution up to high q_z . So even without a data treatment as suggested in section 10.4.3 a reasonable result is achievable in the high-intensity mode. This is in agreement with the experimental findings obtained with the *Selene* prototype.

dynamic range The dynamic range of 8 orders of magnitude obtained in the simulations is not realistic. The simulations ignored all background from the sample itself, from the sample environment, and from the detector. And the sample was assumed to show no off-specular or diffuse scattering. Especially the implications of the latter will have to be investigated in future simulations.

10.4 aspects on the data reduction

10.4.1 raw-data and intensity-maps

Each neutron detected on the position sensitive detector has the associated parameters t , y and z for the time-of-flight and the position on the detector. The detector spatial resolution gives the constant values Δy and Δz , the pulse length sets an upper limit for $\Delta t \leq \tau$. The latter one might be reduced by choppers.

From these basic parameters and the instrument parameters X (source detector distance) and θ_{detector} one can calculate the neutron wavelength [\rightarrow 8.3.1]

$$\lambda = \frac{h}{m_n} \frac{t}{X} \quad (10.4.1)$$

and the final angle after reflection

$$\theta_f = \epsilon + \omega - \arctan z \quad (10.4.2)$$

where ω is the inclination of the sample surface relative to the long axis of the last ellipse of the *Selene* guide, z is the position on the detector if that one is located at $\theta_{\text{detector}} = \epsilon + 2\omega$.

Discretisation in λ and θ_f of a large ensemble of events gives the intensity-map $I(\lambda, \theta_f)$ with the error-map $E(\lambda, \theta_f) \approx \sqrt{I(\lambda, \theta_f)}$. The approximation is valid for more than 10 counts per bin. For less counts a correcting factor has to be taken into account. Zero counts is also a measured quantity and has to have an error. This topic has to be investigated further!

It is also possible to extract $I(q_z)$, $E(q_z)$ or $I(q_z, q_x)$, $E(q_z, q_x)$, instead.

10.4.2 normalisation

The measured intensity-map $I(\lambda, \theta)$ is not only a function of $R(q_z)$ of the sample, but also of the intensity $I_{\text{sample in}}(\lambda, \theta, x, y)$ incident on it. This quantity could ideally be measured with a reference sample with $R(q) = 1$ and exactly the same shape and position as the sample. Non-perfect reflectivity can be corrected for as long as $R_{\text{reference}}(q)$ is known and homogeneous. One could e.g. use a supermirror-coated reference with $m = 10$ (and low reflectivity) to correct up to $q_z = 0.22 \text{ \AA}^{-1}$.

For higher q_z this approach is unrealistic. On the other side the projected sample height is larger, which leads to an averaging over beam inhomogeneities. So it might be possible to use a calculated or simulated reference. The quality of the calculation or simulation can be checked by comparison to the reference below $q_z = 0.22 \text{ \AA}^{-1}$.

integration normal to the scattering plane The normalisation can be performed after integrating in y direction on the detector, i.e. normal to the scattering plane. This is justified by

$$\begin{aligned} I(t, y, z) &= I(t, z) \cdot g(y) \\ \frac{\int I(t, y, z) dy}{\int I_0(t, y, z) dy} &= \frac{\int I(t, z) g(y) dy}{\int I_0(t, z) g(y) dy} \\ &= \frac{I(t, z) \int g(y) dy}{I_0(t, z) \int g(y) dy} \\ &= R(t, z) \end{aligned}$$

where $g(y)$ gives the intensity distribution in y direction. By using a single detector or a 1D position sensitive detector this integration is already realised. This is the case in many conventional reflectometers.

10.4.3 resolution

In most cases the resolution function $f(q_z)$ with $R_e(q_z) = R(q_z) * f(q_z)$ will neither be constant nor proportional to q_z . It is thus dangerous to add several data sets, e.g. data obtained with various ω .

summation of data sets with different resolution The summation of data sets $R_i(q_z)$ with weight a_i and individual resolution function $f_i(q_z)$ is possible, but it leads to a complicated (i.e. not single-Gaussian) resolution function f_Σ :

$$\begin{aligned}
 R_\Sigma &= \sum_i a_i R_i \quad , \quad \sum_i a_i = 1 \\
 &= \sum_i a_i R * f_i \\
 \mathcal{F}[R_\Sigma] &= \mathcal{F}\left[\sum_i a_i R * f_i\right] \\
 &= \sum_i a_i \mathcal{F}[R * f_i] \\
 &= \sum_i a_i \mathcal{F}[R] \cdot \mathcal{F}[f_i] \\
 &= \mathcal{F}[R] \cdot \mathcal{F}\left[\sum_i a_i f_i\right] \\
 &= \mathcal{F}\left[R * \left(\sum_i a_i f_i\right)\right] \\
 R_\Sigma &= R * \left(\sum_i a_i f_i\right) \\
 &:= R * f_\Sigma
 \end{aligned}$$

Simulation or fitting of $R(q_z)$ is possible when $f_\Sigma(q_z)$ can be estimated, and when it is taken into account in the simulation software.

Such a reflectivity profile might not be suited for publication because the abrupt changes in $f_\Sigma(q_z)$ at the joints can lead to significant features in R_Σ .

convolution to $\Delta q/q = \text{const}$ In cases when the experimental resolution function $f_e(q)$ of one data set $R_e(q) = R(q) * f_e(q)$ is known, one can convolve $R_e(q)$ with a resolution $f_c(q)$ in a way to get $R_p(q)$ with $\sigma_p \propto q$, i.e. $\Delta q/q = \text{const} := p$. For Gaussian functions

$$f_{e/c}(q) = \frac{1}{\sqrt{2\pi} \sigma_{e/c}} \exp\left[-\frac{(q - q_{e/c})^2}{2\sigma_{e/c}^2}\right] \tag{10.4.3}$$

the relation

$$\begin{aligned}
 f_p(q) &= f_e(q) * f_c(q) \\
 &= \frac{1}{\sqrt{2\pi} \sigma_p} \exp\left[-\frac{(q - q_p)^2}{2\sigma_p^2}\right] \quad \text{with} \quad \sigma_p^2 = \sigma_e^2 + \sigma_c^2, \quad q_p = q_e + q_c
 \end{aligned} \tag{10.4.4}$$

holds. σ_p is related to the full-width-at-half-maximum Δq via

$$\exp\left[-\frac{(\Delta q/2)^2}{2\sigma_p^2}\right] = 0.5 \tag{10.4.5}$$

$$\begin{aligned}
 \Delta q &= \sqrt{8 \ln 2} \sigma_p \\
 &\approx 2.3548 \sigma_p
 \end{aligned} \tag{10.4.6}$$

$$\begin{aligned}
 \sigma_p &= (8 \ln 2)^{-1/2} \Delta q \\
 &= (8 \ln 2)^{-1/2} p q
 \end{aligned} \tag{10.4.7}$$

and thus

$$\sigma_c(q) = \sqrt{\sigma_p^2(q) - \sigma_e^2(q)} \quad (10.4.8)$$

$$= \sqrt{\frac{pq}{8 \ln 2} - \sigma_e^2(q)} \quad (10.4.9)$$

So when $\sigma_e(q)$ is known one can get the *correcting Gaussian*.

Avoiding $\sigma_c \leq 0$ leads to the constraint

$$p > \sqrt{8 \ln 2} \frac{\sigma_e(q)}{q} \quad \forall q$$

The resulting *corrected* reflectivity curve is then

$$\begin{aligned} R_p(q) &= R_e(q) * f_c(q) \\ &= \int_{\bar{q}=q_{\min}}^{q_{\max}} R_e(q - \bar{q}) \cdot \frac{1}{\sqrt{2\pi} \sigma_c(\bar{q})} \exp \left[-\frac{\bar{q}^2}{2\sigma_c(\bar{q})^2} \right] d\bar{q} \end{aligned} \quad (10.4.10)$$

This¹⁰ now allows to merge several data sets after bringing them to the same resolution for each q in the overlapping region. Information is of course lost by lowering the resolution, but the resulting $R_p(q)$ and eventually a merged $R_\Sigma(q)$ have the appearance expected by standard software, most of the users, and almost all readers of publications.

¹⁰It remains to be verified if this is valid for $\sigma = \sigma(q)$.

11 Prototype

11.1 design considerations

The prototype was designed to operate in a λ - and θ -range close to what can be expected for a reflectometer at the ESS, paying respect to the beam characteristics and spacial constraints at BOA (11.3.1) and Amor (11.4.1).

- length of the focusing section ($= 4c$): The available space at BOA is some 9 m. About 3 m are needed to get an acceptable angular resolution on the detector ($\Delta\theta \approx 0.04^\circ$). Another 1.5 m before the first focal point are required for the ml-monochromator, the chopper and eventually further equipment. This led to $4c = 4$ m.
- divergence: The divergence was chosen to be slightly larger than what is available at BOA or Amor, i.e. $\Delta\theta = 1.8^\circ$.
- ellipse parameters: The effective length was defined to $\xi = 0.60$, leading to $b/a = 0.021480$.
- λ -range: The λ -range was selected based on the considerations made in (2.5.1) to be $\lambda \in [3.8, 12] \text{ \AA}$. This results in a coating with $m = 4$.
- sample size: For $c = 1$ m and the typical $b/a \approx 0.02$ the maximum spot size with only small influence of coma aberration is $1 \times 1 \text{ mm}^2$. Larger spots are possible, but the footprint then is no longer homogeneous.
- chopper speed and pulse length: To cover the required λ -range in time-of-flight with a possible chopper-detector distance of some 8 m one needs a frequency of $\approx 60 \text{ s}^{-1}$. The chopper opening-to closing time ratio is the same as for the ESS pulses, i.e. 0.04.

11.2 devices

Most of the following devices were designed, constructed and fabricated at PSI. The exceptions are the X95 elements, the precision slit and the guide elements.

11.2.1 pulse chopper

The reduced length of the set-up compared to the ESS dimensions with about the same λ -range leads to shorter repetition rate and pulse length for the test set-up. The pulse chopper will operate with up to 60 Hz, its open/closed time ratio is about 5% (to be determined exactly). The chopper disc has 2 openings.

The much reduced dimension of the beam relative to conventional set-ups leads to a disc diameter of $\varnothing = 160$ mm. The absorbing material is 2.2 mm of an Al 10 B alloy, followed by 2 mm Cd. The absorbing region is 10 mm wide. Figure 11.1 shows on the left side the pulse chopper after assembling, before testing.

The pulse chopper is equipped with a laser-based trigger for the TOF data acquisition. Since this system detects each gap opening of the chopper, no correction for the second gap and eventually a phase error is needed.

11.2.2 frame-overlap chopper

The frame overlap chopper has similar dimensions as the pulse chopper, but a open/close time ratio of 50%. Its position is at or close to the intermediate focal point of the *Selene* guide system. The frequencies and phases of pulse- and frame-overlap-choppers can be locked. The frame overlap chopper is the left device in figure 11.1.

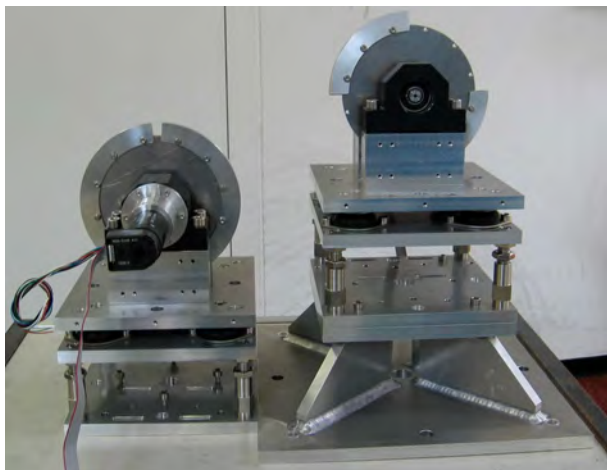


Figure 11.1: Pulse chopper (left) and frame overlap chopper (right) for the *Selene* prototype.

11.2.3 precision slit

The small dimensions of the prototype results in a down-scaling of the sample and thus of the slit at the first focal point. The beam cross-section is of the order $0.1 \times 1 \text{ mm}^2$. This will be realised with a precision x-ray slit system, equipped with BorAl and Cd absorbers. The slit is custom made by ACS and based on their system STT-100-20.

During the experiments on BOA the slit failed several times. In the end it could not be used other than for defining a fix opening of approximately $0.5 \times 1 \text{ mm}^2$.

11.2.4 double multilayer monochromator

The double multilayer monochromator consists of 2 borcron glass substrates, coated with a Ni/Ti multilayer with a first order peak at $m = 3$ with $\Delta q/q = 7\%$. The surfaces are mounted parallel face to face with a gap of 6.5 mm. The first substrate is 305 mm long, the second 119 mm. In x direction there is a 5 mm gap in between both. The design is optimised for a slit positioned 43 mm behind the end of the device. The acceptance is $\Delta\theta = 1.8^\circ$ for $\lambda \in [4, 10] \text{ \AA}$.

The device was tested and characterised on Amor. Since the divergence available for this test was only of the order of 0.3° , the full angular range was reached by tilting the monochromator in discrete steps. Figure 11.2 shows the resulting $I(\theta, \lambda)$ map. The width of the intensity streak shown here is limited by the measurement range, not by the device.

To characterise $\Delta\lambda/\lambda$ and the off-specular scattering, measurements were also performed with a well collimated beam (slits of 1 mm opening, 100 mm and 2200 mm from the entrance of the device). The $I(\lambda)$ curves for various θ are shown in figure 11.3.

Figure 11.4 shows the off-specular scattering for $\lambda = 6.3 \text{ \AA}$ with various slit positions and openings behind the device. The slits before the ml-monochromator are 1 mm each. Surprisingly there is the same broad diffuse background with an exponential decay for all measurements. The origin most likely is a feature of the detector [$\rightarrow 9.2.1$].

11.2.5 sample holder

The sample holder is simply an Al cuboid with grooves and slits to insert (glue) the sample and some absorbing sheets. It is mounted on a y and z translation stage.

11.2.6 guide support

The guide support system is assembled from X95 profiles and joints, motorised and manual translation tables and manual tilting stages. Figure 11.5 shows the mounting frames for the single guide elements (figure 11.7), the height and tilt-adjustments and the X95 bar where upon the guide elements are mounted. This bar is positioned on tilting- and translation stages, which are to be mounted to the lower rotation stages of the BOA tables 3 and 4, respectively.

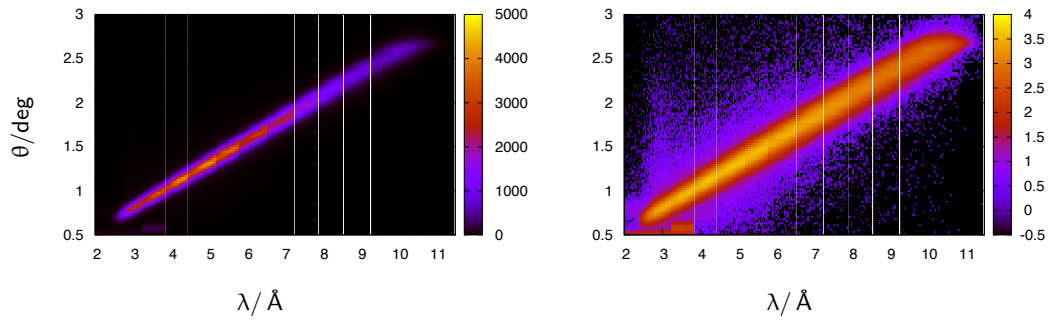


Figure 11.2: $I(\lambda, \theta)$ on linear (left) and logarithmic scale (right) obtained with the ml-monochromator on Amor. The maps are stitched together from 11 measurements since the incoming divergence was limited to 0.3° .

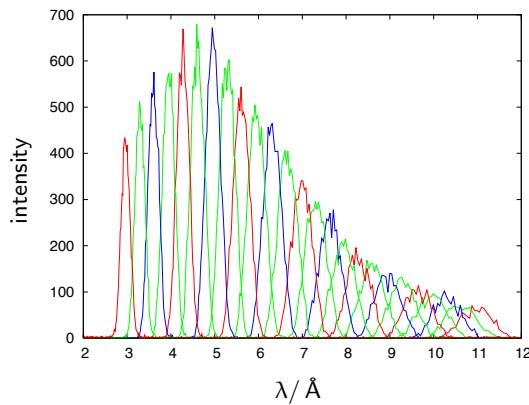


Figure 11.3: $I(\lambda)$ for $\theta = 0.5^\circ, 0.6^\circ, \dots, 3.0^\circ$. The varying height of the individual scans reflects the λ -dependence of the intensity of the incoming beam.

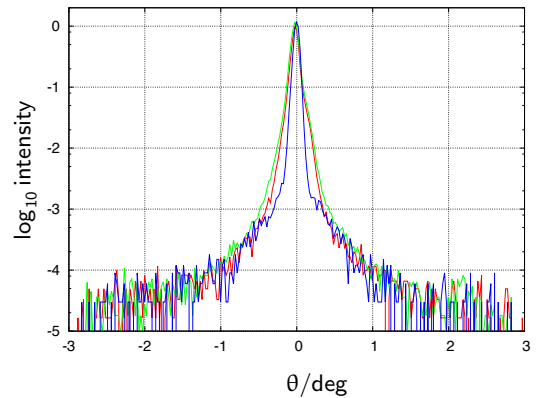


Figure 11.4: $\log_{10}[I(\theta)]$ without aperture behind the device (green), with a 0.5 mm aperture at 50 mm (red), and with a 1 mm aperture at 1300 mm (blue).

11.2.7 guide system

The *Selene* guide system in this case consists of 2 sections focusing elliptically in two dimensions (i.e. in y and in z), where each section consists of 2 mirror-inverted elements of 600 mm length. Figure 11.7 shows one guide element before mounting.

The device was constructed and build by SwissNeutronics according to the measures

$$\begin{aligned}
 c &= 1000.000 \text{ mm} \\
 a &\approx 1000.231 \text{ mm} \\
 b &\approx 21.485 \text{ mm} \\
 b/a &= 0.021480 \\
 \xi &= 0.6 \\
 \Delta\theta &= 1.8^\circ \\
 \epsilon &= 1.5^\circ
 \end{aligned}$$

The coating is a Ni/Ti supermirror with $m = 4$. The horizontally reflecting glass substrate has a constant height of 46 mm. The vertically reflecting glass has one straight edge along the optical axis, and one elliptically curved edge, fitting the horizontal reflectors shape. The vertical reflector has a minimum width of 21 mm.



Figure 11.5: Parts of the guide support before mounting the guide elements.



Figure 11.6: Guide support with 2 guide elements mounted. Shown is the second guide of the *Selene* set-up, reflecting left and downwards. The guides are not yet adjusted, the knife blade slit is missing.



Figure 11.7: Single guide element (half a guide section). The blue part is an L-shaped Al bar on which the glass substrates are screwed. The Al frames are for mounting the elements on the support and alignment system.

11.3 experiments on BOA

The *Selene* prototype was first set up and tested on the beamline BOA at SINQ, PSI, in August and September 2012. The team members for this campaign were U. B. Hansen, T. Panzner, and J. Stahn.

The intensity available at BOA together with the high background limited strongly what could be measured. Since both chopper and ML-monochromator have a transmission of only ca. 5%, it was not possible to operate them simultaneously for TOF λ - θ -encoding.

In the meantime (11. 2012) the background could be reduced by almost 2 orders of magnitude, so further tests on BOA are scheduled for December 2012 and for 2013.

11.3.1 BOA

BOA stands for "beam line for neutron optics and other applications" and is operated by the Neutron Optics group within the Laboratory for Development and Methods at PSI.[37] The beam line is a 18 m long instrument located at beam-channel 51 looking at the SINQ cold source which delivers a neutron spectrum from 1.5 Å to 20 Å. The guide section contains a supermirror bender unit inside the SINQ biological shielding. Thus the beam is permanently polarised in vertical direction.

The flexible space is 12.5 m long (n-flight path) and 3.5 m wide, where the first part is occupied by an anti-trumpet within a concrete shielding. The instrument is equipped with 5 x -translation tables on an optical bench, where the 3 latter are motorised and hold each a y -translation stage. On these platforms optional ω and 2θ rotation stages, goniometers, and further translation stages can be mounted. An area sensitive CCD camera system, a ^3He neutron counter system, and a ^3He area detector (EMBL) are used for data acquisition. Figure 11.8 shows the essential components of the beamline with the *Selene* prototype set-up in place.¹

11.3.2 set-up

All components were mechanically ready by mid August 2012. The installation on BOA started on 13. August. In parallel the motorised components were commissioned and integrated into the instrument control system (translation devices, slit system) or operated as stand-alone solutions (choppers).

First the complete set-up was realised using the instrument's laser for the mean beam direction and the instrument's light source giving a white divergent light to align the guide elements. *Figure of merit* at the beginning was to achieve a symmetric, small light spot at the focal points, and a homogeneous, gap-free light distribution on the detector. The first requirement could be fulfilled rather easily (the spot at the sample

¹section provided by U. Filges, PSI

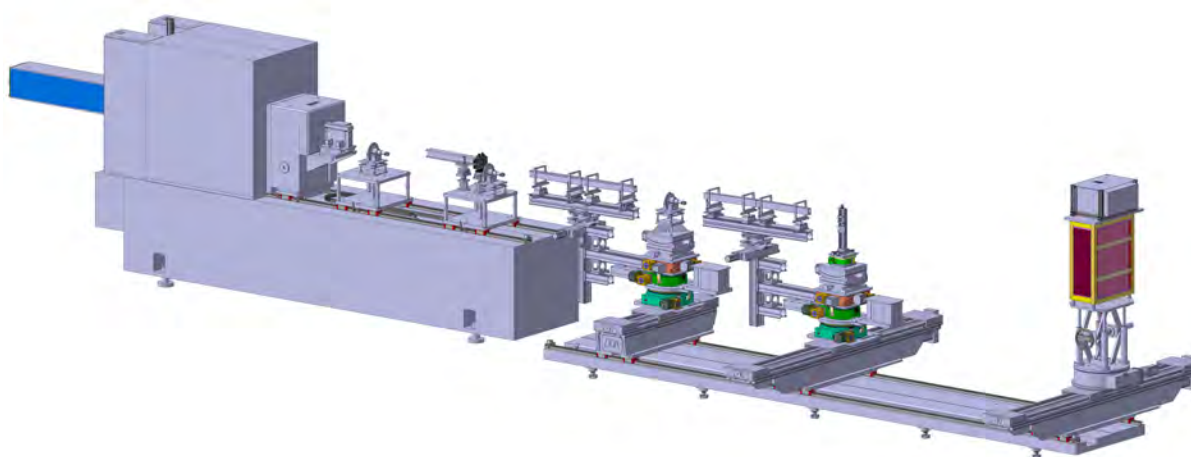


Figure 11.8: Assembly drawing of the construction of the *Selene* prototype set-up on the test facility BOA at PSI. The elements/devices from left to right: n-guide of BOA; pulse chopper on table 2; double ml monochromator, precision slit, pulse chopper (alternative position) on table 3; first guide section on support system, attached to table 4; frame overlap chopper on table 4; second guide section on support system, attached to table 5; sample holder on yz translation stage on table 5; and area detector on table 6.

position is almost identical to the one defined by a pin-hole). The second task proved to be more complicated since the light source produced a highly structured beam, covering mis-alignments. Thus in a later stage a high-power LED with a reflector (bicycle front light) was used in front of the pin-hole.

11.3.3 experiments in TOF mode

The choppers were operated at 1800 min^{-1} , i.e. with a pulse rate of 60 s^{-1} . The phase of the frame-overlap chopper was chosen to select $\lambda \in [2, 13] \text{ \AA}$.

characterisation of the beam

The beam characteristics behind the precision slit were measured with the area detector 5100 mm behind the slit in TOF mode. Due to the bender section in the BOA neutron guide the divergence is strongly patterned in horizontal direction. Reflections on sidewalls (anti-trumpet) and on roof and bottom lead to the higher divergence contributions. In between there is a low-intensity gap. Figure 11.9 (a) and (b) shows the intensity

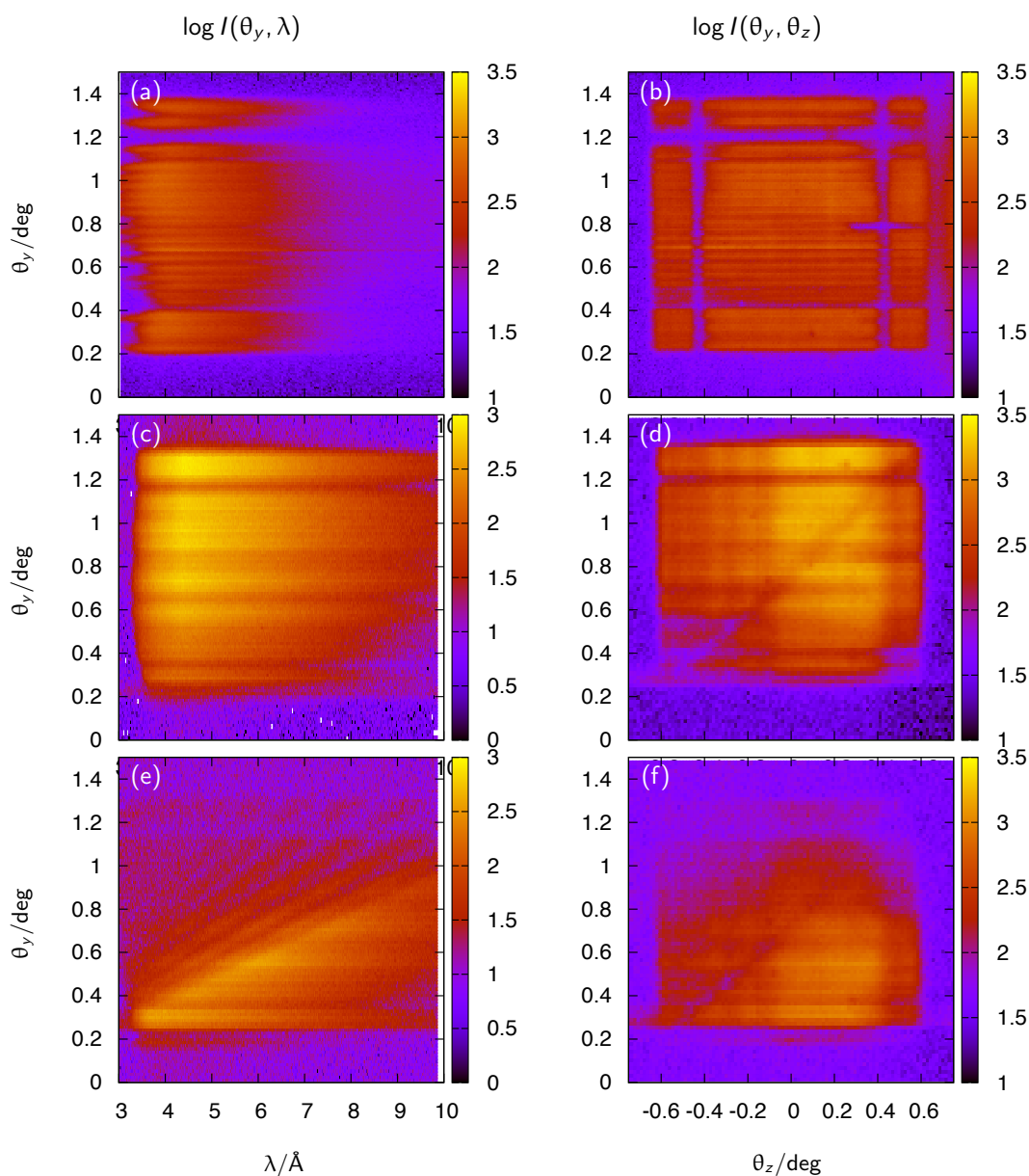


Figure 11.9: Intensity maps $\log I(\theta_y, \lambda)$ and $\log I(\theta_y, \theta_z)$ for the beam emerging from the precision slit (a) and (b), after the *Selene* guide being reflected by a $m = 5$ Ni/Ti supermirror (c) and (d), and being reflected by a 1000 \AA thick Ni film on glass (e) and (f).

maps $I(\theta_y, \lambda)$ and $I(\theta_y, \theta_z)$, obtained from the TOF data by integrating horizontally, or over time. The dark horizontal area in (b) on the right side results from a mechanical damage in the bender section. The horizontal high-intensity streak at $\theta_y \approx 0.7^\circ$ is a feature of the area detector.

Map (a) shows the strong λ dependence of the primary intensity. The $I(\lambda)$ depends also on where the individual channels of the bender point towards the moderator.

The large dynamic range of $I(\lambda)$ here is attenuated by the 4 reflections in the *Selene* guide, which mainly affect short wavelengths.

reflection of a $m = 5$ supermirror

For normalisation of the beam reflected off a sample, a similar measurement using a supermirror can be used. Available are such references with a Ni/Ti supermirror coating of $m = 5$ with area $1 \times 2 \text{ mm}^2$, $3 \times 3 \text{ mm}^2$, and $10 \times 10 \text{ mm}^2$.

Figures 11.9 (c) and (d) show intensity maps similar to the ones mentioned above, but this time measured using the *Selene*-guide. The sample was the $10 \times 10 \text{ mm}^2$ SM, the beam size was 1 mm high and 0.5 mm wide. This means that the sample was illuminated completely along the neutron beam direction. The diagonal dark streak visible in figure 11.9 (d) originates from the areas of the *Selene* guide elements where the horizontal and the vertical reflector join. Tiny errors in the surface quality and the shape of the substrates (caused by the cutting process) lead to a lower reflectivity there. This is inherent to the Montel-type optics. For larger guide systems this feature will be much weaker since the absolute width of the distorted area stays the same, while the guide dimensions get much larger.

The stripe pattern visible in both maps has several origins: besides the inhomogeneities imposed by the beam characteristics of BOA, there are imperfections of the guides (waviness) and more severe, inhomogeneities of the area detector.

The low-intensity region in 11.9 (d) in the lower left corner is a feature of the *Selene* optics: the coma aberration is corrected for in space, but in momentum space some inhomogeneities remain.

reflection of a 1000 Å thick Ni film on glass

The reference sample for characterising and adjusting the TOF reflectometer Amor that was used was a 1000 Å thick Ni film on glass. Figures 11.9 (e) and (f) show the corresponding intensity maps. The *triangle* below the diagonal in map (e) is caused by total reflection off the Ni film. Thus it looks similar to the same region in map (c). The fan-like structure corresponds to the Kiessig fringes. Each horizontal line can be seen as a TOF measurement of a range of the reflectivity curve, where θ_y acts as a scaling factor. But also each vertical line represents a reflectivity measurement, this time in angle-dispersive mode for a given λ .

To obtain a reflectivity curve, the intensity map from the sample has to be divided pixel-by-pixel by the reference measurement (here with the SM). The result is shown in figure 11.10 (a). Then $I(\theta_y, \lambda)$ is transferred to $I(\theta_y, q_z)$ on an (here) equidistant q_z grid to give map (b). Then each horizontal line is normalised so that the total reflection plateau is at $I = 1$. The horizontal stripes still visible in map (c) have 2 origins: e.g. the prominent line at $\theta_y \approx 1.2^\circ$ results from the division of noise by noise in the angular region where (nearly) no intensity is available. The sharper lines result from inhomogeneities of the detector. The maps have not been measured on exactly the same area of the detector, but were shifted by some pixels. Thus the normalisation did not correct for different efficiencies of the detector.

The reflectivity curve in Figure 11.10 (d) was obtained by a weighted summation over the θ_y -channels. No error-handling was applied so far with the consequence that the noise from the region $\theta_y \approx 1.2^\circ$ dominates the curve at high q_z . In this graph only 5 Kiessig fringes are clearly visible, while in the maps one can count 7. This means a more accurate data analysis will provide a better $R(q_z)$ curve. But still the background sets a limits at about 10^{-3} . This is why the experiment is going to be repeated on the TOF reflectometer Amor, which reaches 10^{-5} for small samples ($5 \times 5 \text{ mm}^2$) in a reasonable time in *normal* operation.

11.3.4 experiments with angle-wavelength-encoding

For these measurements the chopper was stopped (in the open position), and the double ML-monochromator was installed before the precision slit. Measurements analogous to the ones discussed in 11.3.3 were performed. But in this case the inhomogeneities of the detector prevent the calculation of $R(q_z)$, thus a repetition is planned where it is made sure that both maps, from the sample and from the reference, are collected on exactly the same area on the detector.

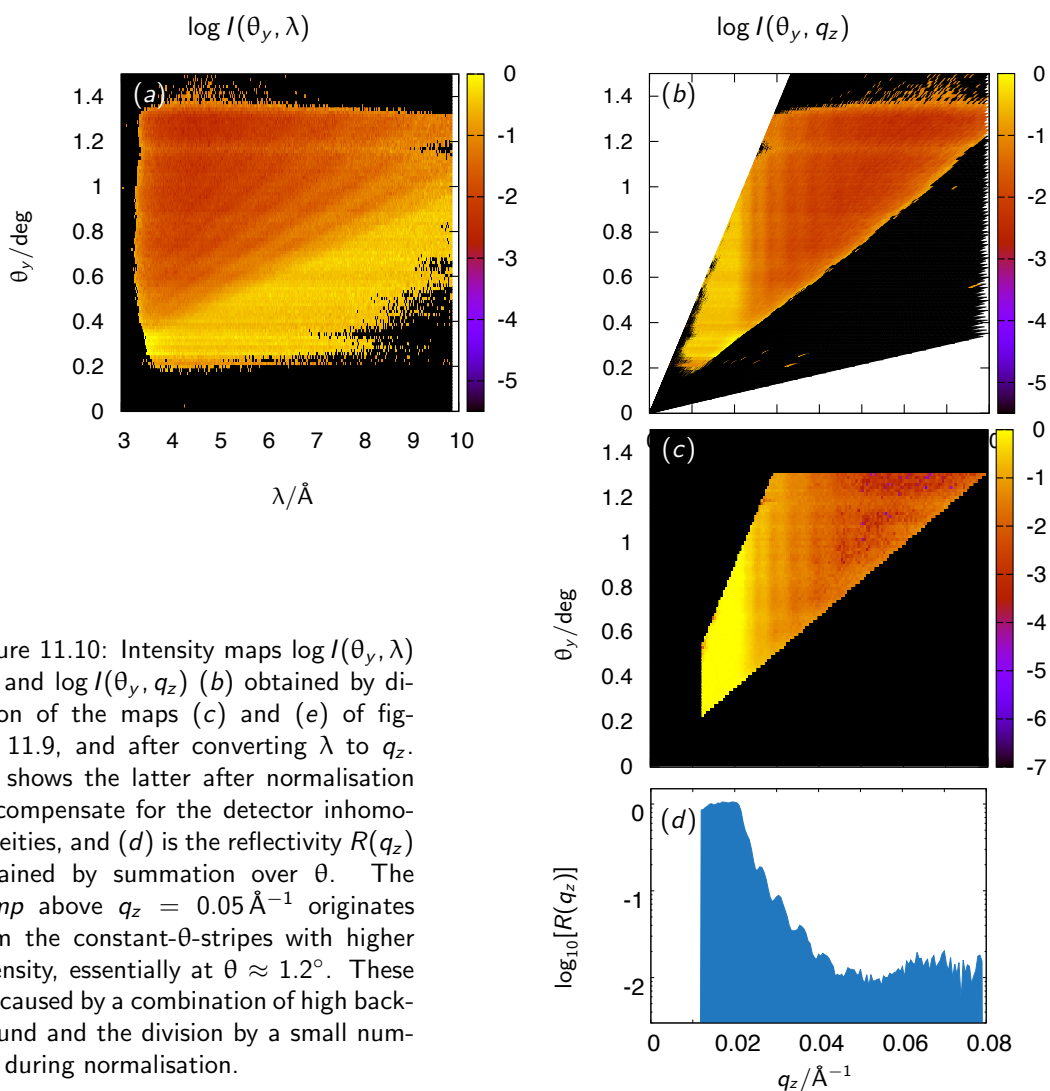


Figure 11.10: Intensity maps $\log I(\theta_y, \lambda)$ (a) and $\log I(\theta_y, q_z)$ (b) obtained by division of the maps (c) and (e) of figure 11.9, and after converting λ to q_z . (c) shows the latter after normalisation to compensate for the detector inhomogeneities, and (d) is the reflectivity $R(q_z)$ obtained by summation over θ . The *bump* above $q_z = 0.05 \text{\AA}^{-1}$ originates from the constant- θ -stripes with higher intensity, essentially at $\theta \approx 1.2^\circ$. These are caused by a combination of high background and the division by a small number during normalisation.

11.3.5 use of a diffusor

One can use the *Selene* guide to create a small virtual source far from the moderator. This might be of interest e.g. for an imaging beam line. In this case the beam emerging from the last focal point should have a homogeneous $I(\theta_x, \theta_y)$ distribution. Since in the present case the source is inhomogeneous (see figure 11.9 (b)) also the divergence after the *Selene* guide is. For the intensity map shown in figure 11.11 a 2 mm thick graphite plate was positioned at the focal point instead of the sample.

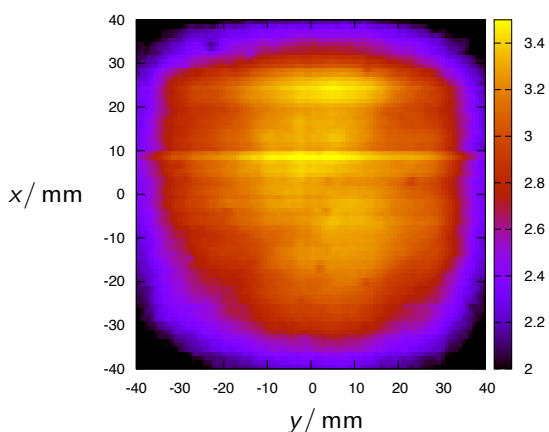


Figure 11.11: Intensity map $I(x, y)$ measured in direct view to the *Selene* guide with a 2 mm thick graphite plate at the sample position, acting as a diffusor. The distance from the graphite to the detector was 3200 mm. The bright horizontal stripe at $x \approx 9 \text{ mm}$ originates from a defect of the detector (electronics?).

11.3.6 discussion

The intended program for the first beamtime on BOA was too ambitious. Instead of the measurement of $R(q_z)$ of a reference sample in all principle operation modes (with chopper, with ML monochromator, using both), only the chopper mode was at least partly completed.

The main problems are not connected to the *Selene* guide but result from the experimental environment and the equipment:

- High background caused by fast neutrons coming down the BOA guide, and by thermal neutrons from the neighbouring imaging beamline ICON.
- In the meantime the background could be lowered by 2 orders of magnitude. The improvements on shielding are based on the measurements within this campaign.
- Inhomogeneous sensitivity of the ^3He area detector.
- Inhomogeneous beam profile and divergence of the beam leaving the BOA guide.
- This can be reduced by installing a graphite diffusor before the initial slit.
- Surprisingly low intensity.

On the other side it proved to be quite simple to align the guide elements using a (homogeneous) white light source before the initial focal point.

guide quality The overall quality of the guide is very good. Compared to the first elliptically focusing guide produced for Amor there is a lot of progress made by SwissNeutronics.

- Still there is some waviness visible, where the *propagation of the waves* is parallel to the neutron beam direction.
- The effect is so small that it hardly affects the data analysis.
- The two substrates for the horizontal and the vertical reflecting part of one guide element do not form exactly a 90° angle.
- This prohibits a simultaneous perfect alignment of the guide elements in both directions. An improvement is possible.
- At the region where two elements join, the reflectors do not exactly follow an elliptic shape, leading to reduced intensity coming from there.
- This should be improved. Off-situ analysis using light is planned to identify the real shape.

measurements

- For the chopper-only mode the inhomogeneities mentioned above play a minor role. Essentially they just lead to a reduction of the intensity. So in this case the measurements have been successful in a sense that a reflectivity curve could be measured. Limitations were imposed by the long counting time and the high background limiting the dynamic range.
- Using both, chopper and ML-monochromator was not successful: The much too low intensity even prohibited to align the sample.
- The data obtained with a ML-monochromator only, are not yet analysed completely. But since there the inhomogeneities of the beam and the detector directly influence the resolution and the λ - θ -encoding, it will be no surprise if the data analysis fails.

11.4 experiments on Amor

11.4.1 Amor

Amor is a neutron reflectometer at SINQ, PSI [38], which allows for a wide range of set-ups. The scattering geometry is vertical so that liquid surfaces are accessible. Most components are positioned on an optical bench which allows to play with the resolution, or to test exotic set-ups like the prism approach by R. Cubitt [32] or the *Selene* concept. In general Amor is operated in time-of-flight mode (realised by a double chopper), but it is also possible to run it with a monochromator.

The ML-monochromator is placed on the frame-overlap mirror stage and can be driven out of the beam.

fixed values	/ mm	
guide end – chopper housing start	:	75
guide end – chopper housing end	:	1309
guide end – earliest position polariser	:	2744
1 st slit – earliest position polariser	:	1242
typical values		
chopper disc 1 – chopper disc 2	:	490
3 rd slit – sample	:	400
sample – 4 th slit	:	400

Table 11.1: List of typical or fixed distances on Amor.

The chopper is positioned in a housing, some cm behind the end of the neutron guide. It consists of 2 discs, 490 mm apart, each with 2 openings of 13.6°. In general it is operated in a way to give $\Delta\lambda/\lambda = \text{const.}$ [39]. For the tests we used a pulse frequency of 23.3 Hz (corresponding to 700 rpm).

The chopper housing limits the maximum incoming divergence because it leads to a minimum distance of 1500 mm between the end of the guide to the first diaphragm. The distance to the first position where a monochromator can be placed (on the frame overlap filter stage) is some 1800 mm.

Behind the chopper housing and the 1st diaphragm a frame overlap filter is mounted. the latter consists of Si-wafers of 0.6 mm thickness, coated with a Ni/Ti $m^f = 2$ SM. If placed in the beam with an inclination of θ^f it reflects all neutrons with $\lambda > 4\pi \sin \theta^f / m^f q_{\text{Ni}}^c$. In the case of the strongly divergent beam the deviation of α^f from θ^f has to be taken into account. The cut-off wavelength is then $\lambda^f = 4\pi \sin(\theta^f - \theta) / m^f q_{\text{Ni}}^c$.

In TOF mode (without monochromator) the situation is more complicated: All neutron trajectories accepted by the elliptic guide should provide all required wavelengths. But the flat frame-overlap filter is angle dependent. A possible solution is to build a filter bent accordingly [→7.1]. This then is optimised for one specific cut-off wavelength.

11.4.2 high-intensity specular reflectometry

A principle sketch of this mode is given in 10.3. The standard disc choppers of Amor were used, operated at 750 rpm, giving a pulse rate of 25 s⁻¹. The first slit after the chopper housing was used to define the initial beam size. All other slits were removed or driven out of the way. The polariser (including a frame-overlap filter) [→7.1] and the *Selene* guide were mounted on a common, 3.5 m long X95 beam, mounted on a support which enables longitudinal and transverse translation, tilting and rotation. A technical design of the set-up is shown in figure 11.12. The distance from the sample position to the detector was 3000 mm.

Fe layer Polarised measurements² were performed on the multilayer³ Si (179 Å) / Fe (12 Å) / Cu (462 Å) / Si, where the substrate was some 15 × 15 mm². For normalisation a slightly larger $m = 5$ supermirror⁴ was used. Shown are the raw measurements, the corrected reflectivity as a function of θ before and after reformatting from λ to q_z , and the resulting reflectivity. The deviation of the 2 reflectivity curves implies that there is a rather high background of 10⁻³ for the red curve. Tests to find the origin of this revealed that the background results from cross-talk within the detector [→9.2.1].

The *Selene* guide leads to a horizontal and a vertical off-set of the beam of 106 mm. In height this can be corrected for by redefining the zero-position of the sample and the detector z translation. But the detector can not be translated horizontally. Thus the guide was mounted *diagonally* for the cost of horizontal divergence and thus of intensity. A horizontal movement of the granite block normal to the beam will be possible from 2014 on, and will increase the usable flux by at least a factor 2.

² for one spin state only, because of the lack of a spin-flipper at that time

³ courtesy of B. Wiedemann, Technical University Munich, Germany

⁴ courtesy of SwissNeutronics

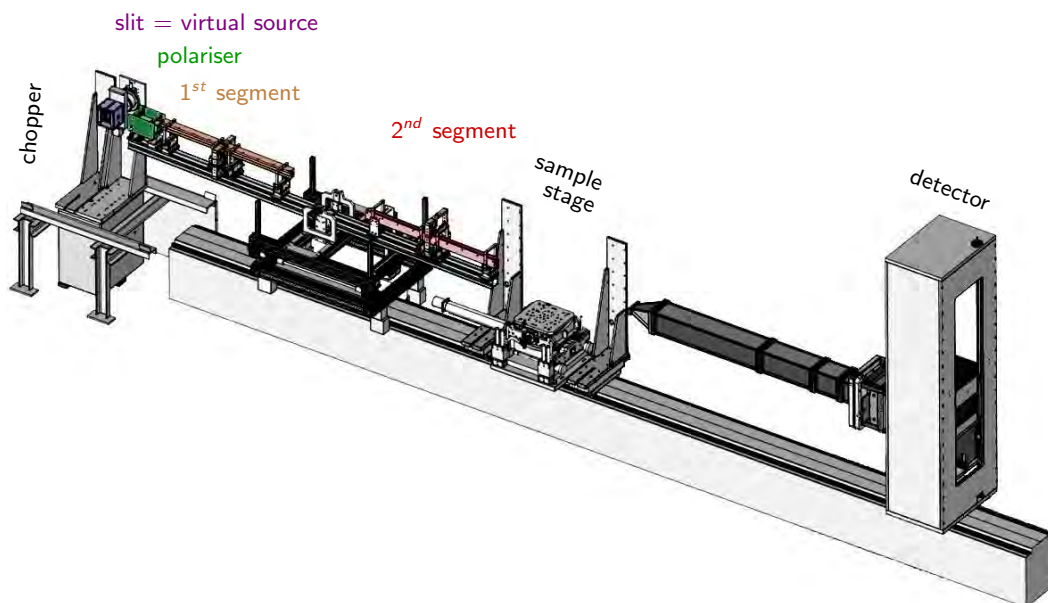


Figure 11.12: Set-up of the *Selene* guide on Amor including the polariser. The granite block (optical bench) is 8 m long.

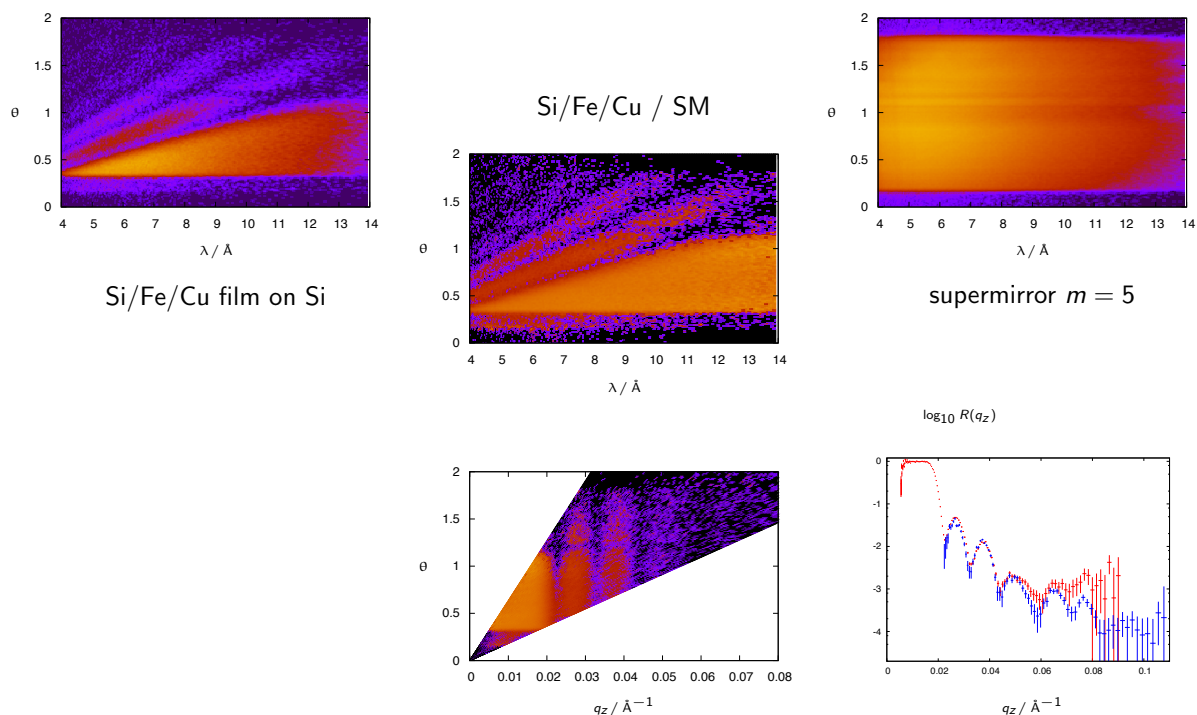


Figure 11.13: Measurements using the high-intensity specular reflectivity mode on Amor. The sample was a multilayer of the type Si (179 Å) / Fe (12 Å) / Cu (462 Å) / Si. For normalisation a $m = 5$ supermirror was used. Shown are the raw measurements in the top line, the corrected reflectivity as a function of θ before and after reformatting from λ to q_z , and the resulting reflectivity curve (red). The blue curve results from a second measurement with higher ω .

perovskite multilayer For an earlier test without polariser or frame-overlap mirror the samples were a $[\text{La}_{1/3}\text{Ca}_{2/3}\text{MnO}_3/\text{YBaCuO}_3]_5$ multilayer on SrTiO_3 with a period of 600 \AA and a layer thickness ratio of $2 : 1$. As reference to normalise the measurements and to characterise the beam a NiTi supermirror with $m = 5$ was used. Both samples had a surface area of $10 \times 10\text{ mm}^2$.

Figure 11.14 shows the intensity maps $I(\lambda, \theta)$ for both samples, and for the re-normalised map. The reflectivity extracted there from is displayed in figure 11.15. The measurement times for the maps shown were 4 h each, at an angle $\omega = 1.5^\circ$. The same measurements were performed also in 24 min and in 2.5 min, and at higher angles.

In map 11.14 (a) the iso- q_z lines for the first, second and fourth Bragg peak and for the total reflection edge are nicely visible. The dark line at $\theta \approx 0.9^\circ$ originates from a mis-alignment of the guides. This just leads to a reduced intensity, not to systematic errors. Since these measurements and the data reduction were performed with a constant $\Delta\lambda \propto \Delta t$ while the instrument has a resolution $\Delta\lambda/\lambda = \text{const.}$, the resolution at low q_z is

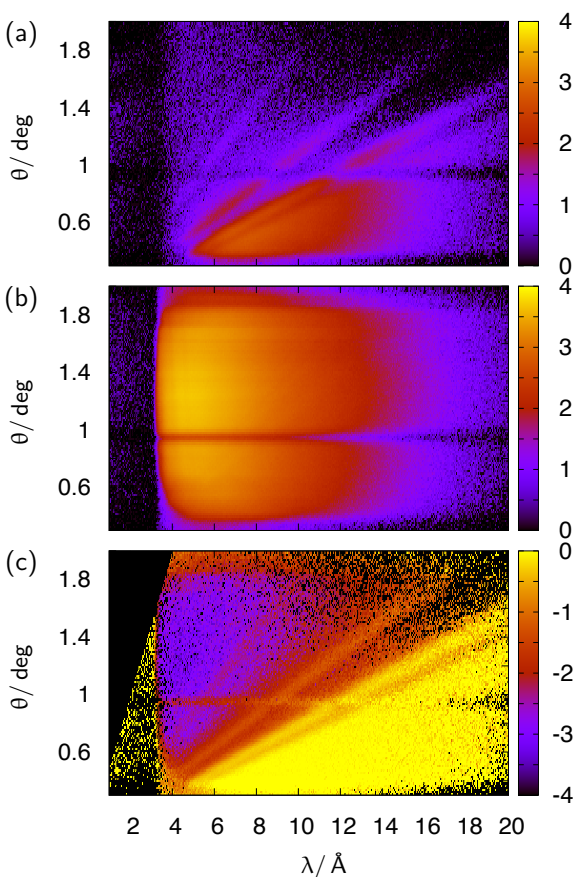


Figure 11.14: Intensity maps $\log_{10}[I(\lambda, \theta)]$ measured in 4 h with a LCMO/YBCO multilayer (a), and a NiTi supermirror (b). From these, map (c) is obtained by division. (d, blue line) Reflectivity curves $R(q_z)$ obtained by summation over equal q_z of the map (c). The red and green lines correspond to counting times of 24 min and 2.5 min. The differences visible at $q_z \approx 0.3\text{ \AA}^{-1}$ originate from a not yet correct treatment of the errors of zero-count channels.

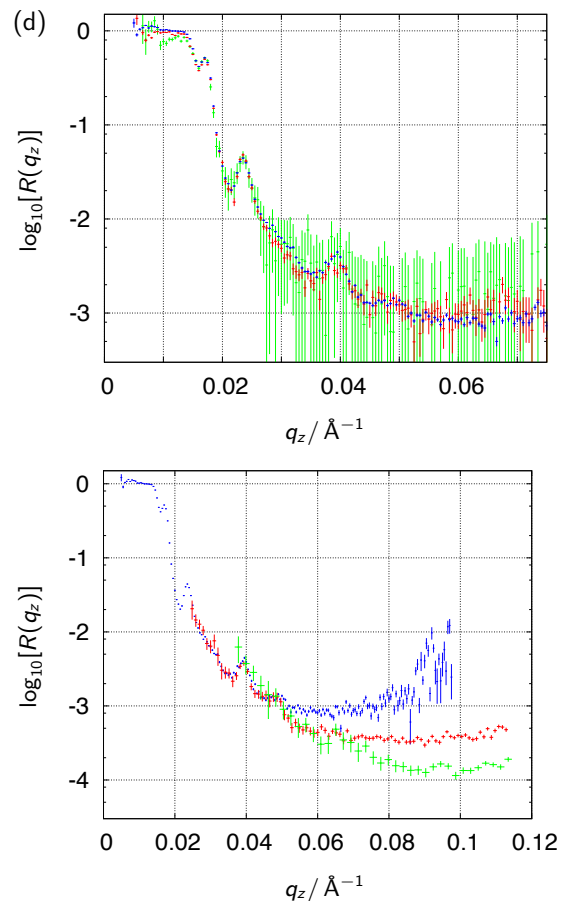


Figure 11.15: Reflectivity of a LCMO/YBCO multilayer. The blue curve is identical to the one in figure 11.14 (d), the others were obtained in a similar way with $\omega = 3^\circ$ (red), and $\omega = 4^\circ$ (green). The resolution was reduced accordingly. The deviations clearly illustrate the influence of the λ -dependent background.

underestimated, and at high q_z a coarser binning could be performed without loss of information, which would qualify the error-bars.

No frame-overlap filter was used, so that the totally reflected neutrons with $\lambda > 24 \text{ \AA}$ leak in at nominally $\lambda > 4 \text{ \AA}$. This leaking can be seen in the maps at $\lambda < 3.5 \text{ \AA}$.

11.4.3 angle-wavelength-encoding

In addition to the operation mode described in 11.4.2 a multilayer monochromator (\rightarrow 11.2.4) is installed after the chopper. As a consequence the first slit on Amor could not be used anymore and was replaced by a manual slit system behind the monochromator. Unfortunately, the chopper was operated at 1500 rpm and with a non-adequate time binning scheme. This results in half the intensity for $\lambda < 6.8 \text{ \AA}$. The samples were the same LCMO/YBCO multilayer and NiTi supermirror discussed above.

The resulting reflectivity is compared to the one obtained with the height-intensity mode in figure 11.16 (d). The much reduced statistics displays the intensity gain one gets by loosening the resolution and using a high divergence. In addition, for $q_z > 0.03 \text{ \AA}^{-1}$ the mentioned mismatch of chopper speed and time binning leads to a further reduction of the statistics by a factor 2.

The deviation of $R(q_z)$ for small $q - z$ results from problems with the normalisation. Most likely the positions of both samples were not exactly identical, leading to a slightly different illumination. This is most severe for low angles, where the projected sample size might be smaller than the position off-set.

11.4.4 discussion

Overall the test series on Amor was successful, for it proved that even delicate samples can be measured. The gain in counting time relative to the normal operation mode on Amor is about one order of magnitude for small samples. This value was estimated from the actual counting time, the illuminated sample area, and the difference of the chopper speeds.

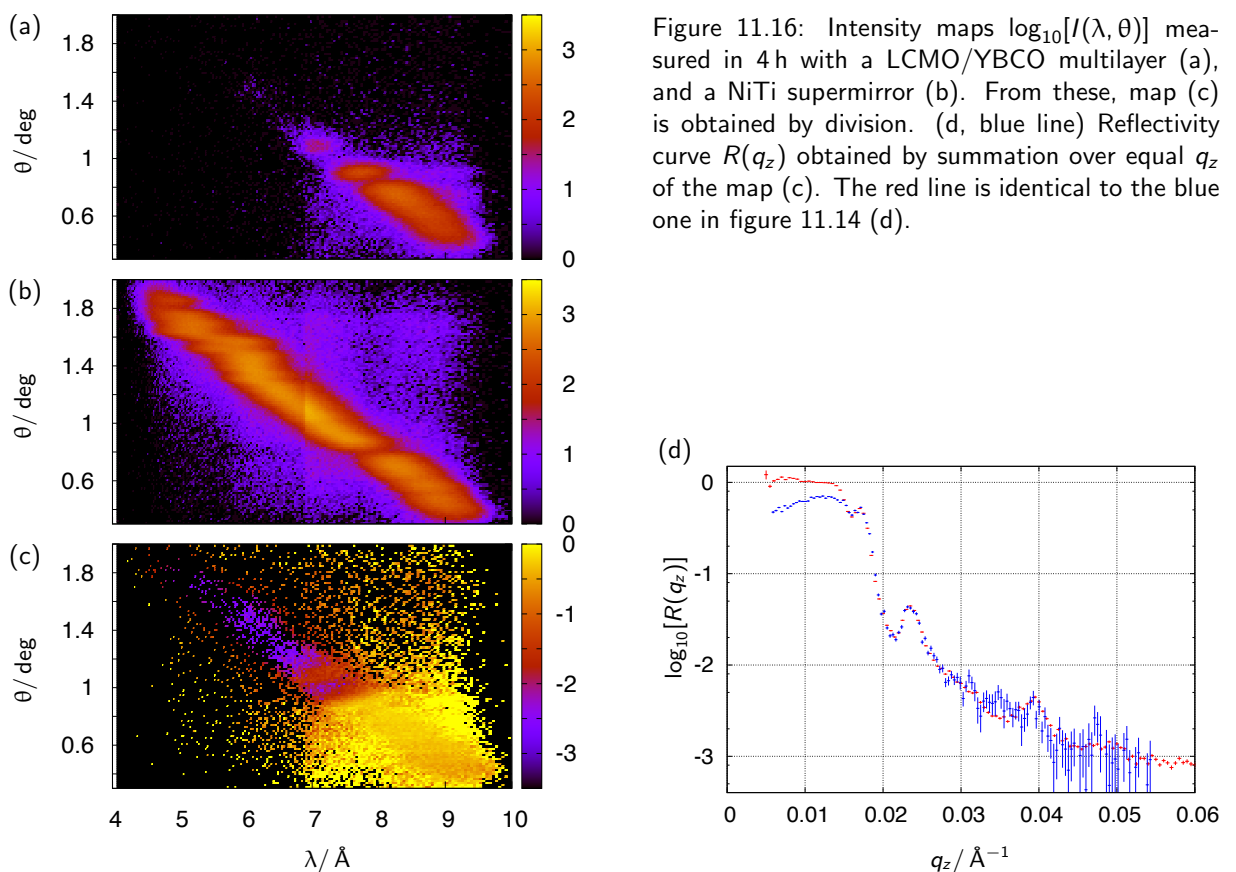


Figure 11.16: Intensity maps $\log_{10}[I(\lambda, \theta)]$ measured in 4 h with a LCMO/YBCO multilayer (a), and a NiTi supermirror (b). From these, map (c) is obtained by division. (d, blue line) Reflectivity curve $R(q_z)$ obtained by summation over equal q_z of the map (c). The red line is identical to the blue one in figure 11.14 (d).

The measurements also revealed the problems still present. The different beam geometry requires adapted shielding and modified slit mounts to reduce background. This was already realised by end of 2012. Still to come is the possibility to horizontally move the optical bench.

The horizontal stripe pattern visible in the intensity maps results from a misalignment of the guide elements and from waviness on the reflecting surfaces. The relative alignment of the guides can be improved. Mechanical modifications are being discussed with SwissNeutronics. For the waviness the problem is more difficult to solve. Measurements with an interferometer suggest that the main contribution to the waviness comes from an inhomogeneous distribution of the glue which attaches the coated thin substrate to the shape-giving thick glass model. The waviness leads to distortions in the angle-wavelength-encoding and thus to a reduced resolution in this operation mode. For the other modes it just results in a reduction of the intensity by fractions of a percent, so it might be neglected there.

The small sample size together with the small beam spot requests a more precise and reproducible way to align the sample. Here we want to investigate approaches as used in x-ray or synchrotron experiments. The challenge will be to realise these when using e.g. a cryomagnet.

outlook The *Selene* prototype will be further improved and used in the future as an add-on on Amor. Besides this it is available for the neutron scattering community for tests, either on Amor or BOA, or at other institutes. The improvements are:

- modification of the aluminium backbone to allow for an individual alignment of the two mirrors forming one building block of 600 mm length;
- inclusion of an RF spin flipper between the two guide sections (under construction);
- addition of a precision slit to allow for exact 3-dimensional footprint definition (under construction);
- design/construction of some housing enabling an Ar atmosphere along the beam path to avoid attenuation by air scattering (up to 40% for $\lambda = 10 \text{ \AA}$);
- modification of the optical bench of Amor to enable a horizontal movement of the detector (under construction). This is necessary to compensate for the horizontal beam off-set of 10 cm by the *Selene* guide. This measure increases the accepted (and transmitted) divergence and thus the intensity at the sample.

References

- [1] Sang-Wook Cheong and Maxim Mostovoy. Multiferroics: a magnetic twist for ferroelectricity. *Nature Materials*, 6(1):13–20, JAN 2007.
- [2] R. Ramesh and Nicola A. Spaldin. Multiferroics: progress and prospects in thin films. *Nature Materials*, 6(1):21–29, JAN 2007.
- [3] J. Hoppler, J. Stahn, Ch. Niedermayer, V. K. Malik, H. Bouyanfif, A. J. Drew, M. Roessle, A. Buzdin, G. Cristiani, H. U. Habermeier, B. Keimer, and C. Bernhard. Giant superconductivity-induced modulation of the ferromagnetic magnetization in a cuprate-manganite superlattice. *Nature Materials*, 8(4):315–319, APR 2009.
- [4] B. J. Kirby, D. Kan, A. Luykx, M. Murakami, D. Kundaliya, and I. Takeuchi. Anomalous ferromagnetism in TbMnO₃ thin films. *Journal of Applied Physics*, 105(7), APR 1 2009. 53rd Annual Conference on Magnetism and Magnetic Materials, Austin, TX, NOV 11-14, 2008.
- [5] J. S. White, M. Bator, Y. Hu, H. Luetkens, J. Stahn, S. Capelli, S. Das, M. Döbeli, Th. Lippert, V. K. Malik, J. Martynczuk, A. Wokaun, M. Kenzelmann, Ch. Niedermayer, and C. W. Schneider. Strain-induced ferromagnetism in antiferromagnetic lumino₃ thin films. *Phys. Rev. Lett.*, 111:037201, Jul 2013.
- [6] A Ohtomo, DA Muller, JL Grazul, and HY Hwang. Artificial charge-modulation in atomic-scale perovskite titanate superlattices. *Nature*, 419(6905):378–380, SEP 26 2002.
- [7] A Ohtomo and HY Hwang. A high-mobility electron gas at the LaAlO₃/SrTiO₃ heterointerface. *Nature*, 427(6973):423–426, JAN 29 2004.
- [8] J. Mannhart, D. H. A. Blank, H. Y. Hwang, A. J. Millis, and J. M. Triscone. Two-Dimensional Electron Gases at Oxide Interfaces. *MRS Bulletin*, 33(11):1027–1034, NOV 2008.
- [9] Pavlo Zubko, Stefano Gariglio, Marc Gabay, Philippe Ghosez, and Jean-Marc Triscone. Interface Physics in Complex Oxide Heterostructures. In Langer, JS, editor, *Annual Review of Condensed Matter Physics, VOL 2*, volume 2 of *Annual Review of Condensed Matter Physics*, pages 141–165. 2011.
- [10] Marta Gibert, Pavlo Zubko, Raoul Scherwitzl, Jorge Iniguez, and Jean-Marc Triscone. Exchange bias in LaNiO₃-LaMnO₃ superlattices. *Nature Materials*, 11(3):195–198, MAR 2012.
- [11] A. V. Boris, Y. Matiks, E. Benckiser, A. Frano, P. Popovich, V. Hinkov, P. Wochner, M. Castro-Colin, E. Detemple, V. K. Malik, C. Bernhard, T. Prokscha, A. Suter, Z. Salman, E. Morenzoni, G. Cristiani, H. U. Habermeier, and B. Keimer. Dimensionality Control of Electronic Phase Transitions in Nickel-Oxide Superlattices. *Science*, 332(6032):937–940, MAY 20 2011.
- [12] H Schmidt, M Gupta, and M Bruns. Nitrogen diffusion in amorphous silicon nitride isotope multilayers probed by neutron reflectometry. *Physical Review Letters*, 96(5), FEB 10 2006.
- [13] H. Schmidt, U. Geckle, and M. Bruns. Simultaneous diffusion of Si and N in silicon nitride. *Physical Review B*, 74(4), JUL 2006.
- [14] E. Hueger, H. Schmidt, J. Stahn, B. Braunschweig, U. Geckle, M. Bruns, and A. Markwitz. Atomic transport in metastable compounds: Case study of self-diffusion in Si-C-N films using neutron reflectometry. *Physical Review B*, 80(22), DEC 2009.

- [15] Sujoy Chakravarty, Harald Schmidt, Ursula Tietze, Dieter Lott, N. P. Lalla, and Ajay Gupta. Self-diffusion and defect annihilation in nanocrystalline Fe films probed by neutron reflectometry. *Physical Review B*, 80(1), JUL 2009.
- [16] E. Hueger, U. Tietze, D. Lott, H. Bracht, D. Bougeard, E. E. Haller, and H. Schmidt. Self-diffusion in germanium isotope multilayers at low temperatures. *Applied Physics Letters*, 93(16), OCT 20 2008.
- [17] E. Hueger, J. Rahn, J. Stahn, T. Geue, and H. Schmidt. Diffusivity determination in bulk materials on nanometric length scales using neutron reflectometry. *Physical Review B*, 85(21), JUN 4 2012.
- [18] Erwin Hueger, Lars Doerrer, Johanna Rahn, Tobias Panzner, Jochen Stahn, Gerhard Lilienkamp, and Harald Schmidt. Lithium Transport through Nanosized Amorphous Silicon Layers. *Nano Letters*, 13(3):1237–1244, MAR 2013.
- [19] D. Pantel, S. Goetze, D. Hesse, and M. Alexe. Reversible electrical switching of spin polarization in multiferroic tunnel junctions. *Nature Materials*, 11:289293, 2012.
- [20] J. Stahn, T. Panzner, U. Filges, C. Marcelot, and P. Böni. Study on a focusing, low-background neutron delivery system. *N.I.M. A*, page in press, 2010.
- [21] J. Stahn, U. Filges, and T. Panzner. Focusing specular neutron reflectometry for small samples. *The European Physical Journal Applied Physics*, 58, 4 2012.
- [22] Frédéric Ott and Alain Menelle. Refocus: A new concept for a very high flux neutron reflectometer. *Nuclear Instruments and Methods in Physics Research A*, 586(1):23 – 30, 2008. Proceedings of the European Workshop on Neutron Optics - NOP '07.
- [23] F. Ott and A. Menelle. New designs for high intensity specular neutron reflectometers. *European Physical Journal - Special Topics*, 167:93–99, 2009.
- [24] Phillip M. Bentley, Shane J. Kennedy, Ken H. Andersen, Damian Martin Rodriguez, and David F. R. Mildner. Correction of optical aberrations in elliptic neutron guides. *N.I.M. A*, 693:268–275, 2012.
- [25] L. D. Cussen, D. Nekrassov, C. Zandler, and K. Lieutenant. Multiple reflections in elliptic neutron guide tubes. *Nuclear Instruments & Methods in Physics Research Section A-Accelerators Spectrometers Detectors and Associated Equipment*, 705:121–131, MAR 21 2013.
- [26] M. Montel. X-ray microscopy with catamegonic roof mirrors. *X-ray microscopy and microradiography*, pages 177–185, 1957.
- [27] M. Russina, F. Mezei, and G. Kali. First Implementation of Novel Multiplexing Techniques for Advanced Instruments at Pulsed Neutron Sources. In *5th European Conference on Neutron Scattering*, volume 340 of *Journal of Physics Conference Series*, Dirac House, Temple Back, Bristol BS1 6BE, England, 2012. European Nucl Scattering Assoc, IOP Publishing Ltd. 5th European Conference on Neutron Scattering (ECNS), Prague, Czech Republic, JUL 17-21, 2011.
- [28] R.T. Robiscoe. A spin flip problem. *Am. J. Phys.*, 39:146150, 146-150.
- [29] S.V. Grigoriev, A.I. Okorokov, and V.V. Runov. Peculiarities of the construction and application of a broadband adiabatic flipper of cold neutrons. *Nucl. Instr. and Meth. A*, 384:451456, 1997.
- [30] Maruyama R., Ebisawa T., Tasaki S., Hino M., Takeda M., Kawai T., Kawabata Y., and Sakai K. A resonance neutron-spin flipper for neutron spin echo at pulsed sources. *Physica B*, 335(1):238–242, 2003.
- [31] J. Stahn. A switchable white-beam neutron polariser. *Physica B: Condensed Matter*, 345(1-4):243 – 245, 2004. Proceedings of the Conference on Polarised Neutron and Synchrotron X-rays for Magnetism.
- [32] R. Cubitt. *N.I.M. A*, 558:547–550, 2006.
- [33] R. Cubitt and J. Stahn. Neutron reflectometry by refractive encoding. *Eur. Phys. J. Plus*, 126:111, 2011.
- [34] R. Georgii, G. Brandl, N. Arend, W. Haeussler, A. Tischendorf, C. Pfeleiderer, P. Boeni, and J. Lal. Turn-key module for neutron scattering with sub-micro-ev resolution. *Applied Physics Letters*, 98:073505, 2011.

-
- [35] M. Schneider, J. Stahn, and P. Böni. Focusing of cold neutrons: Performance of a laterally graded and parabolically bent multilayer. *Nuclear Instruments and Methods in Physics Research Section A: Accelerators, Spectrometers, Detectors and Associated Equipment*, 610(2):530 – 533, 2009.
- [36] P. Mikulík. *EDXR — X-ray and neutron reflectivity calculation program*. mikulik@physics.muni.cz, 2001.
- [37] U. Filges. First experiments on the new boa instrument at sinq. *Swiss Neutron News*, 40:4–8, 2012.
- [38] M. Gupta, T. Gutberlet, J. Stahn, P. Keller, and D. Clemens. Amor - the time-of-flight neutron reflectometer at SINQ/PSI. *Pramana-Journal of Physics*, 63:57–63, 2004.
- [39] A.A. van Well. Double-disk chopper for neutron time-of-flight experiments. *Physica B: Condensed Matter*, 180-181(2):959 – 961, 1992.